TUHH ims
Institute of
Multiphase Flows

Bachelor Thesis

Experimental Investigation of the Flow Behavior of Lagrangian LED Particles in a 200 L Bioreactor

by Maximilian Kamp

1st Examiner: Prof. Dr.-Ing. Michael Schlüter
Supervisor: Sebastian Hofmann, M.Sc.

25.02.2022 - 29.04.2022

Eidesstattliche Erklärung

Hiermit versichere ich, dass ich die vorliegende Arbeit selbstständig verfasst und keine anderen als die angegebenen Quellen und Hilfsmittel benutzt habe, dass alle Ausführungen, die anderen Schriften wörtlich oder sinngemäß entnommen wurden, kenntlich gemacht sind und dass die Arbeit in gleicher oder ähnlicher Fassung noch nicht Bestandteil einer Studien- oder Prüfungsleistung war.

Hamburg, den _____ Unterschrift: _____

Technische Universität Hamburg | V-5 | 21073 Hamburg

Maximilian Kamp

Institut für Mehrphasenströmungen
Institutsleiter: Prof. Dr.-Ing. habil. Michael Schlüter

Hamburg, 25.02.2022

Task definition for the Bachelor thesis

Title: Experimental Investigation of the Flow Behavior of Lagrangian LED Particles in a 200 L Bioreactor

General challenge and scientific objective:

In stirred tank bioreactors, the homogeneity of the fermentation broth is an important criteria in terms of product quality and quantity, and thus needs to be controlled precisely. This is particularly challenging as cells often experience transient culture conditions in heterogeneously mixed industrial scale bioreactors. Monitoring depends on the information provided by the implemented sensors (temperature, pH, dissolved oxygen concentration and many more). However, these sensors are mostly limited in their position close to the reactor wall, and therefore cannot accurately give information about occurring dead zones and compartments. To tackle this issue, Lagrangian Sensor Particles (LSP) are being developed by multiple research teams all over the world and also at the Institute of Multiphase Flows. These LSPs are supposed to move with the fluid flow and provide information about the conditions alongside the sensor's position in the reactor. Thereby, the latter is a valuable information, since these particle trajectories differ from lifelines of a cell, and thus need to be characterized. However, in order to understand the flow behavior in combination with the recorded data of these mobilized sensors in a highly turbulent flow a thorough investigation of sole inertial particles is needed first. Various challenges are presented, like designing a robust, luminous hollow sphere, developing a MATLAB algorithm for particle recognition and spatial and temporal tracking and an eventual quantitative evaluation with respect to probability of residence in reactor regions, velocity and acceleration distributions.

Institut für Mehrphasenströmungen (V-5)
Gebäude O | Eißendorfer Str. 38
21073 Hamburg
T. +49 40 428 78-3106
sebastian.hofmann@tuhh.de
www.ims.tuhh.de

Scope of work:

This Bachelor thesis aims at providing solutions to the above stated issues, by means of building Lagrangian LED Particles and the development of a robust MATLAB code, which shall be functional for different reactors (200 L up to 15000 L) and particle sizes and types in upcoming studies. Furthermore, the code should work even during poor visibility conditions as occurring while gassing with spargers.
To do so, in a first step, PMMA shells (d = 25 mm) need to be manufactured and equipped with suitable LEDs. A 200 L bioreactor is used in this study to test a proper shell design and eventually record these particles with a camera. Parameters like impeller speed, gassing rate, sparger type and agitator type will be varied. The main focus will be on the second step, the development of a MATLAB code, whereas the following prerequisites are to be implemented:

- Image calibration step with the utilization of a calibration target inside the reactor to minimize distortion and refraction.
- Image preprocessing, LED mote recognition and distortion removal algorithm.
- Track recognition code to record LED mote tracks.
- Documentation (FAIR) of the MATLAB algorithm for utilization and adjustment in upcoming studies.

This visual tracking will provide a quantitative evaluation with respect to residence times in reactor regions, velocity and acceleration distributions throughout the reactor.

The guidelines for the preparation of a Bachelor thesis are available at the Institute of Multiphase Flows and must be observed. The thesis will be written in English.

Prof. Dr.-Ing. Michael Schlüter Sebastian Hofmann, M.Sc. Maximilian Kamp

Institut für Musterlösungen
Gebäude | 21073 Hamburg
T. +49 40 428 78-XXXX
F. +49 40 428 78-YYYY
mustermann@tuhh.de
www.tuhh.de

Contents

List of Symbols, Units and Abbreviations

Dimensionless Numbers

Symbol	Meaning	Unit
St	Stokes Number	-
Re_p	Reynolds Number of the particle	-
Ar	Archimedes Number	-

Latin Symbols

Symbol	Meaning	Unit
d_2	Impeller diameter	m
D	Particle diameter	m
RPM	Revolutions per minute	min^{-1}
v_tip	Impeller tip speed	$\mathrm{m\,s}^{-1}$
f_rot	Rotational frequency	s^{-1}
C_D	Drag coefficient	-
u_t	Terminal particle velocity	$\mathrm{m\,s}^{-1}$
g	Gravitational acceleration	$\mathrm{m\,s}^{-2}$
d_*	Dimensionless particle diameter	-
W_m	Superficial gas velocity	$\mathrm{m\,s}^{-1}$
$\mathrm{v}_\mathrm{mag,m}$	Mean velocity magnitude	$\mathrm{m\,s}^{-1}$
$\mathrm{a}_\mathrm{mag,m}$	Mean acceleration magnitude	$\mathrm{m\,s}^{-2}$
$v_\mathrm{total,m}$	Mean total velocity	$\mathrm{m\,s}^{-1}$

$c_{\mathrm{mass,NaCl}}$	Mass concentration of sodium chloride	$\mathrm{kg\,kg^{-1}}$
k	Number of tracks	-
p	Number of positions in tracks	-
j	Number of total positions	-
r	Ratio of tracked and total positions	-

Greek Symbols

Symbol	Meaning	Unit
τ_{p}	Momentum response time of the particle	s
τ_{f}	Characteristic time of the flow field	s
μ_{f}	Dynamic viscosity of the fluid phase	$\mathrm{kg\,m^{-1}\,s^{-1}}$
ρ_{p}	Density of the particle	$\mathrm{kg\,m^{-3}}$
ρ_{f}	Density of the fluid phase	$\mathrm{kg\,m^{-3}}$
ρ_{solution}	Density of the sodium chloride solution	$\mathrm{kg\,m^{-3}}$

Abbreviations

Abbr.	Definition
STR	Continuously Stirred Tank Reactor
SU-STR	Single-use Continuously Stirred Tank Reactor
CHO	Chinese hamster ovary
PB	Pitched blade
RT	Rushton turbine
PBPB	Double pitched blade
RTPB	Rushton turbine and pitched blade
LSP	Lagrangian Sensor Particle
LED	Light-emitting diode
2D	2-Dimensional
3D	3-Dimensional
IMU	Inertial measurement unit
CAD	Computer-aided design

Zusammenfassung

Lagrange'sche Sensor-Partikel sind essenziell, um Informationen über Prozessbedingungen in Einwegbioreaktoren zu erlangen. Hierfür sollten die Partikel den Strömungen im Reaktor folgen. Bis jetzt war es jedoch nicht möglich, ihre internen Methoden zur Bestimmung ihrer Bewegungsbahnen zu validieren. Um dieses Problem zu lösen, werden in dieser Arbeit die Positionen von mit LEDs ausgestatteten Partikeln, LED-Motes genannt, in einem kontinuierlich gerührten 200-Liter-Tankreaktor bestehend aus Acrylglas visuell bestimmt und ihre Geschwindigkeiten und Beschleunigungen berechnet.

Zu diesem Zweck werden LED-Motes entworfen und hergestellt. MATLAB Skripte zur LED-Mote-Erkennung sowie ein Skript zur Beseitigung von Bildverzerrungen mit Hilfe einer geometrischen Kalibrierung werden entwickelt und mit Skripten zur Berechnung von Geschwindigkeits- und Beschleunigungswerten aus Positionsdaten kombiniert.

Experimente mit zwei verschiedenen Rührerkombinationen werden durchgeführt. Die erste Rührerkombination besteht aus einem Rushton-Turbinen-Rührer und einem Schrägblattrührer. Die zweite Rührerkombination besteht aus zwei Schrägblattrührern. Die Experimente werden ohne Begasung und mit einer Begasungsrate von $15\,\mathrm{l}\cdot\mathrm{min}^{-1}$ und $20\,\mathrm{l}\cdot\mathrm{min}^{-1}$ unter Verwendung sowohl eines Mikro- als auch eines Makrobegasungstellers durchgeführt. Somit werden, von Variationen der Rührerdrehzahl abgesehen, 10 Kombinationen von Versuchsparametern umgesetzt. Experimente mit allen Parameterkombinationen werden mit Rührerdrehzahlen von 50, 70, 100 und 120 Umdrehungen pro Minute durchgeführt, was insgesamt 40 Experimente ergibt.

Ein hoher Anteil der theoretisch möglichen LED-Mote-Positionen

wird erkannt. Nur Positionen, welche einem Positions-Track mit einer Länge von 5 oder mehr Positionen zugeordnet werden können, werden für die Berechnung von Geschwindigkeits- und Beschleunigungswerten verwendet. Bis zu 94% der erkannten Positionen können einem solchen Positions-Track zugeordnet werden. Für den begasten Fall, bei welchem die Sichtbarkeit verringert ist, ist dieser Anteil geringer, mit einem Minimalanteil von 66%. Für die meisten Experimente liegt der Anteil der für Berechnungen verwendeten Positionen zwischen 80% und 90%.

Die Ergebnisse zeigen, dass die Verfolgung der 2D-Positionen von LED-Motes zu einem guten Verständnis der vorherrschenden Strömungsphänomene in einem kontinuierlich gerührten Tankreaktor führen. Die höchsten berechneten durchschnittlichen Geschwindigkeitsmagnituden in einem einzelnen 62 mm mal 60 mm Untersuchungsfenster haben einen Wert von circa der Hälfte der Geschwindigkeit der Rührerspitzen. Die erwarteten Strömungsmuster für die verschiedenen Rührertypen werden nachgewiesen. Der Rushton-Turbinen-Rührer verursacht hohe radiale Geschwindigkeiten, während die Schrägblattrührer hohe axiale Geschwindigkeiten verursachen. Eine ausreichende Auflösung der Geschwindigkeits- und Beschleunigungsdaten kann selbst bei kurzen Versuchslaufzeiten von nur 120 s erreicht werden. Im begasten Fall kommt es jedoch zur Abschattung der LED-Motes, was zu einer Minderung der Ergebnisqualität führt.

Durch eine längere Aufnahmezeit, oder eine Erhöhung der LED-Leuchtkraft kann die Qualität und Auflösung der Ergebnisse noch weiter verbessert werden.

Nützlichkeit und Qualität der Daten kann durch die Entwicklung von 3D-Tracking-Techniken erhöht werden, bei denen zwei Kameras oder ein Spiegelaufbau verwendet werden, um zwei verschiedene Blickwinkel auf den Reaktor zu erhalten, anstatt nur einen Blickwinkel zu evaluieren. Das entwickelte Skript schafft hierfür eine solide Grundlage.

Abstract

Lagrangian Sensor Particles are essential in gaining knowledge about process conditions inside of Single-Use Stirred Tank Bioreactors. To facilitate this, the particles should follow the flow of the fluids inside of the reactor.

However, so far it has not been possible to validate their internal means of trajectory determination. To address this problem, in this thesis the positions of LED-equipped tracking particles, called LED Motes, in a 200 L Continuously Stirred Tank Reactor made of acrylic glass are measured visually and their velocities and accelerations calculated.

To this end, LED Motes are designed and manufactured. A mote recognition script as well as a script for removal of distortions in the image through geometric calibration for MATLAB is developed to complement scripts for the calculation of velocity and acceleration values from positional data.

Experiments are performed utilizing two different stirrer setups, one consisting of a Rushton turbine impeller and a pitched blade impeller and the other consisting of two pitched blade impellers. The experiments are performed without aeration and with an aeration rate of 15 $\mathrm{l} \cdot \mathrm{min}^{-1}$ and 20 $\mathrm{l} \cdot \mathrm{min}^{-1}$ using both a micro and a macro sparger. Thus, a total of 10 combinations of experimental parameters are achieved not accounting for variations in stirrer speed. Experiments utilizing every combination of experimental parameters are performed at four different stirrer speeds of 50, 70, 100 and 120 RPM for a total of 40 experiments.

A high proportion of theoretically possible LED Mote positions are recognized. Only positions that can be assigned to a track of a length of more than 5 positions are evaluated for the calculation

of velocity and acceleration values. Up to 94% of the recognized positions are assigned to such a track. However, for the low-visibility, aerated, cases the percentage of positions assigned to tracks long enough to allow for evaluation is lower, reaching as low as 66%. For the majority of experiments the percentage of positions used for calculations lies between 80% and 90%.

The results show that the tracking of the 2D positions of LED Motes can lead to a good understanding of the dominant flow phenomena inside of a CSTR. The highest calculated mean velocity magnitudes for a single 62 mm by 60 mm interrogation window are approximately half of the stirrer tip speed. The expected flow patterns for the different stirrer types are observed. The Rushton turbine impeller causes high radial velocities while the pitched blade impellers cause high axial velocities. A good resolution of velocity and acceleration data can be achieved even with short experimental run times of only 120 s. However, for the aerated case, obscuration of the LED Motes reduces the quality of the results. A longer experimental run time and an increase in LED-brightness can increase the quality and resolution of the evaluation results even further. Usefulness and quality of data can be increased by the development of 3D tracking techniques using two cameras or a mirror setup to achieve two different viewpoints of the reactors instead of evaluating a single point of view. For this, the produced script lays a solid foundation.

1. Introduction

When operating a continuously stirred tank bioreactor (STR), knowledge about the process conditions inside of the reactor is essential to the implementation and optimization of fermentation processes. Traditional methods of measuring the process conditions, such as measurements taken at a stationary probe, also called Eulerian measurements, can provide information about fluid conditions at fixed points of measurement. However, probes cannot measure process conditions at every point inside of the reactor. As such, undetected heterogeneities in process conditions can lead to a divergence between measured conditions and conditions experienced by microorganisms during fermentation [Rei16].

Therefore, to attain information about the process conditions experienced by microorganisms at different points inside of the reactor and detect heterogeneities and dead zones, measurements taken by sensors moving with the fluid, also called Lagrangian measurements, are necessary.

To facilitate this, Lagrangian Sensor Particles (LSP) are a subject of active research by a multitude of scientific research groups. LSP are particles that move inside of the fluid while measuring process parameters using sensors. By following a trajectory that is characteristic for their density and size, LSP are able to detect heterogeneities in reactor conditions emerging during fermentation. However, as the minimum size of LSP is limited by the contained sensor and battery dimensions, their flow-following properties are not ideal. As such, the possibility of undetected heterogeneities and compartmentalization remains.

To address this challenge, knowledge about the trajectories of the LSP inside of the bioreactor is required. Multiple approaches for

the detection of LSP locations are being pursued. Among them are the tracking of the vertical position of LSP inside of the reactor based on hydrostatic pressure measurements and the use of inertial measurement units (IMU) to reconstruct LSP trajectories based on internally measured accelerations [Bun20,Rei16]. Both of these methods are as yet not reliable in reconstructing the exact locations of LSP. Additionally, simulations are used to predict LSP distributions throughout the reactor [Lau19]. However, these simulations of LSP trajectories lack experimental verification.

Therefore, in order to address these challenges, in this thesis the particle positions and trajectories throughout an acrylic stirred tank bioreactor are spatially and temporally resolved. The data obtained through the detection process designed for this thesis will be used to validate and improve the reconstruction of trajectories based on internal sensor data of LSP equipped with LEDs. To simplify the problem, this work focuses solely on particle tracking velocimetry without actual implementation of sensors.

The objective of this project is the implementation of a process capable of detecting the positions of tracking particles containing light-emitting diodes (LED Motes). Additionally, the positions of LED Motes, as well as their their velocities and accelerations are to be determined in a STR under different process parameters. Furthermore, the Stokes Number of the utilized particle-fluid system is to be estimated. This is to give an indication of the degree of flow-following behavior that can be expected by the deployed LED Motes.

The implemented process will be used to improve the precision of IMU and pressure sensor based location detection of LSP designed for the Priority Program SPP 2170 "InterZell" (funded by the German Research Foundation - Deutsche Forschungsgemeinschaft) and will further be used for the validation of Lattice-Boltzmann simulations of inertial particles in large-scale bioreactors.

2. Theoretical Background

2.1. Single-use Stirred Tank Reactors

Bioreactors are used to facilitate expression of specific products by microorganisms, such as Chinese Hamster Ovary (CHO) cells, within the reactor under controlled conditions [Eib10]. Typical bioreactors are made of stainless steel and have to be sterilized using hot steam before usage and cleaned thoroughly after every use. This process is costly and time intensive [Eib18]. The risks of contamination is high if the sterilization is not carried out properly as processes are usually carried out aseptically [Löf13]. Singe-use bioreactors are characterized by their disposal after one fermentation. They are typically pre-sterilized by the manufacturer through irradiation with gamma rays or autoclaving [Eib19]. Because of this, single-use bioreactors allow for more operation time, a higher flexibility in process parameters, lower costs and reduced risk of contamination [Löf14]. The cultivation container for most single-use bioreactors is a bag made out of layered plastics. In the first single-use bioreactor designs, mixing was accomplished by shaking or rocking the reactor, not by stirring as is the case in the much better understood Stirred Tank Reactors [Löf13,Gla10]. Newer single-use bioreactor designs combine the well-known mixing and scale-up attributes and design characteristics of established reusable stirred tank bioreactors with the advantages of single-use bioreactors by encasing the cultivation bag in a rigid, stainless steel frame in the form of a traditional Stirred Tank Reactor [Wil14] (Figure 2.1).

Figure 2.1.: Single-use bioreactor bag with a volume of 1 m^3 being placed into a Biostat STR with a top-adjusted stirrer motor [Eib18]. The control unit is visible to the right.

In addition to their advantages, single-use bioreactors present some challenges. Among those challenges is the secretion of chemicals from the plastic bag into the medium, causing inhibited cell growth and a reduction in product quality. Another big challenge for designing, characterizing and operating single-use bioreactors is their typically low level of instrumentation due to a lack of single-use sensors [Löf14]. Utilizing standard sensors increases the cleaning and sterilization

time and the risk of contamination due to their contact with the medium. The mentioned issues diminish the advantages of the single-use technology and usage of standard sensors is thus regarded only as a compromise. Products typically manufactured using single-use bioreactor technology are pharmaceutical and of high value, such as modern vaccines and antibodies, hormones and enzymes [Eib19,Löf14].

One available SU-STR design is the Biostat STR 200 by Sartorius Stedim Biotech [Wil14]. This reactor has a working volume of 200 L, with a total height of 1 m, a diameter of 0.6 m and a height to diameter ratio of 1.8. Two types of stirrer setups can be installed. The first setup utilizes a Rushton turbine (RT) impeller at the bottom with a pitched blade impeller (PB) above (RTPB). The second setup utilizes a two-stage pitched blade (PB) impeller setup (PBPB). The impeller diameter is 22.5 cm and the distance between impellers 0.3 m. Pitched blade impellers generate large axial flow patterns, and thus achieve a high degree of homogeneity throughout the reactor . At similar impeller speed and diameter, a PBPB setup causes a lower energy dissipation rate, and thus lower shear forces in comparison to a similar setup including a Rushton turbine [Wer97]. However, Rushton turbine impellers generate high radial flows, high local energy dissipation rates in the vicinity of the impeller tips, and thus an increase in gas bubble dispersion. Figure 2.2 shows a simulation of flow patterns caused by different stirrer types [Bis21b].

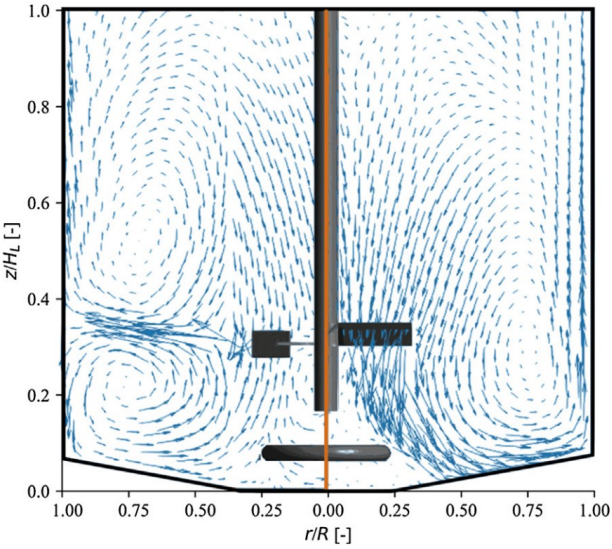

Figure 2.2.: Simulation of the flow patterns caused by a Rushton turbine impeller (left) and pitched blade impeller (right) [Bis21b]

Baffles are used in traditional STR to prevent bulk rotation of the liquid and to increase axial flow inside of the reactor [Zlo01]. Figure 2.3 shows the flow patterns caused by different impellers in a baffled reactor.

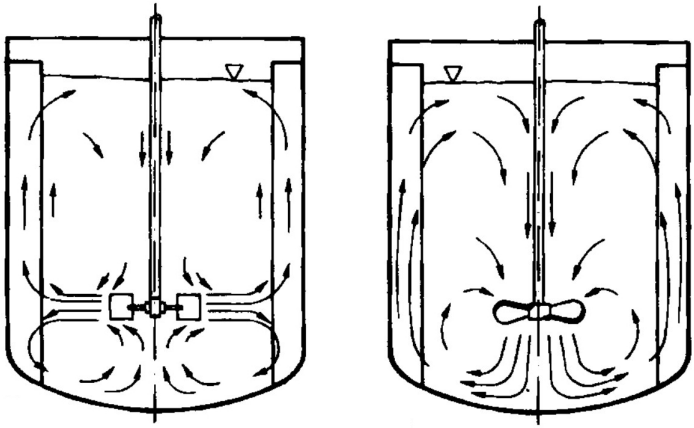

Figure 2.3.: Flow patterns caused by a Rushton turbine impeller (left) and pitched blade impeller (right) [Zlo01]

One notable characteristic of the Biostat STR 200 and other SU-STR is a lack of baffles. This is due to the impracticability of fitting single-use bioreactor bags with internal baffles. Inserting reusable external baffles into the cultivation container would defeat the purpose of utilizing a single-use bioreactor as these baffles would need to be sterilized and cleaned.

2.2. Lagrangian Sensor Particle Designs

Development of Lagrangian Sensor Particles (LSP) and methods of spatial tracking are topics of active research by multiple teams around the world. In this section, an overview of the most recent teams is given.

2.2.1. Lauterbach et al.

The Lagrangian sensor motes developed by Lauterbach et al. (TU Dresden) are equipped with a thermometer and able to send the measured data to an external computational unit in real time for recording and evaluation from inside a bioreactor. The motes, called Sens-o-Spheres have a diameter of 7.9 mm and an adjustable density [Lau19] (Figure 2.4).

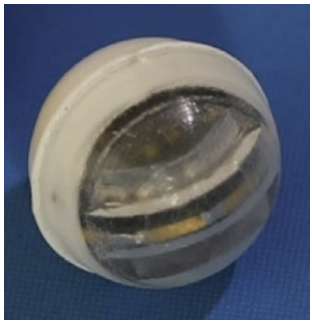

Figure 2.4.: LSP designed by Lauterbach et al. [Lau19]

A density of 1050 kg $\cdot$ m^{-3}, is determined via simulation to facilitate an even distribution of LSP throughout a 2 L Stirred Tank Reactor. As this density is significantly higher than the density of water at standard conditions, non-optimal flow following behavior is expected. Simulations of LSP positions over time have been performed, but no particle tracking velocimetry has been implemented. During experiments at the Institute of Multiphase Flows (IMS) (TU Hamburg) the LSP have been adjusted to a density of 1000 kg $\cdot$ m^{-3} to improve flow-following behavior.

2.2.2. Reinecke et al.

The sensor motes developed by Reinecke et al. (Helmholtz-Zentrum Dresden-Rossendorf, Fraunhofer-Institut für Keramische Technolo-

gien und Systeme) based on an initial design by Thiele et al. contain a temperature sensor, a pressure sensor to determine vertical position based on hydrostatic pressure and a magnetometer [Rei16] (Figure 2.5).

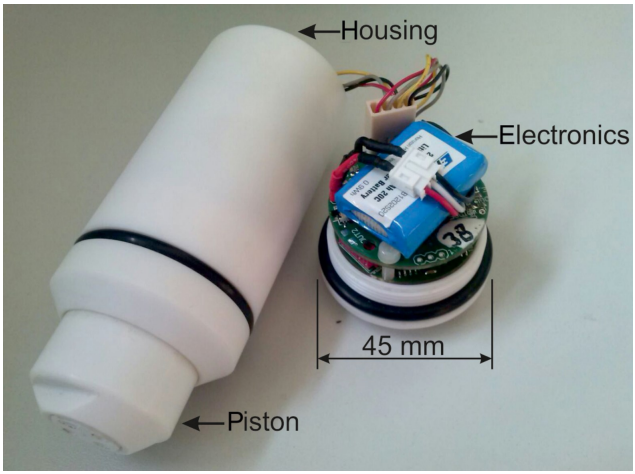

Figure 2.5.: LSP designed by Reinecke, Thiele et al. [Rei16]

The sensor motes are cylindrically shaped, with a diameter of 45 mm and a variable length. The minimal volume of the mote is $1.5 \cdot 10^{-4}\ m^3$ and its minimum density is 967 kg $\cdot$ m^{-3}. In this state, the motes equivalent spherical diameter is 6.6 mm and its sphericity 0.9. The density of the sensor motes can be increased up to 1873 kg $\cdot$ m^{-3} by inserting stainless steel weights. To increase flow-following behavior by becoming neutrally buoyant the mote can automatically increase its length and thus volume using a piston connected to an electric motor inside. Detection of the sensor mote's vertical position is implemented by using the on-board pressure sensor to determine submersion depth based on hydrostatic pressure. The horizontal movement of the mote is measured utilizing a submersible

coil at a fixed location inside of the reactor generating a magnetic field that can be measured by the mote's magnetometer on every pass, thus giving a binary representation of the mote's horizontal circulation time. A code to reconstruct the attitude and acceleration of a separate LSP from the data measured by an inertial measurement unit (IMU) is being developed with the goal of obtaining velocity and position of the LSP from the IMU's data [Bun20].

2.2.3. Zimmermann et al.

The LSP designed by smartINST S.A.S. and analysed by Zimmerman et al. is called smartPART (Figure 2.6). The diameter of the mote is 25 mm and it has an adjustable density. The LSP incorporates a 3D-accelerometer. The data recorded by the accelerometer is sent to an external computational processing unit via radio waves.

Figure 2.6.: LSP designed by smartINST S.A.S. [Zim13b]

An experiment was conducted measuring the orientation and position of the sensor mote visually and comparing the results to the data obtained by the mote's accelerometer. The accelerometer's data was adjusted for gravitational acceleration using the rotational data recorded visually and had good agreement with the acceleration calculated from visually attained positional data [Zim13a].

2.2.4. Bisgaard et al.

The LSP designed by Freesense ApS and deployed by Bisgaard et al. (Figure 2.7) has an outer diameter of 43 mm. The included sensors are an absolute pressure sensor, a thermocouple to measure temperature and a pH-sensor [Bis21b].

Figure 2.7.: LSP designed by Freesense ApS [Bis20]

In characterisation experiments, the density of the LSP was adjusted to match that of the surrounding water at 998 $\mathrm{kg\,m^{-3}}$ [Bis21a]. Determination of the LSP position was done for the vertical direction only. This was done utilizing data recorded by the pressure sensor to calculate the height of the liquid column above the LSP based on calculations for the hydrostatic pressure. Circulation times of the LSP were found to have a high correlation with measurements of the mixing time carried out via homogenization of chemical tracers.

2.2.5. Stine et al.

The LSP developed by Stine et al. is called bPod and has an outer diameter of 60 mm (Figure 2.8). Integrated into the system is a dissolved oxygen sensor. Measured data is sent to an external receiver via Bluetooth at a frequency of 2.45 GHz [Sti20].

Figure 2.8.: bPod LSP designed by Stine et al. [Bis20]

Validations for the dissolved oxygen sensor were performed in a 2 L and 10 L reactor for various dissolved oxygen concentrations. The sensor showed a linear current response in correlation with the dissolved oxygen concentration [Sti19].

2.2.6. Stewart, Wang et al.

The LSP designed by Stewart, Wang et al. has an outer diameter of 28 mm and contains a temperature sensor and a light-emitting diode (LED) [Ste15] (Figure 2.9).

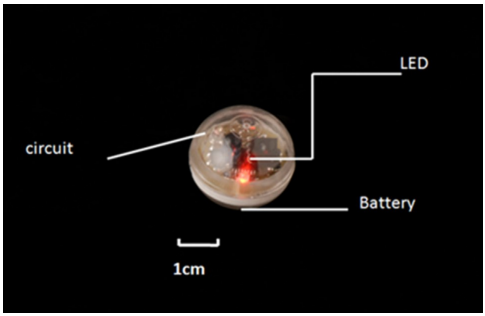

Figure 2.9.: LSP designed by Stewart et al. [Wan16]

Tracking of the 3D-position of the LSP inside of a glass tank was achieved using a single camera and a mirror. Figure 2.10 shows the experimental setup used in experiments by Stewart et al.

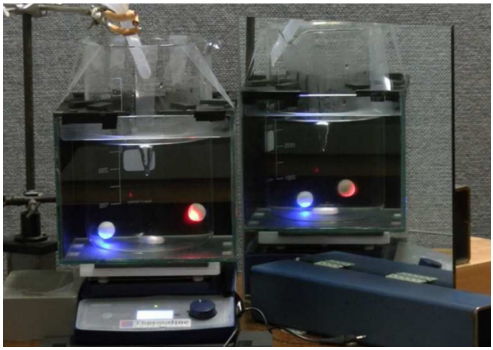

Figure 2.10.: 3D-position tracking setup utilized by Stewart et al. [Ste15]

Additionally, the LSP trajectories were visualized via photography with high exposure times to detect particle trapping behavior [Wan16].

2.2.7. Hofmann et al.

The LSP designed by Hofmann et al. at the Institute for Multiphase Flows in tandem with the LED Motes utilized in this work have a diameter of 40 mm and are adjusted to a density range of 2 $\mathrm{kg\,m^{-3}}$ to 7 $\mathrm{kg\,m^{-3}}$ higher than the fluid phase (Figure 2.11. The adjusted density range for experiments conducted in deionized water at a temperature of 37 °C and a fluid density of 994.8 $\mathrm{kg\,m^{-3}}$ was 996.7 $\mathrm{kg\,m^{-3}}$ to 1001.7 $\mathrm{kg\,m^{-3}}$. They are outfitted with two LEDs and an inertial measurement unit (BlueDot BNO055 9-Axis) or a pressure sensor (LPS33HW MEMS).

Figure 2.11.: LSP designed by Hofmann et al.

Experiments have been performed in the 200 L reactor used for this study and in a 15000 L acrylic glass reactor.

2.2.8. Summary

Table 2.1 shows a summary of LSP dimensions and densities.

Table 2.1.: Summary of basic LSP attributes

Group	**Diameter** mm	**Sphericity** -	**Density** $\mathrm{kg\,m^{-3}}$
Lauterbach	7.9	<1	1000 - 1050
Reinecke	45, var. length	≥ 0.9	967 - 1873
Zimmermann	25	1	-
Bisgaard	43	1	998
Stine	60	<1	-
Stewart	28	1	-
Hofmann	40	1	995 - 1002

2.3. Dimensionless Numbers

Dimensionless Numbers are used to characterize systems and predict their behavior. As the predictions made by Dimensionless Numbers are applicable regardless of scale, they can be used for up- and down-scaling of systems [Rub21].

2.3.1. Stokes Number

Particles that are spherical, neutrally buoyant and have an extremely small diameter follow the same trajectories as infinitesimal fluid elements [Oue08]. However, as LSPs have a relatively large size compared to the smallest flow scales of the surrounding fluid these conditions are not met. As such LSPs instead behave as inertial particles and changes in their velocity lag behind changes in the velocity of the surrounding flow field. This behavior of an inertial particle in a moving fluid is described by the Stokes Number St and defined as

$$St = \frac{\tau_\mathrm{p}}{\tau_\mathrm{f}} \ . \tag{2.1}$$

Here τ_p is the momentum response time of the particle and τ_f the characteristic time of the flow field.

The momentum response time τ_p of a particle can be interpreted as the time the particle takes to respond to changes in the velocity of the surrounding fluid. The characteristic time of the flow field τ_f can be interpreted as the timescale at which the fluid changes velocity through external influences [Rei12]. As such, for low Stokes Numbers ($St \ll 1$) the time the particle takes to adjust to changes in the fluid velocity is much smaller than the timescale at which those changes in fluid velocity occur and the particle can be said to be flow-following [Cro12]. In the opposite case of very high Stokes Numbers ($St \gg 1$), the time the particle would take to adjust to the changes in velocity of the surrounding fluid is much greater than the timescale at which these changes in velocity actually occur, and as such the particle can

be said to be mostly unaffected by, and thus not follow, the flow of the fluid. When designing a LSP or other tracking particle with the goal of achieving flow-following behavior, it is therefore important to reach as low a Stokes Number as feasible to ensure that observed particle velocities are close to the velocities of the surrounding fluid.

According to Reinecke et al. [Rei12], the characteristic time of the flow field τ_f for Stirred Tank Reactors is estimated by equation 2.2.

$$\tau_\mathrm{f} = \frac{d_2}{v_\mathrm{tip}} \tag{2.2}$$

Here, d_2 is the diameter of the impeller and v_tip the tip speed of the impeller blades. The tip speed is calculated as

$$v_\mathrm{tip} = f_\mathrm{rot} \cdot d_2 \cdot \pi \ , \tag{2.3}$$

with f_rot being the frequency of rotation. From equations 2.2 and 2.3 it follows that the characteristic time of the flow field can be roughly estimated as

$$\tau_\mathrm{f} = \frac{1}{f_\mathrm{rot} \cdot \pi} \tag{2.4}$$

As the characteristic time of the flow field τ_f cannot be influenced through the tracking particle design, the only feasible way to influence the resulting Stokes Number for tracking particles in a Continuously Stirred Tank Reactor is to reduce the momentum response time of the employed particle.

The momentum response time τ_p can be derived from the equation of motion for a spherical particle in a fluid and equals

$$\tau_\mathrm{p} = \frac{\rho_\mathrm{p} \cdot D^2}{\mu_\mathrm{f} \cdot 18} \cdot \frac{24}{C_\mathrm{D} \cdot Re_\mathrm{p}} \ , \tag{2.5}$$

as detailed in Crowe et al. [Cro12]. In this equation, ρ_p is the density of the particle, D the particle diameter, μ_f the dynamic viscosity of the fluid, C_D is the drag coefficient and Re_p the particle

Reynolds Number. A correlation for calculating the drag coefficient for spherical particles, according to Haider and Levenspiel [Hai89], for $Re_\mathrm{p} < 2.6 \cdot 10^5$ is defined as

$$C_\mathrm{D} = \frac{24}{Re_\mathrm{p}} \cdot (1 + 0.173 \cdot Re_\mathrm{p}^{0.657}) + \frac{0.413}{1 + 16300 \cdot Re_\mathrm{p}^{-1.09}} \tag{2.6}$$

Furthermore, the particle Reynolds Number is defined as

$$Re_\mathrm{p} = \frac{\rho_\mathrm{f} \cdot D \cdot u_\mathrm{t}}{\mu_\mathrm{f}} \tag{2.7}$$

where ρ_f is the density of the fluid and u_t the terminal particle velocity [Rei12]. From Haider and Levenspiel an equation for the terminal velocity of spherical particles u_t can be estimated as

$$u_\mathrm{t} = \frac{\frac{18}{d_*^2} + \frac{3 \cdot 0.8039}{4 \cdot d_*^{0.5}}}{\sqrt[3]{\frac{\rho_\mathrm{f}^2}{g \cdot \mu_\mathrm{f} (\rho_p - \rho_\mathrm{f})}}} \tag{2.8}$$

where the dimensionless particle diameter d_* is given as

$$d_* = D \cdot \sqrt[3]{\frac{g \cdot \rho_\mathrm{f} \cdot (\rho_p - \rho_\mathrm{f})}{\mu_\mathrm{f}}} \tag{2.9}$$

with g being the gravitational acceleration.

As can be inferred from the above equations, particle diameter and particle density have an inverse relation to the Stokes Number. To design a tracking particle with a low momentum response time, and thus displaying a strong flow following behavior, the diameter should be reduced as much as feasible. The particle density should be adjusted to a value as close as possible to the density of the surrounding fluid, making it neutrally buoyant. If the particle density is lower than that of the surrounding fluid the buoyancy force will exceed that of the gravitational force and thus causing floating of the particle on the fluid.

As all parameters required for the calculation of the Stokes Number are obtainable by measurements or from literature it is not only possible to minimize the Stokes Number as far as possible, but also to arrive at an estimate for the Stokes Number for the system employed in the performed experiments (Figure 4.1).

2.3.2. Archimedes Number

The Archimedes Number Ar describes the ratio of the sinking force, and the frictional force [Hai20] and is defined as

$$Ar = \frac{\rho_\mathrm{f} \cdot (\rho_p - \rho_\mathrm{f}) \cdot g \cdot D^3}{\mu_\mathrm{f}^2} \ . \tag{2.10}$$

For high Archimedes Numbers Ar > 100, the sinking force dominates the frictional force, leading to fast sinking of the dispersed particles. For low Archimedes Numbers Ar < 100, the opposite is the case and the frictional force dominates the sinking force, meaning the particle will stay suspended for longer times [Mer98]. As such a low Archimedes Number is desired when designing a tracking particle.

3. Materials and Methods

This chapter explains the experimental setup and procedure to visually measure LED Mote trajectories in a 200 L Stirred Tank Reactor. The reactor parameters to be varied are stirrer setup and stirrer speed as well as sparger type and aeration rate.

Additionally, this chapter explains the MATLAB code used for correction of the collected data using a custom-made calibration target. Furthermore the analysis of the collected data is explained, including the process of tracking single motes through the reactor.

3.1. Experimental Setup

In order to visually measure the LED Mote positions inside of a continuously Stirred Tank Reactor (STR) the STR is made of acrylic glass and filled with deionized water to a working volume of 200 liters and placed into an outer container. Transparent acrylic glass spheres containing red LEDs are placed into the water of the reactor. The experiment is recorded using a camera at a distance of 2.1 m to the outer container.

3.1.1. 200 L Stirred Tank Reactor

The reactor used is similar to the Biostat STR 200 and is made of acrylic glass. It has a height of 0.98 m and an inner diameter of 0.59 m, giving it a height to diameter ratio of 1.7. The left and right bottom of the reactor are rounded off with a corresponding radius of 0.3 m. From the camera's point of view the front and back of the reactor is cylindrical in shape (see Figure 3.1). The reactor is seated

in an outer container that is filled with deionized water to reduce distortion and compensate for refraction through the acrylic glass. The distance between reactor and outer container is 0.1 m.

Figure 3.1 shows the reactor schematic from the front and side views.

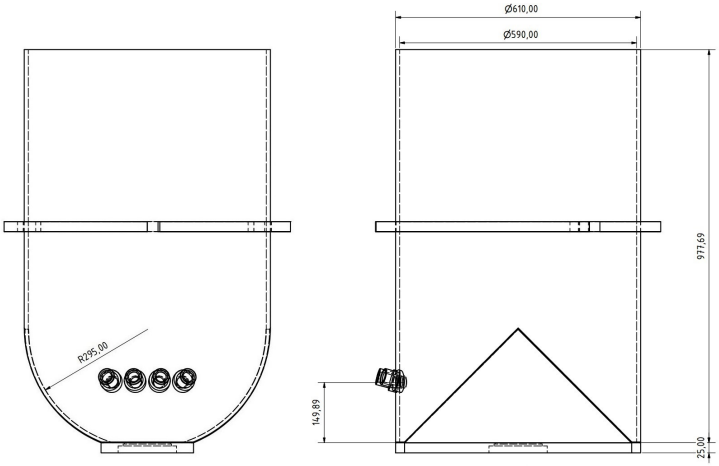

(a) Front view (b) Side view

Figure 3.1.: Schematic of the 200 L Stirred Tank Reactor

In a top entry agitator setup, the reactor is stirred using impellers connected to a shaft driven by a motor above the reactor. Two different stirrer setups have been used. The first set of impellers (RTPB) consists of a Rushton turbine impeller in the lower position and a pitched blade impeller in the upper position. Both, the Rushton turbine impeller and the pitched blade impellers have a diameter of 22.5 cm. The second set of impellers (PBPB) consists of two identical pitched blade impellers at the same positions as the impellers used in the first impeller set. Both pitched blade impellers have the same

dimensions as the pitched blade impeller used for the first setup. The distance between impellers is 0.3 m for both setups. The ratio of the stirrer diameter d_2 and the tank diameter d_1

$$R_{d2d1} = \frac{d_2}{d_1} \tag{3.1}$$

is $R_{d2d1\,Rushton} = 0.38$ for both impeller setups.

For the experiments four different stirrer speeds are used. The speeds are identical for both setups at 50 RPM, 70 RPM, 100 RPM and 120 RPM, corresponding to tip speeds $v_{tip,50}$ of 0.59 $\mathrm{m\,s^{-1}}$, 0.82 $\mathrm{m\,s^{-1}}$, 1.18 $\mathrm{m\,s^{-1}}$ and 1.41 $\mathrm{m\,s^{-1}}$ respectively.

Gas spargers at the bottom of the reactor are connected to air tubes fastened to the backside of the reactor. The used spargers are a micro sparger and a macro sparger. The micro sparger has 150 holes with a diameter of 0.15 mm. The macro sparger has 25 holes with a diameter of 0.8 mm. In addition to the unaerated case two different aeration rates are used. As such, the used aeration rates were 0 $\mathrm{l \cdot min^{-1}}$, 15 $\mathrm{l \cdot min^{-1}}$ and 20 $\mathrm{l \cdot min^{-1}}$. This corresponds to a superficial gas velocity W_m of 0.9 $\mathrm{mm\,s^{-1}}$ for an aeration rate of 15 $\mathrm{l \cdot min^{-1}}$ and 1.2 $\mathrm{mm\,s^{-1}}$ for an aeration rate of 20 $\mathrm{l \cdot min^{-1}}$ respectively. The water inside of the reactor is kept at a temperature of 20.6 °C. The density of water at a temperature of 20.6 °C is expected to be 998.01 $\mathrm{kg\,m^{-3}}$. This is confirmed using an oscillating U-tube density meter (Anton Paar GmbH). Figure 3.2 shows a visualization of adjusted experimental parameters.

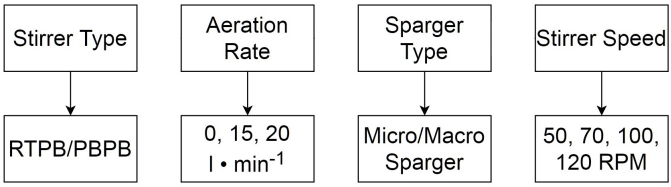

Figure 3.2.: Chart showing experimental parameters to be adjusted

3.1.2. LED Motes

The spherical LED Motes have a diameter of 25 mm and a density between 1000 $\mathrm{kg\,m^{-3}}$ and 1003 $\mathrm{kg\,m^{-3}}$. They are made up of two acrylic glass half shells containing an electrical circuit, utilizing a 220 Ω resistor, two 3 V button batteries (Camelion CR1632) and two red LEDs (Quadrios GmbH) connected in parallel. Figure 3.3 shows a schematic of the circuit diagram.

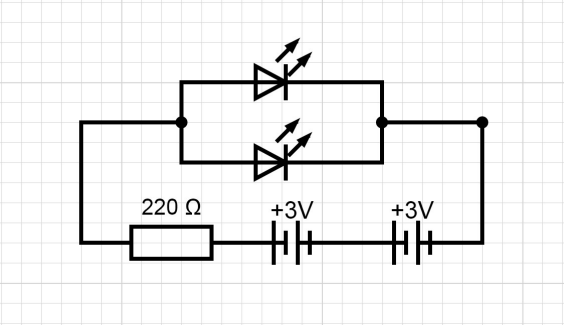

Figure 3.3.: Circuit diagram for the LED Motes

The density of the LED Motes is adjusted using cut up tin weights with an original mass of 0.6 g. The half shells and circuit were designed for this thesis. Figure 3.4 shows the computer-aided design (CAD) models of the half shells.

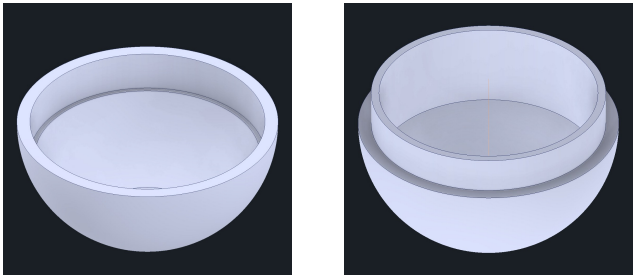

(a) (b)

Figure 3.4.: LED Mote shell top half (a) and bottom half (b)

The motes are sealed using liquid latex (Aimeili) at the half shell intersection. The experiments are conducted with 5 LED Motes in the reactor.

Figure 3.5 shows a deployed LED Mote with the circuit closed.

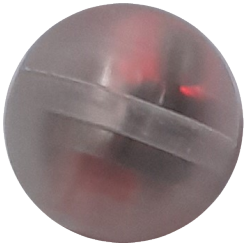

Figure 3.5.: One of the LED Motes deployed in the experiments

3.1.3. Camera setup

The Nikon D7100 camera is located 2.1 m away from the outer container at a height of 0.38 m from the reactor bottom. and fixed in place using an aluminum frame. A 35 mm camera lens with f/5.6 is used. The frame rate of the recorded video is 24 frames per second and the exposure time 1/30 s. During recording the ambient light is turned off. The LED Motes are recorded using the the camera while the reactor is stirred. Each experiment aims to record 600 s of mote trajectories. For 5 LED Motes in the reactor, this corresponds to 120 s of recording time. The base recording time of 120 s is increased if one or more LED Motes get stuck in the reactor tubing and discarded by the tracking script. Consequently, the range of recording times lies between 120 s and 210 s. The required increase in recording time is an estimate. Because of this, the actual time of recorded mote trajectories varies between experiments.

Figure 3.6 shows the filled reactor with LED Motes from the point of view of the camera for the unaerated (left) and aerated (right) case. Figure 3.7 depicts a schematic experimental setup.

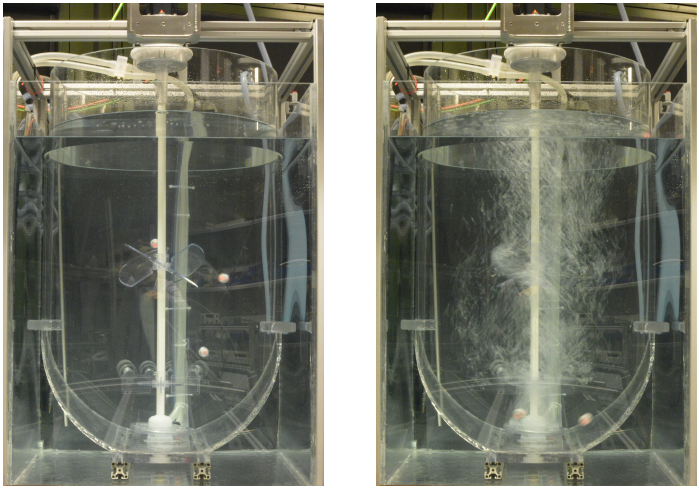

(a) (b)

Figure 3.6.: Reactor shown from the perspective of the camera, without aeration (a) and with aeration (b) at 50 RPM

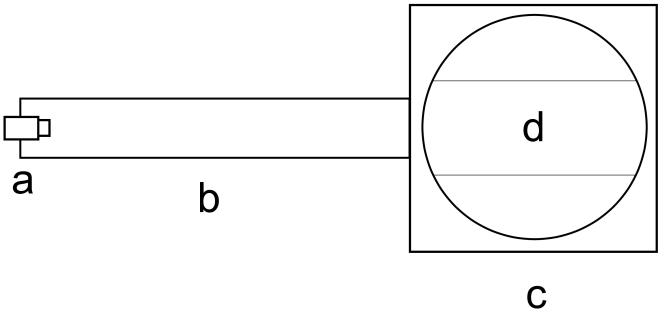

Figure 3.7.: Schematic of the experimental setup viewed from above, with camera (a), camera rail (b), outer container (c) and acrylic glass reactor (d)

3.2. Experimental Procedure

3.2.1. Mote density adjustment

Deionized water is mixed with sodium chloride (PanReac AppliChem) in two different containers at different mass ratios, producing one solution with a density of 1000 $\mathrm{kg\,m^{-3}}$ and another with a density of 1003 $\mathrm{kg\,m^{-3}}$ 20.6 °C. The sodium chloride mass concentrations of the employed solutions are first calculated using an interpolation between known density mass concentration points according to equation F.1, shown in the appendix. The densities are confirmed using an oscillating U-tube density meter (Anton Paar GmbH). The LED Motes are placed into the solutions and their floating behavior is observed. If an LED Mote sinks in both solutions, tin weights are removed from the mote in order to reduce the weight and thus the density. If the mote swims in both solutions, weight pieces are added. After weight adjustment the process is repeated until the mote swims in the higher density solution and sinks in the lower density solution. The mote is considered to have a density between 1000 $\frac{kg}{m^3}$ and 1003 $\frac{kg}{m^3}$ once this behavior is observed. Figure 3.8 shows the relationship between mote density, mote diameter and mass. The chosen range of densities is a trade-off between accuracy and adjustment time.

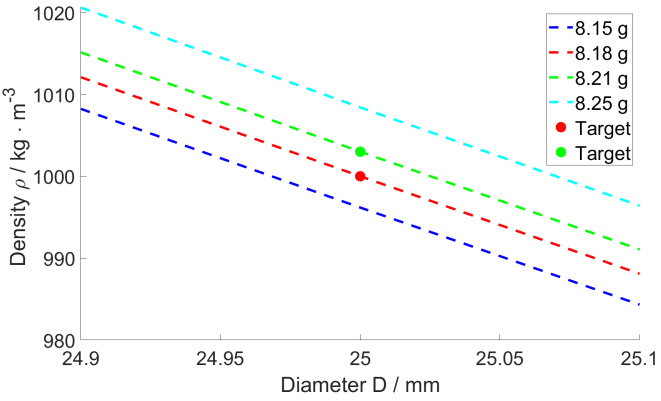

Figure 3.8.: Mote density over mote diameter at different masses

3.2.2. Calibration

It is expected that distortion will be introduced to the image through the camera lens, reactor walls or the medium, despite the refraction alignment performed by using an outer container for the reactor. A geometric calibration is performed to correct for these distortions and give a reference frame for mote positions in real space.

The calibration target (see Figure 3.9 consists of a white PVC tarp with black dots in a grid pattern supported by an aluminum frame. The target has a height of 0.9 m and a width of 0.55 m. The dots printed on the target have a diameter of 5 mm and are spaced 20 mm apart center-to-center.

Before starting the experiment, the target is placed into the reactor, with the tarp's printed side facing the camera. The reactor and calibration target are recorded with ambient light in order to obtain a reference for the reconstruction of real space coordinates from pixel coordinates in MATLAB. From that point of measurement, the camera and other equipment is not to be moved or displaced.

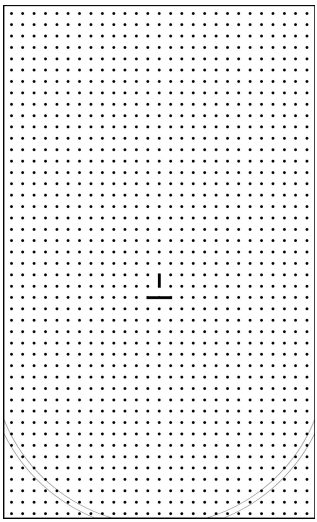

Figure 3.9.: (Raw) calibration target image. The lines at the bottom correspond to the inner and outer points of reactor bottom. The tarp is cut along the inner line and the bottom left and right sections removed to fit the particular shape of the reactor bottom.

3.3. Particle Tracking Velocimetry

The recorded video files are cut into single frames and then analysed using a MATLAB script.

Originally, a preexisting script developed by Nikki Indresh Lal (project work at the IMS (2019)) was to be used for LED Mote recognition. However the script was designed to recognize polyethylene particles with a size of 355 µm and a high seeding density. Furthermore, this 3D-Particle Tracking Velocimetry algorithm utilized a three point Gaussian fitting [Wil91] for localizing particles with aforementioned diameters and did not contain a way to remove dis-

tortion. It only utilized a manually set pixel to real world unit ratio applied uniformly across the whole image. As the LED tracking motes utilized in these experiments are not uniformly illuminated (see Figure 3.10), three point Gaussian fitting is not adequate to reliably detect particle positions. To address these challenges and attain a more robust image recognition pipeline for future projects a new particle recognition script has been developed for this thesis while still employing altered versions of previous scripts. Scripts for image pre-processing, particle location and calibration have been newly developed. Scripts for combining located particle positions into tracks and calculating their velocities and accelerations have been reused.

3.3.1. Image preprocessing

The image preprocessing script incorporates code snippets originally developed by Alexandra von Kameke. The first step of image preprocessing is the creation of a minimum image of the analysed video file. Images in MATLAB are saved in matrices with dimensions corresponding to the pixel width and height of the image. Additional dimensions are used for non-greyscale images, corresponding to the three colours red, green and blue. The values of the matrix cells correspond to the brightness of the pixel at the corresponding location in the image. To create the minimum image, the first frame of the video is copied into a working matrix. Following this, another frame is loaded and the value, and thus brightness of all corresponding pixels are compared between the currently loaded frame and the working matrix. After the comparison, the pixel with the lower intensity is saved in the working matrix. As the images used are in colour, this comparison is performed for each color separately. This process is repeated using images that are evenly spaced through the video, until the end of the video is reached. The resulting working matrix contains only the darkest pixels found in the video for each pixel position and corresponds to the minimum image of the video.

In the second step, each frame is loaded and the minimum image

matrix subtracted from the image matrix. The image matrix is then converted to greyscale and binarized according to a brightness cut-off by setting all image matrix cells with a value lower than the threshold to a value of 0 (black), and all values higher than that threshold to a value of 255 (white).

In the third step, any pixel that is inside an area completely enclosed by white pixels will also have its value set to 255.

In the fourth step, the values of all pixels outside the reactor are set to 0 by applying a mask around reactor. The reactor mask is created manually by selecting points around the reactor edge.

3.3.2. LED Mote recognition

LED Mote recognition is achieved via applying a MATLAB function to find circles of a manually set size in the preprocessed image. For each image in order, the center point coordinates of every circle are saved into a matrix, together with a value corresponding to the function's certainty of having correctly identified a circle. Any circle below an adjusted certainty threshold is discarded.

The non-discarded circles often overlap with one another, as a single near-circle in the processed image will be recognized as a multitude of circles by the MATLAB function. Additionally, a single LED Mote contains two LED and will thus create two separate bright regions in the image (see Figure 3.10 (a)). To attain a single location per LED Mote, a separate function to identify clusters is applied to the matrix containing the coordinates of the circle centers. This function labels any coordinate it identifies to be part of a cluster with a unique number corresponding to that cluster. For each identified cluster the average coordinates are calculated and saved in a new cluster matrix, effectively removing any double recognitions. This allows for the location of non-uniformly illuminated particles such as the deployed LED Motes or fluorescent particles illuminated in a half-circle pattern.

Figure 3.10 exemplifies the recognition of a single LED Mote.

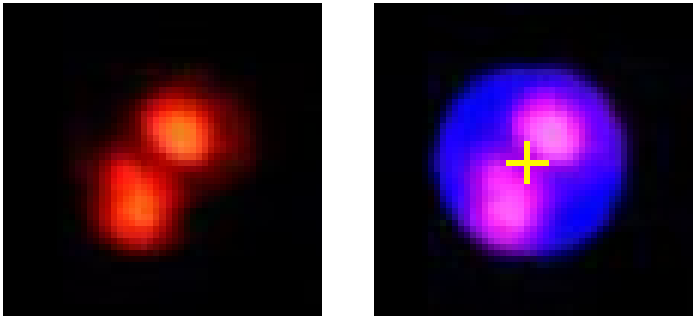

(a) (b)

Figure 3.10.: Single LED Mote with both LEDs visible. Recorded image raw (a) and with overlay showing located center position marked with a yellow cross (b).

In addition, to prevent false results from motes stuck in the reactor tubing, any mote position that is recognized for 48 frames (2 seconds of recording time) consecutively is discarded from all following frames.

For each image, the created matrix containing all mote positions is appended to an array containing the mote positions for all previous images.

Figure 3.11 shows a comparison of the raw frame image (a) and the same frame image with an overlay demonstrating the prev iously recognized LED Mote trajectories over time (b). The LED Mote near the bottom of the image is stuck, and thus automatically discarded from consideration.

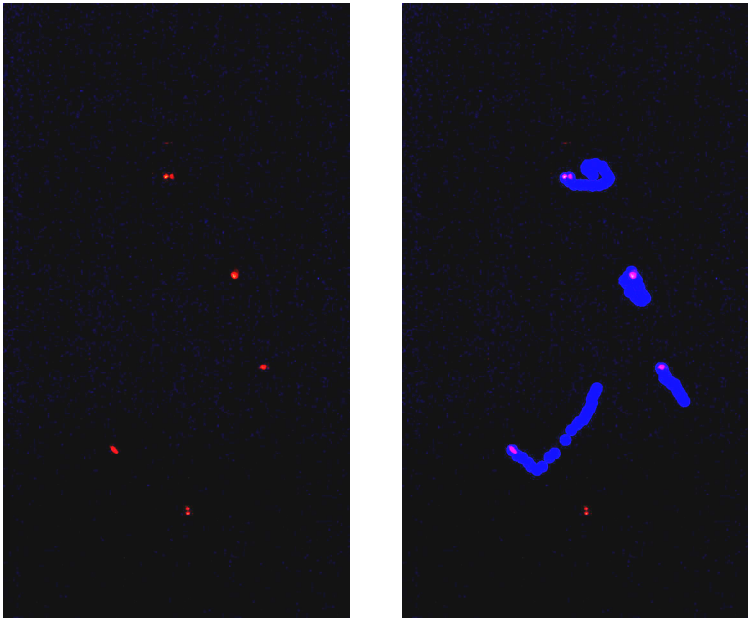

(a) (b)

Figure 3.11.: Raw frame image (a) and frame image with overlay showing mote trajectories in blue (b)

3.3.3. Image calibration

For the calibration of the script, the image of the reactor with the calibration target inside is loaded. The printed dots are recognized using the same procedure as is used in the particle recognition step. After automatic recognition, any falsely recognized points are manually removed and missing points added. The manual adjustment is done visually as the recognized dots are displayed on top of the analysed image. Figure 3.12 shows the raw image of the reactor with

calibration target inserted (a) and the image displayed for manual adjustment, displaying automatically recognized target dots in white (b).

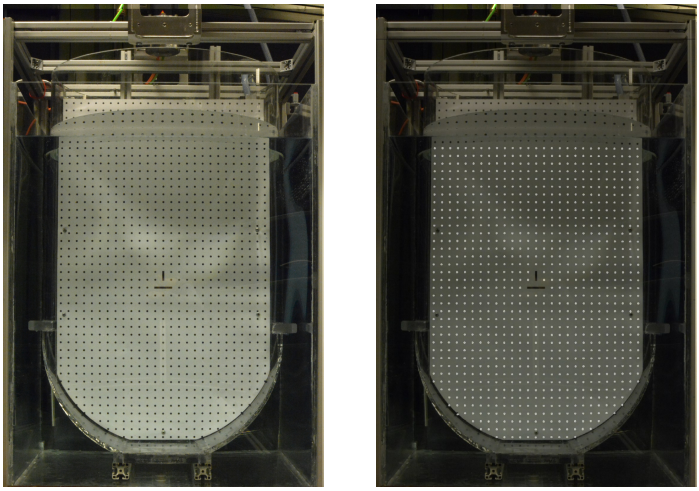

(a) (b)

Figure 3.12.: Image of the reactor with calibration target inserted raw (a) and with automatically recognized target dots (b)

After the final adjustment, all points are saved into a n-by-2 matrix. In this matrix the rows correspond to the found points. The first column corresponds to the respective X-coordinate and the second column corresponds to the Y-coordinate. The matrix is then split into two n-by-1 vectors. Each dot on the calibration target can uniquely be assigned to exactly one column and one row. To find the column and row of each point, a function to identify clusters in data is applied to the two vectors separately. As the X-coordinates of all points compromising a single column are roughly equal, points of the

same column will be sorted into the same cluster. The same process is executed for the Y-coordinates to sort the points into rows.

After each dot is assigned to exactly one row and one column, the results are visually checked for errors by displaying the analysed image and coloring in the rows and columns separately. If any of the dots are falsely categorized into a certain row or column, the calibration process is repeated using adjusted setting parameters. If no errors are found, the resulting rows are saved to one array and the columns to another.

3.3.4. Image distortion removal and translation into real space

To translate the pixel coordinates gained through the steps outlined in the LED Mote recognition into coordinates in real space, adjustments have to be made based on the calibration data.

To facilitate this, for every found point in every frame the two target rows with the closest average Y-position to the point's Y-position and the two target columns with the closest average X-position to the currently translated point's X-position are found and saved separately.

For each of the rows and columns, the closest two points on that row or column to the currently translated point are found and saved to an array. Figure 3.13 shows a schematic of the above step.

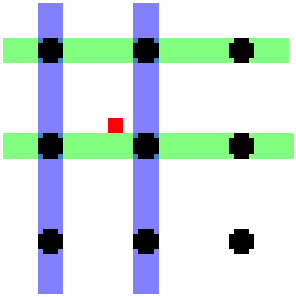

Figure 3.13.: Translated point (red), target dots (black), closest two columns (blue) and closest two rows (green)

Additionally, for each of these two rows and two columns, a new vector is created with the same length as the corresponding row or column. The values of these vectors contain the real world positions of the corresponding dot-centers and are generated based on the knows distance between dots on the calibration target.

As such, each of the two dots per row or column is assigned a position in real space. With these assignments, an interpolation in multiple steps is conducted. In the first interpolation step, an estimate of the point's real world position is calculated for each of the two rows and columns separately. To calculate the point's X-position, an interpolation between the two dots of the upper row is conducted. This is repeated for the two dots of the lower row. To calculate the point's Y-position, an interpolation between the two dots of the left column is conducted. This is repeated for the two dots of the right column. As such, two different X- and Y-positions are calculated respectively. These estimated positions are the real space X- and Y-positions if the point was exactly on the respective row or column used for the calculation.

The actual real space X- and Y-positions are calculated in the second interpolation step. To calculate the real space X-position of the point, an interpolation between the two calculated X-positions is done. This interpolation is conducted based on the Y-position of the

point and the two average Y-positions of the rows from which the two X-positions are calculated. This process is repeated to calculate the real space Y-position based on an interpolation between the two calculated Y-positions. The final resulting real world X- and Y-positions are saved and the next point translated until a real world position is found for every point found through the LED Mote recognition step.

3.3.5. Particle tracking

The track recognition step was originally coded by Nikki Indresh Lal within the framework of a project work at the Institute of Multiphase Flows. It employs an algorithm based on Ouellette [Oue06]. In order to implement this step to the data sets created in this work and to improve reliability of results alterations are incorporated.

After finding the real world positions of all motes for every frame, the positions together with the frame number for each position and the current length of the track are loaded into the track recognition script. For every position belonging to the first frame, a new track entry is created and saved in an array. From the second frame on, the current X- and Y-positions and the X- and Y-positions of the previous frame are saved in two new arrays. The difference between the current frame's positions and the previous frame's positions is saved as velocity array. The sum of the current frame's positions and the velocity array is saved as the array estimating the next frame's positions. For every track that has had a position added to it in the past 2 frames, the square of the differences between its estimated next X- and Y-coordinates and all X- and Y- coordinates of the current frame are calculated and the sum of the X- and Y-differences saved to a new array entry for every point. This way a measure for the distance between the estimated next track position and all positions of the current frame is found separately for each track. If only one of the resulting distances is smaller than a manually set threshold, the corresponding position is saved as the next position for this track. If there are multiple distances smaller than the threshold, the position

corresponding to the smallest distance between predicted and actual positions is saved. Considering the recognition algorithm naming scheme used by Ouellette [Oue06], this algorithm can be described as 3-Frame best estimate previous velocity.

Figure 3.14 shows a schematic of the used tracking algorithm.

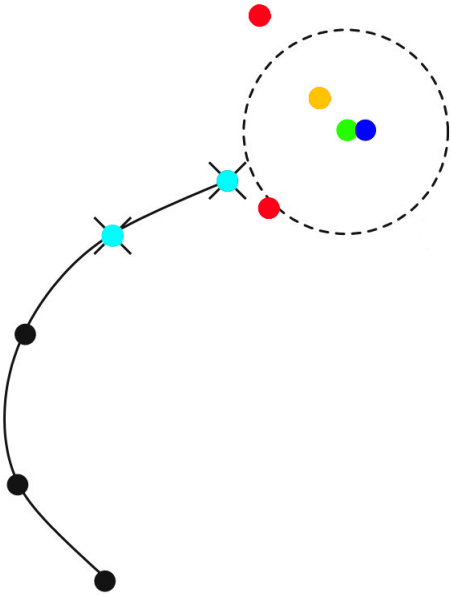

Figure 3.14.: Schematic of the tracking algorithm. Two previous track positions (turquoise), estimated next position (green), threshold radius (dotted line), best-fitting candidate (blue), less-fitting candidate (orange) and positions outside the threshold radius (red) [Oue06]

After assigning the position to a track, a search is run through all tracks to check if the matched position has previously been matched to another track. If the matched position for the current track has been matched to another track already the match to the track with the smaller distance between actual position and estimated position is kept while the other match is discarded.

All positions that remain unmatched to a track at the end of this process are saved to the track array as the beginnings of new tracks. Tracks with a length of less than 5 positions are discarded from evaluation if no new position has been added to the track for more than 2 frames.

3.3.6. Velocity and acceleration calculation

To calculate the velocity in the X-direction of a track on a certain frame, the difference between consecutive X-positions is divided by the product of the length of the frame-gap between the frames containing the positions and the inverse of the frame rate of the recording. To calculate the acceleration, the difference between two subsequent velocities is calculated and the result divided by the product of the length of the frame-gap between the frames containing the positions and the inverse of the frame rate of the recording. The same is done for the Y-positions. To calculate the resulting total velocity and acceleration, the square root of the sum of the squares of the radial and axial velocities and accelerations respectively is taken.

4. Results and Discussion

This chapter contains the results and discussions of the calculations of dimensionless numbers as well as the evaluation of the performed experiments and discusses them. Furthermore the evaluation is divided into three parts. The first part demonstrates the general trends in mean velocity and acceleration with changing reactor parameters, the second shows sets of experiments performed under the same reactor parameters with exception of the stirrer speed and the third regarding distributions of evaluated parameters across the 2D plane.

4.1. Stokes Number

By means of equation 2.1 it is possible to estimate the Stokes Number for the chosen setup. Figure 4.1 shows the estimated Stokes Numbers for the utilized stirrer speeds and the chosen LED Mote dimensions and densities.

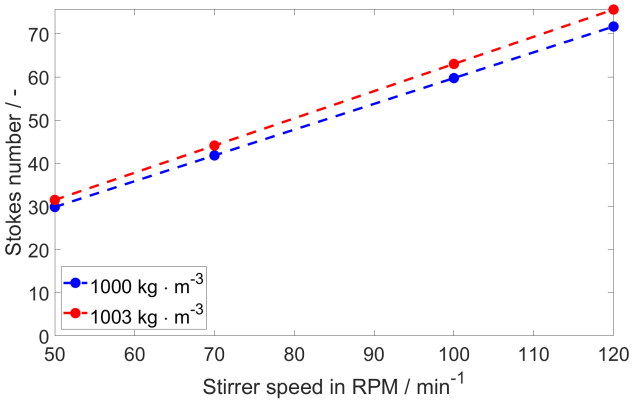

Figure 4.1.: Stokes Number as a function of stirrer speed at particle densities of 1000 kg·m^{-3} and 1003 kg·m^{-3}, representing the outer bounds of the employed LED Mote densities.

With a calculated particle Reynolds Number of 43 for a density of 1000 $kg \cdot m^{-1}$ and 38 for a density of 1003 $kg \cdot m^{-1}$, the estimated Reynolds Number is well below the upper limit of $Re_{\mathrm{p}} < 2.6 \cdot 10^5$ for the calculation of the drag coefficient according to the equation by Haider and Levenspiel [Hai89] and thus the estimated Stokes Number is valid for the encountered flow regime.

As the estimated Stokes Numbers are much bigger than 1, it is unlikely that the chosen LED Motes are able to track turbulence on a micro-scale due to a much higher response time. However, Reincke et al. [Rei12] has shown that tracking mote velocities can still reflect the dominant flow phenomena despite the system possessing a Stokes Number much higher than 1.

4.2. Archimedes Number

Figure 4.2 shows the calculated range of Archimedes Numbers for the LED Motes deployed in the experiment, as well as theoretical values for altered particle diameters and densities.

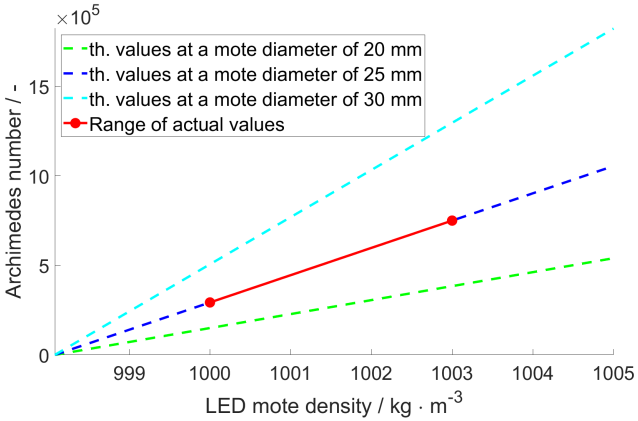

Figure 4.2.: Archimedes Number over particle density for particle diameters of 20 mm, 25 mm and 30 mm. The motes employed in all experiments have a diameter of 25 mm.

As evident from the above figure, the Archimedes Number is much greater than 100 for the entire range of employed LED Mote densities. As such, gravitational forces dominate drag forces and there is a possibility of inhomogeneous suspension of LED Motes due to sinking. This should be considered when evaluating the following results, especially at low stirrer speeds.

4.3. General trends over parameter changes

In total, 40 experiments were conducted. The varied parameters were the stirrer speed, the stirrer type, the aeration rate and the sparger type. The stirrer speeds used are 50 RPM, 70 RPM, 100 RPM and 120 RPM, corresponding to tip speeds $v_{tip,50}$ of 0.59 $\mathrm{m\,s^{-1}}$, 0.82 $\mathrm{m\,s^{-1}}$, 1.18 $\mathrm{m\,s^{-1}}$ and 1.41 $\mathrm{m\,s^{-1}}$ respectively. Each experiment is run for a base time of 120 s. The recording time is increased if any LED Motes get stuck in the reactor tubing and are discarded by the script. Consequently, the range of recording times lies between 120 s and 210 s. Additionally, for velocity and acceleration calculations, some positions are not evaluated due to belonging to tracks with a length less than 5. Because of these reasons, the number of evaluated data points differs between experiments.

4.3.1. Changes in stirrer speed and stirrer type

In this subsection all 40 experiments are compared regarding the influence of the stirrer speed and stirrer type on the mean velocity and acceleration magnitudes. Mean velocity and acceleration magnitudes are calculated according to Equation F.2. Error bars are shown. As expected, both mean velocity and acceleration magnitudes derived from the evaluation of experimental video data show a trend towards higher velocity and acceleration magnitudes with increasing stirrer speeds, as seen in Figure 4.3.

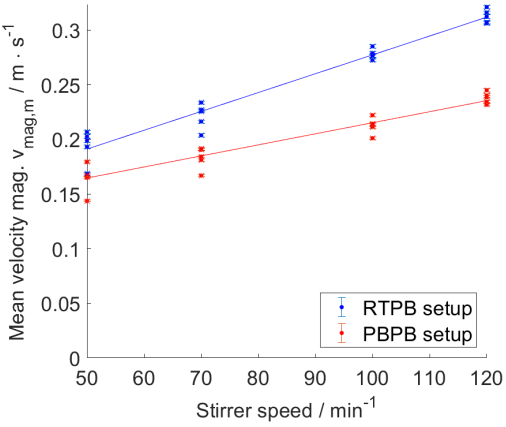

(a)

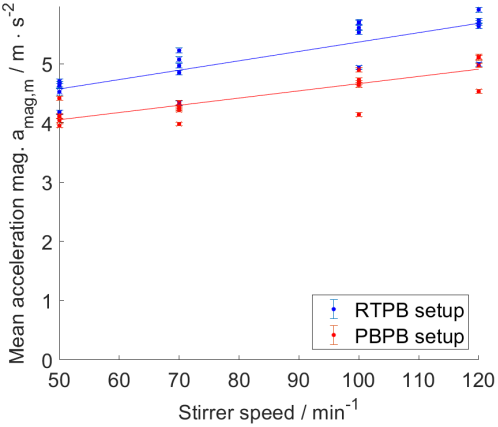

(b)

Figure 4.3.: Scatter plot of calculated mean velocity magnitudes $v_{mag,m}$ (a) and acceleration magnitudes $a_{mag,m}$ (b) as a function of stirrer speed

Additionally, the data shows consistently higher velocities and accelerations in experiments utilizing the Rushton turbine impeller and pitched blade impeller (RTPB) setup (blue dots) than in those performed with the double pitched blade impeller (PBPB) setup (red dots). The trends for the two stirrer setups calculated using a linear regression model are displayed in the respective data color. The trend line for the RTPB setup shows a stronger correlation between RPM and calculated mean velocity than that of the PBPB setup, resulting in a steeper increase in mean velocity when increasing the impeller speed. This effect is not observed to a statistically relevant degree in the calculated mean acceleration magnitudes, at which the difference in rates of change between the two trends falls within the margin or error. Despite not showing a stronger correlation between stirrer speed and mean acceleration, the RTPB setup still produces consistently higher mean calculated accelerations, suggesting a fundamental difference in flow behavior through the reactor might be responsible for the observed difference in mean acceleration magnitudes.

4.3.2. Changes in sparger type and aeration rate

In this subsection all 40 experiments are compared regarding the influence of the sparger type on the mean velocity and acceleration magnitudes. The mean calculated velocities and accelerations in relation to the rate of aeration are shown in Figure 4.4.

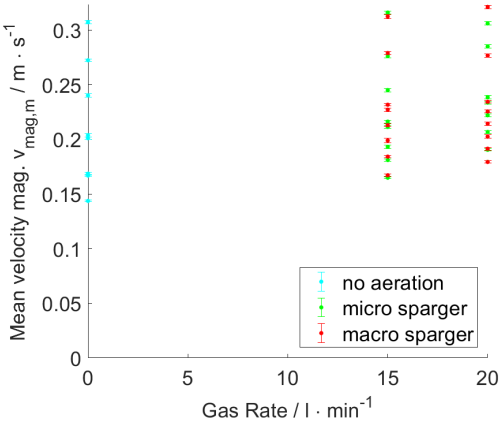

(a)

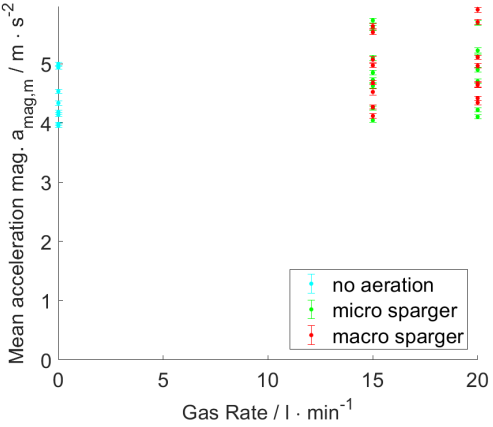

(b)

Figure 4.4.: Scatter plot of calculated mean velocity magnitudes $v_{mag,m}$ (a) and mean acceleration magnitudes $a_{mag,m}$ (b) as a function of aeration rate for different sparger types

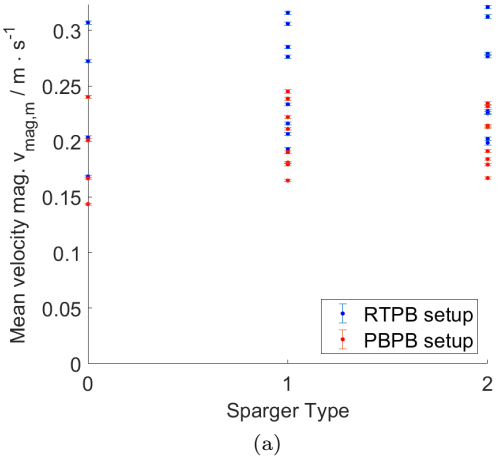

(a)

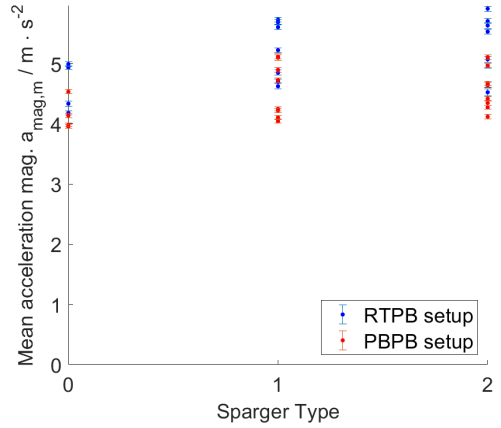

(b)

Figure 4.5.: Scatter plot of calculated mean velocity magnitudes $v_{mag,m}$ (a) and mean acceleration magnitudes $a_{mag,m}$ (b) between the two sparger types

The evaluation shows a very small trend towards rising velocities and accelerations with higher gas rates, though with a sample size of only 40 experiments and a large range of calculated means compared to the observed trend the likelihood of a statistical error is high. Figure 4.5 shows the velocities and accelerations in relation to the two sparger types as well as the unaerated setup without the distinction by aeration rate. The unaerated state is denoted by the value 0, the micro sparger is denoted by the number 1 and the macro sparger is denoted by the number 2. No statistically significant trend of velocity or acceleration in relation to the employed sparger type is observed. Means derived from experiments utilizing the RTPB stirrer setup are colored blue, those from experiments utilizing the PBPB stirrer setup are colored red. The sparger type does not appear to have an influence on the previously observed trend of higher velocities and accelerations when utilizing the RTPB stirrer setup over the PBPB stirrer setup.

4.4. Comparison of representative sets of parameters

To get a more granular understanding of the flow behavior of the LED Motes inside the reactor, the following sections contain figures showing the velocities and accelerations along the two principal axis of the reactor from the point of view of the camera. For brevity, representative combinations of reactor parameters are shown. The micro sparger with an aeration rate of 20 $\mathrm{l} \cdot \mathrm{min}^{-1}$ was chosen as representative for the aerated case because a bubble size distribution tending towards smaller diameters is generally favorable for fermentation processes and processes aiming for high rates of mass transfer. Furthermore, a higher aeration rate is predicted to increase the visibility of any trends emerging through aeration processes. Additionally a high aeration rate would depict a feasibility study on the recognition algorithm to evaluate LED Motes during poor visibility conditions. The mean velocity and acceleration magnitudes as well

as their calculated uncertainties are displayed separately for each experiment. The bin size for all figures, along both spacial axis is 30 mm. For each bin the mean magnitude values within that bin are shown. Higher uncertainties are calculated for positions near the edges of the evaluated area as the count of evaluated LED modes registered in these regions is low for some recordings.

4.4.1. Velocity over reactor width

Figures 4.6 and 4.7 show the mean velocity magnitudes of LED Motes over the reactor width, also called radial position, within the reactor for representative sets of reactor parameters.

Comparing the velocities in experiments utilizing the RTPB stirrer setup with those for experiments utilizing the PBPB stirrer setup, two observations can be made. Firstly, the influence of the stirrer speed on the velocities inside the reactor is, as previously noted, stronger for the RTPB stirrer setup, however the distribution of velocities across the width of the reactor appears much more uniform for the PBPB stirrer setup. Observed velocities are trending to be greater towards the middle of the reactor for all shown sets. This is likely being caused in part by the projection of circular movement onto the camera's plane of view. Additionally, this effect is likely compounded by the absence of baffles in the reactor. While the reactor tubing acts in a way similar to a baffle, it is unlikely to compensate for the lack of multiple baffles, as used in traditional STR. As such a higher degree of tangential flow in the reactor is expected as there are no baffles to redirect the flow into the axial direction. The degree of the observed trend differs strongly between the two stirrer setups and between stirrer speeds. The difference between the highest and lowest observed velocities for 120 RPM in Figure 4.6 (a) and (b) is greater than 0.2 $\mathrm{m\,s^{-1}}$, while it is approximately 0.1 $\mathrm{m\,s^{-1}}$ for the same RPM in Figure 4.7 (a) and (b). As such, this effect is unlikely to be purely caused by the projection of 3D velocities onto a 2D plane as this would cause a uniform skewing of velocities across all experiments.

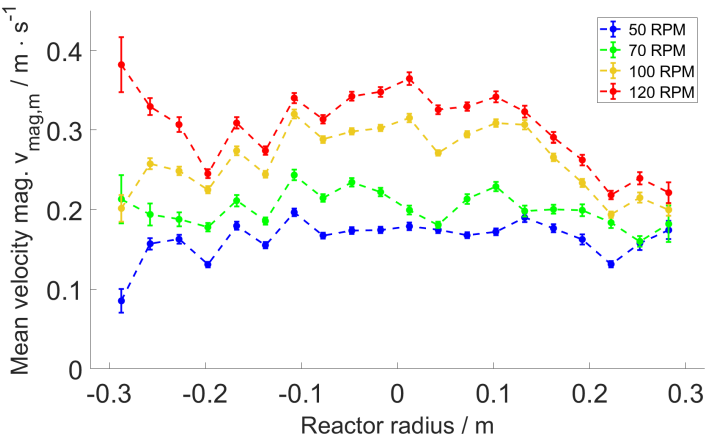

(a) RTPB, no aeration

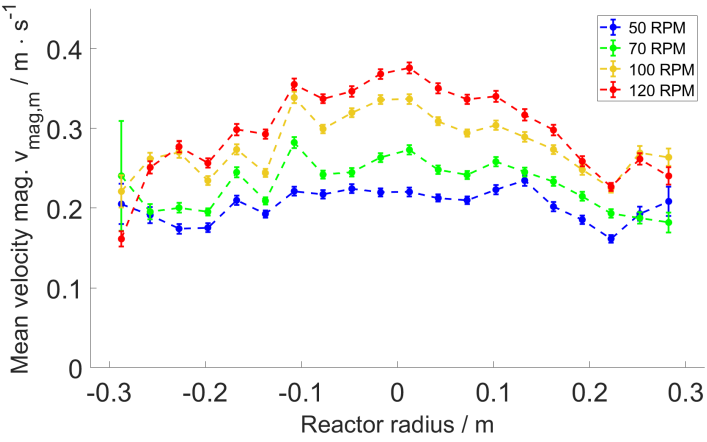

(b) RTPB, micro sparger, 20 l · min^{-1}

Figure 4.6.: Line plot of calculated mean velocity magnitudes $v_{mag,m}$ for the RTPB setup with no aeration (a) and an aeration rate of 20 l · min^{-1} utilizing the micro sparger (b) over reactor width

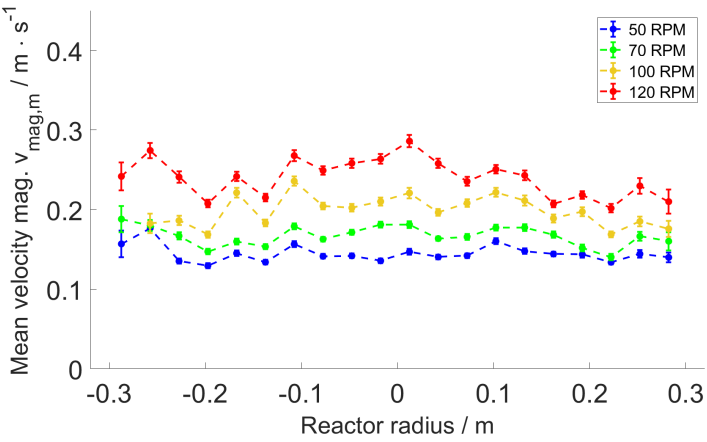

(a) PBPB, no aeration

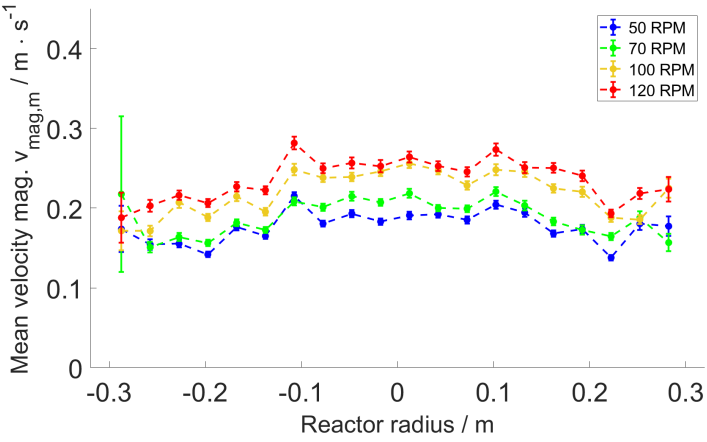

(b) PBPB, micro sparger, 20 l · min^{-1}

Figure 4.7.: Line plot of calculated mean velocity magnitudes $v_{mag,m}$ for the PBPB setup with no aeration (a) and an aeration rate of 20 l · min^{-1} utilizing the micro sparger (b) over reactor width

Secondly, another observable effect of a change in reactor parameters, namely between the unaerated and aerated states, is an increase in velocities for lower stirrer speeds when aerating compared to the unaerated state. This increase in mean velocity magnitudes is not observed for higher stirrer speeds, and is thus lowering the influence of the stirrer speed on the velocity inside of the reactor. The increase of velocities for lower RPMs can be explained by the reduced energy input through the stirrer, making mixing effects caused by rising bubbles of air more pronounced, while at higher stirrer speeds the velocity field of the reactor would be more strongly dominated by the rotation of the stirrer. Additionally for all sets of experiments an increase in velocity at a radial position of around -0.1 m and +0.1 m can be observed. Bins in this region show mean velocity magnitudes of up to 0.5 $\mathrm{m\,s^{-1}}$ higher the surrounding bins. This is likely caused by the end of the stirrer blades at that radial position.

4.4.2. Acceleration over reactor width

Figures 4.8 and 4.9 show the acceleration of LED Motes over the reactor width, or radial position, within the reactor for representative sets of reactor parameters.

The relative increase in acceleration with the stirrer speed is much weaker for the acceleration that it is for the velocity. The previously observed effect of increased velocities towards the middle of the reactor does not appear to apply to the acceleration, as LED Motes towards the middle section of the reactor are consistently accelerated less strongly than those in the immediate surrounding of the impeller blades. This reduced acceleration towards the middle is likely caused in part by the projection of the 3D movement of the LED Motes onto the 2D plane of view of the camera and suggests acceleration in the radial direction.

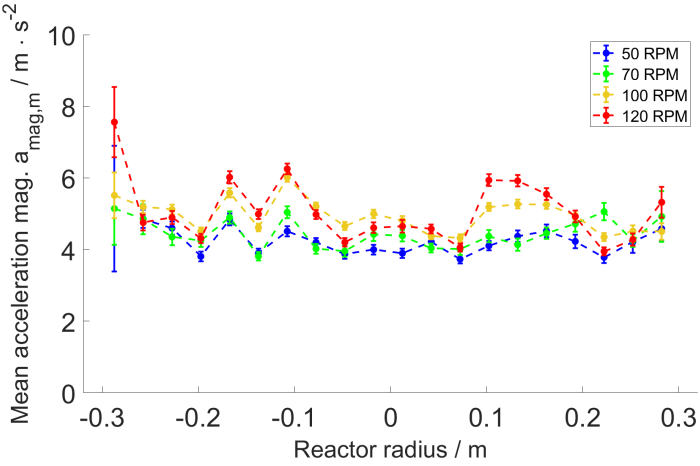

(a) RTPB, no aeration

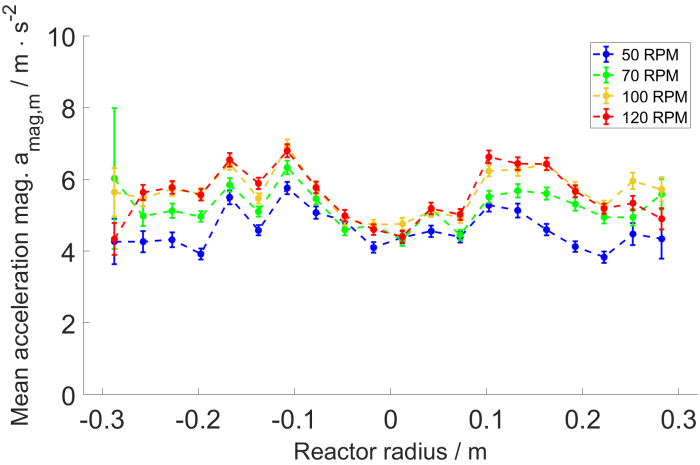

(b) RTPB, micro sparger, 20 l · min^{-1}

Figure 4.8.: Line plot of calculated mean acceleration magnitudes $a_{mag,m}$ for the RTPB setup with no aeration (a) and an aeration rate of 20 l · min^{-1} utilizing the micro sparger (b) over reactor width

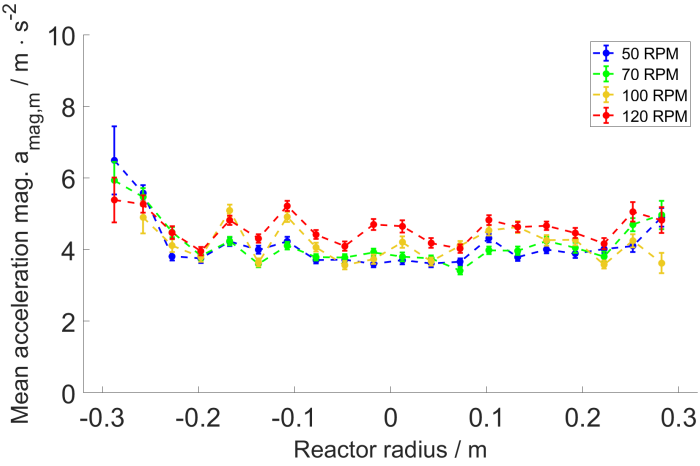

(a) PBPB, no aeration

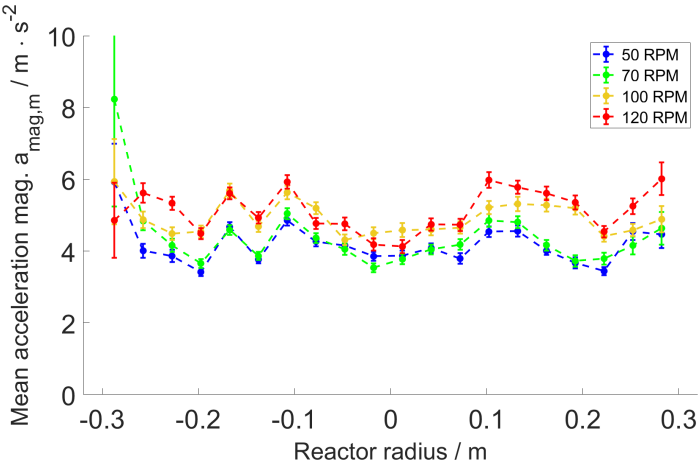

(b) PBPB, micro sparger, 20 l · min^{-1}

Figure 4.9.: Line plot of calculated mean acceleration magnitudes $a_{mag,m}$ for the PBPB setup with no aeration (a) and an aeration rate of 20 l · min^{-1} utilizing the micro sparger (b) over reactor width

As with the velocity, peaks in acceleration are registered at a radial position of around -0.1 m and +0.1 m. These peaks are likely caused by the acceleration of LED Motes hit by the stirrer blades or a current in the direct wake of the stirrer rotation. This effect is more strongly pronounced for experiments utilizing aeration, the difference being especially visible for lower stirrer speeds. Comparing the effects of the different stirrer setups, it becomes apparent that the previously observed effect of increased velocities when utilizing the RTPB stirrer setup over the PBPB stirrer setup is less pronounced for the acceleration. In addition to the generally weaker effect of the stirrer speed on the acceleration of the LED Motes, the increase in the influence of the stirrer speed on the acceleration for the RTPB stirrer setup over the PBPB stirrer setup is less pronounced than that of the increase in velocity. While not as strong, the effect can still be observed, especially for the middle section of the reactor, where the peaks at a radial positions of around -0.1 m and +0.1 m are pronounced more strongly in experiments utilizing the RTPB stirrer setup.

4.4.3. Velocity over reactor height

Figures 4.10 and 4.11 show the velocity of LED Motes over the reactor height within the reactor for representative sets of reactor parameters. Values from LED Motes appearing to be located at positions below the height of 0 m due to perspective effects are cut for clarity.

The mean velocity magnitudes over the reactor height show a stronger correlation between stirrer speed and LED Mote velocities for the RTPB stirrer setup. Additionally mean LED Mote velocity magnitudes are higher for the RTPB stirrer setup than for the PBPB stirrer setup. Once again, the velocities for lower RPM values are generally higher for the aerated cases. Experiments performed with either stirrer setup and without aeration show a trend towards lower velocities with higher LED Mote locations in the reactor. This trend is weaker for aerated cases (and lower stirrer speeds). However in Figure 4.11 (b) at 50 RPM the contrary of the trend can be observed in that the mean observed velocity is trending higher at higher vertical positions in the reactor. These trends combined lead to a high diversity of observed mean velocity magnitudes over the reactor height and over different stirrer speeds between the experiment sets. This is most visible between the experiment set performed without aeration utilizing the RTPB stirrer setup (Figure 4.10 (a)), and the set of experiments utilizing the PBPB stirrer setup and an aeration rate of 20 $\mathrm{l} \cdot \mathrm{min}^{-1}$ through the micro sparger (Figure 4.11 (b). Notably absent is the observation of persistent peaks in mean velocity magnitudes at the positions of any of the stirrers.

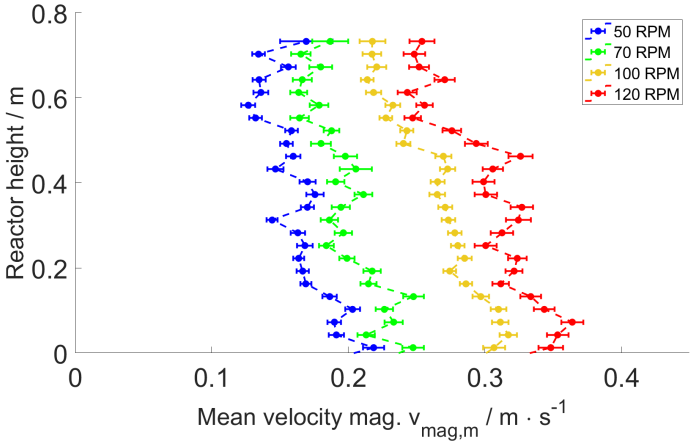

(a) RTPB, no aeration

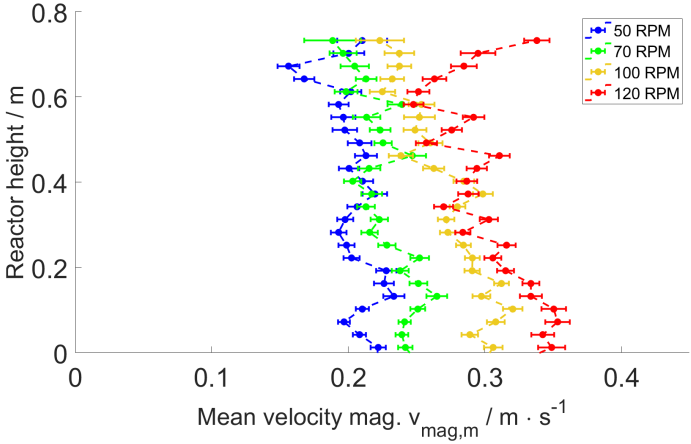

(b) RTPB, micro sparger, 20 $l \cdot min^{-1}$

Figure 4.10.: Line plot of calculated mean velocity magnitudes $v_{mag,m}$ for the RTPB setup with no aeration (a) and an aeration rate of 20 $l \cdot min^{-1}$ utilizing the micro sparger (b) over reactor height

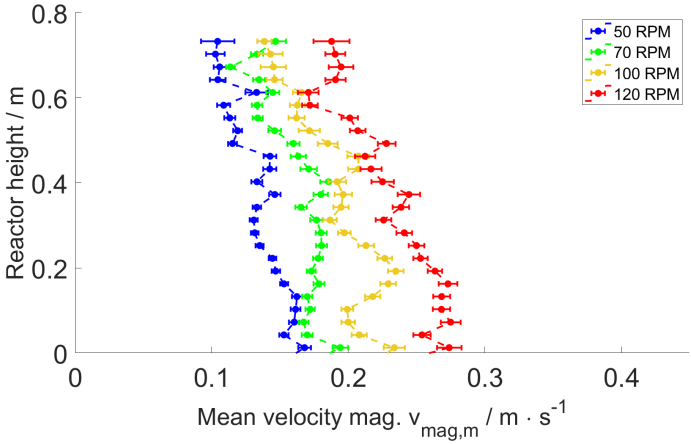

(a) PBPB, no aeration

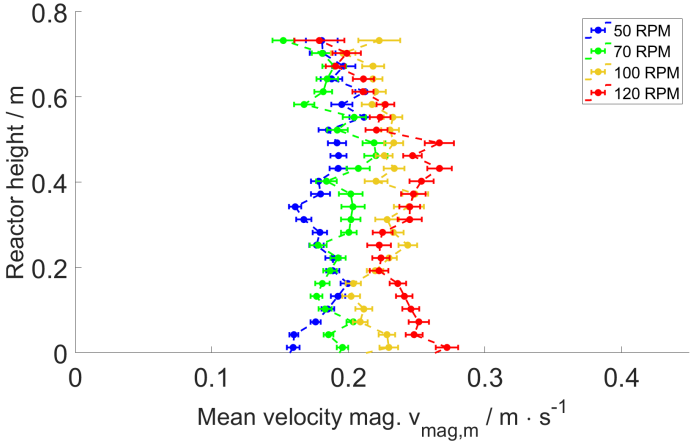

(b) PBPB, micro sparger, 20 $\mathrm{l} \cdot \mathrm{min}^{-1}$

Figure 4.11.: Line plot of calculated mean velocity magnitudes $\mathrm{v}_{\mathrm{mag,m}}$ for the PBPB setup with no aeration (a) and an aeration rate of 20 $\mathrm{l} \cdot \mathrm{min}^{-1}$ utilizing the micro sparger (b) over reactor height

4.4.4. Acceleration over reactor height

In Figures 4.12 and 4.13 the mean acceleration magnitudes of the LED Motes over the reactor height are shown for representative sets of reactor parameters. Values from LED Motes appearing to be located at positions below the height of 0 m due to perspective effects are cut for clarity.

Plotting the acceleration over the reactor height shows, similarly to the plot of the acceleration over the reactor width, a reduced relative influence of the stirrer speed on the acceleration, compared to the relative influence of the stirrer speed on the velocity. Again a general trend is shown towards higher accelerations for the aerated experiments. A trend of higher mean acceleration magnitudes of LED Motes towards the reactor bottom can be observed. The experiment performed at 50 RPM utilizing the PBPB stirrer setup and an aeration rate of 20 $\mathrm{l} \cdot \mathrm{min}^{-1}$ through the micro sparger (Figure 4.13(b)) again goes against this trend as it displays higher mean acceleration magnitudes at higher reactor positions.

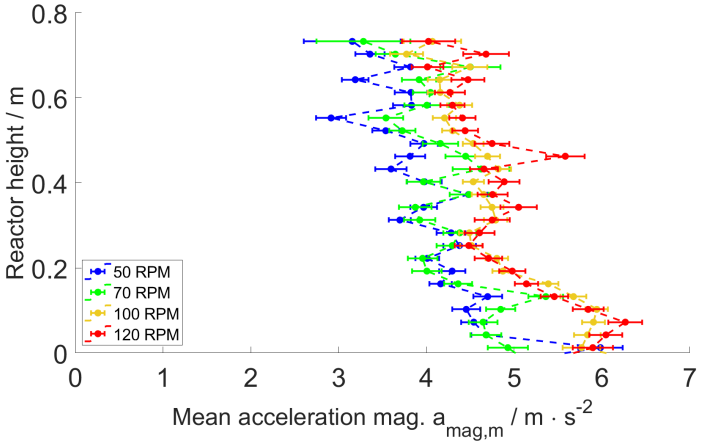

(a) RTPB, no aeration

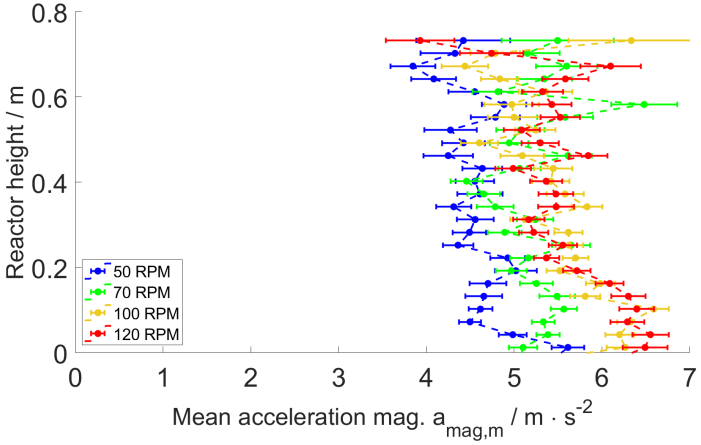

(b) RTPB, micro sparger, 20 $l \cdot min^{-1}$

Figure 4.12.: Line plot of calculated mean acceleration magnitudes $a_{mag,m}$ for the RTPB setup with no aeration (a) and an aeration rate of 20 $l \cdot min^{-1}$ utilizing the micro sparger (b) over reactor height

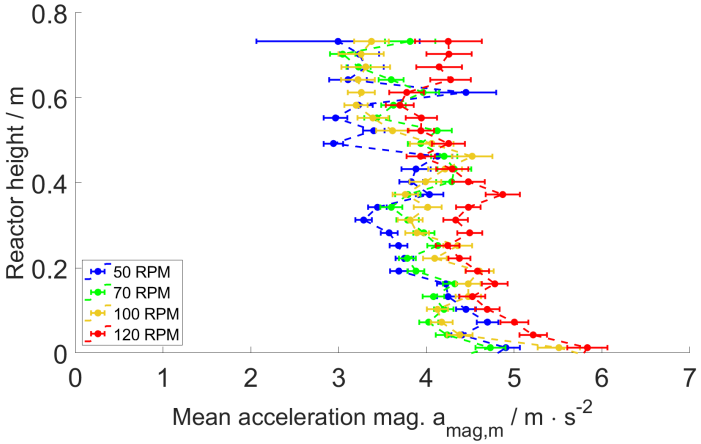

(a) PBPB, no aeration

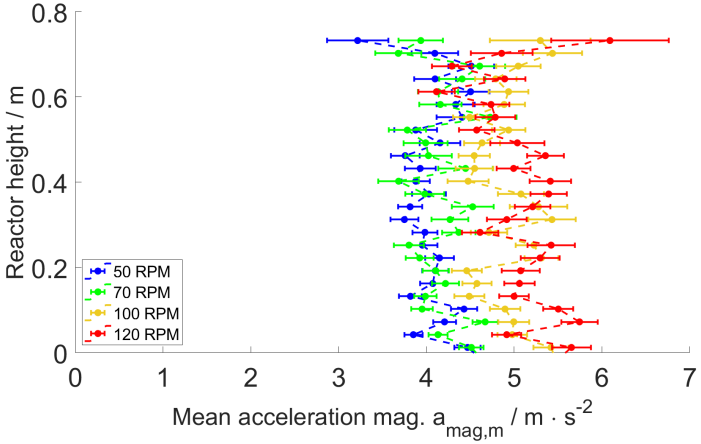

(b) PBPB, micro sparger, 20 $l \cdot min^{-1}$

Figure 4.13.: Line plot of calculated mean acceleration magnitudes $a_{mag,m}$ for the PBPB setup with no aeration (a) and an aeration rate of 20 $l \cdot min^{-1}$ utilizing the micro sparger (b) over reactor height

4.5. Evaluation of results in a 2D projection grid

In this section mean velocity and acceleration magnitudes as well as the probability density function over a 2D projection of the reactor rare displayed and discussed. In this section only experiments performed using the RTPB setup are shown. The four sub-figures in this section show the values for the stirrer speeds of 50 RPM (a), 70 RPM (b), 100 RPM (c) and 120 RPM (d), corresponding to tip speeds $v_{tip,50}$ of 0.59 $\mathrm{m\,s^{-1}}$, 0.82 $\mathrm{m\,s^{-1}}$, 1.18 $\mathrm{m\,s^{-1}}$ and 1.41 $\mathrm{m\,s^{-1}}$ respectively.

The same 2D projection grid is used for the mean velocity and acceleration magnitudes and the probability density function. As such, velocity and acceleration values can be allocated to the respective probability densities.

4.5.1. Arrangement of the 2D projection grid

Each subfigure is divided into interrogation windows over which a mean value is calculated. Every interrogation window has a width of 62 mm and a height of 60 mm. These dimensions are chosen to ensure that the entire evaluated area of the reactor is tiled uniformly. The grid has a height of 13 interrogation windows and a width of 10 interrogation windows for a total number of 130 interrogation windows. Heights registered below 0 mm because of perspective effects are not cut. As such, the lowest reactor interrogation window starts below the X axis at a height of -40 mm.

Figure 4.14 shows the approximate division of the reactor into interrogation windows. The shown figure is only an approximation as, unlike the displayed data, the shown image of the reactor is not corrected for distortion.

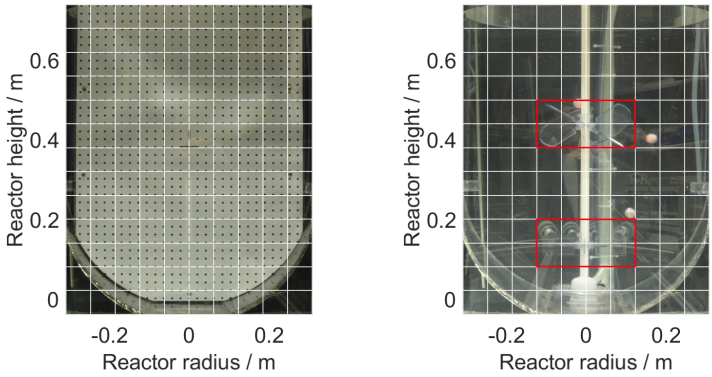

(a) with target (b) with stirrer and motes

Figure 4.14.: Reactor with (a) and without (b) inserted calibration target. The grid is showing an approximation of the interrogation windows. Interrogation windows containing the stirrer blades are marked by a red rectangle.

The color of each interrogation window represents the mean velocity or acceleration magnitude or probability density inside of it as denoted by the colored sidebar. For the mean velocity and acceleration magnitudes, The radius of the contained black circle shows the uncertainty of the measured mean for that interrogation window. A circle touching the interrogation window edges indicates a large uncertainty, a dot indicates a small uncertainty. If no circle is shown, no error could be calculated for the displayed interrogation window. Interrogation windows containing the stirrer blades are marked by a red rectangle.

The very high mean velocity and acceleration magnitudes are adjusted to a maximum color value to reduce the impact of high value, high uncertainty evaluation artifacts. This is done to preserve readability. To facilitate this, for every experiment, the value of the

interrogation windows with the 6th highest (95th percentile) mean velocity or acceleration magnitude is searched. The highest of those values across the set of experiments is selected as the adjustment value. The color scale is adjusted with this value as the maximum. This means values above the adjustment value will be displayed as the adjustment value in the color scale but not higher. The three interrogation windows in the bottom left and right corners are outside of the reactor bounds. These windows show a value of 0 $\mathrm{m\,s^{-1}}$, however the bottom right interrogation window shows the maximum value of the color scale. This is done for technical reasons.

4.5.2. Distribution of mean velocity magnitudes over the 2D projection grid

The following figures show the distribution of mean velocity magnitudes over the 2D projection grid for the sets of experiments performed utilizing the RTPB stirrer setup without aeration (4.15) and an aeration rate of 20 $\mathrm{l \cdot min^{-1}}$ using the micro sparger (4.16). The radius of the black circle corresponds to the uncertainty. A black circle touching the border of the interrogation window corresponds to an uncertainty of 0.03 $\mathrm{m\,s^{-1}}$ or higher.

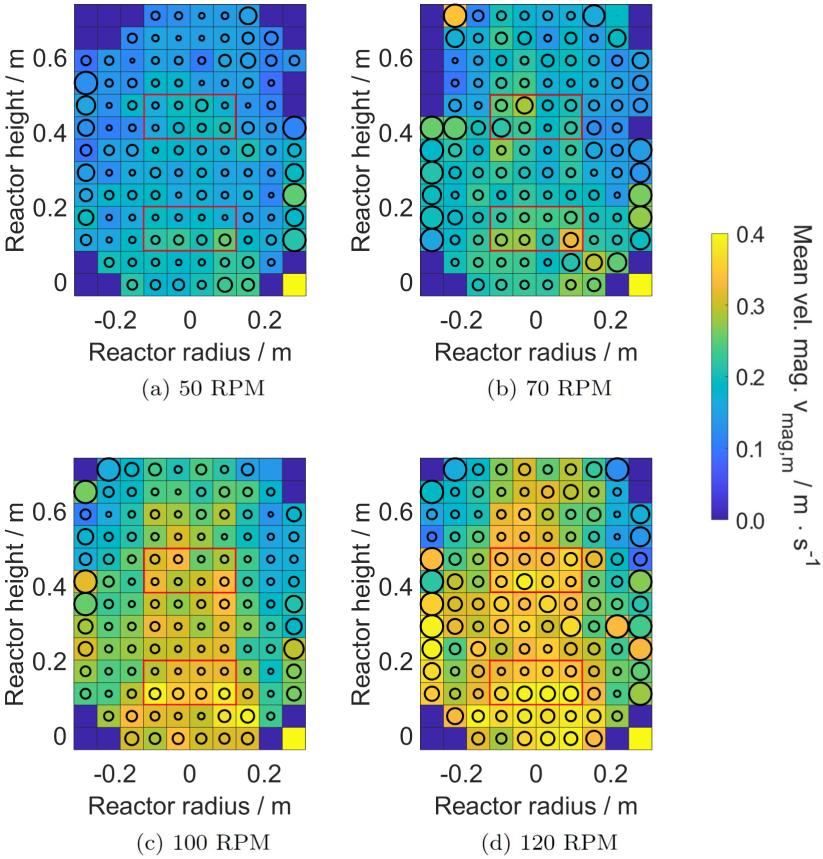

Figure 4.15.: Distributions of velocity magnitudes $v_{mag,m}$ within the reactor utilizing the RTPB setup with no aeration. The color of each interrogation window represents the mean velocity magnitude. The radius of the contained black circle corresponds to the uncertainty of the measured mean up to an uncertainty of 0.03 $\mathrm{m\,s^{-1}}$.

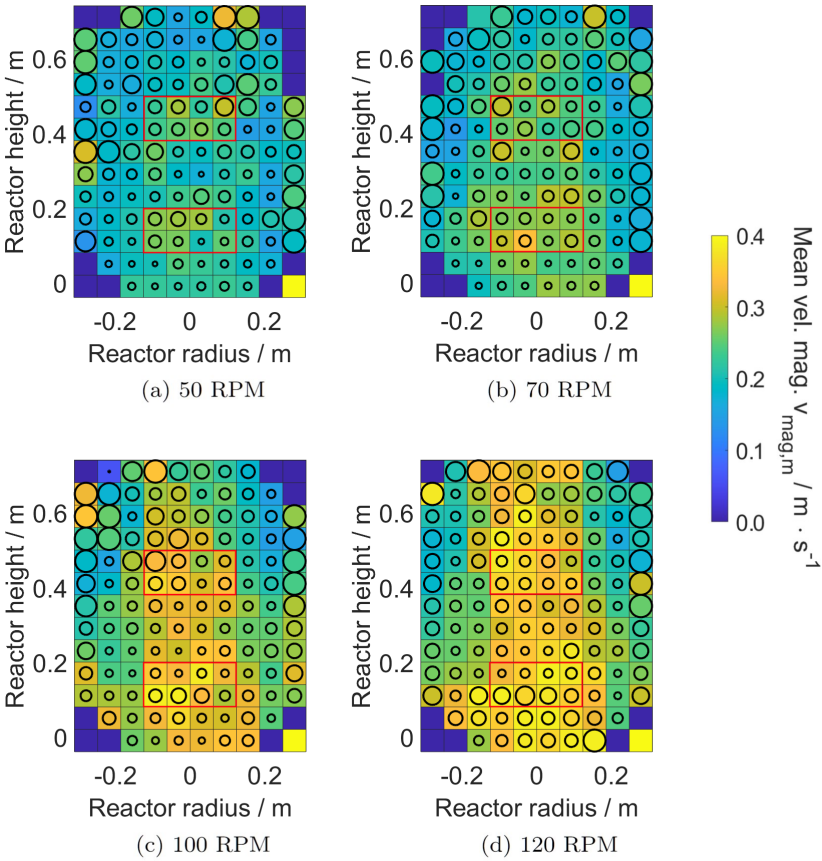

(a) 50 RPM (b) 70 RPM

(c) 100 RPM (d) 120 RPM

Figure 4.16.: Distributions of velocity magnitudes $v_{mag,m}$ within the reactor utilizing the RTPB setup with an aeration rate of 20 $l \cdot min^{-1}$ using the micro sparger. The color of each interrogation window represents the mean velocity magnitude. The radius of the contained black circle corresponds to the uncertainty of the measured mean up to an uncertainty of 0.03 $m\,s^{-1}$.

When plotting the velocity of the LED Motes over the 2D projection grid, the general trend of growing velocities with higher stirrer speeds is shown very clearly for both sets of experiments. Additionally, the two previously observed trends of higher mean velocity magnitudes in the center and bottom of the reactor can once again be observed. When comparing the unaerated and the aerated case it also becomes clear that for the aerated case the velocities at lower stirrer speeds (subfigure 'a') are generally higher relative to the velocities observed for higher stirrer speeds and distributed much more uniformly across the reactor. This effect is likely caused by relatively uniform and random movement of the LED Motes caused by interaction with air bubbles rising upwards through the fluid when aerated and becomes less pronounced with higher stirrer speed as the velocity field becomes increasingly dominated by the rotation of the stirrer. This also suggests that aeration will lead to increased mixing at low stirrer speeds like those employed in bioreactors.

4.5.3. Distribution of mean acceleration magnitudes over the 2D projection grid

The following figures show the distribution of mean acceleration magnitudes through the reactor interrogation windows for the sets of experiments performed utilizing the RTPB stirrer setup without aeration (Figure 4.17) and an aeration rate of 20 $\mathrm{l} \cdot \mathrm{min}^{-1}$ using the micro sparger (Figure 4.18). The radius of the black circle corresponds to the uncertainty. A black circle touching the border of the interrogation window corresponds to an uncertainty of 1 $\mathrm{m\,s}^{-2}$ or higher.

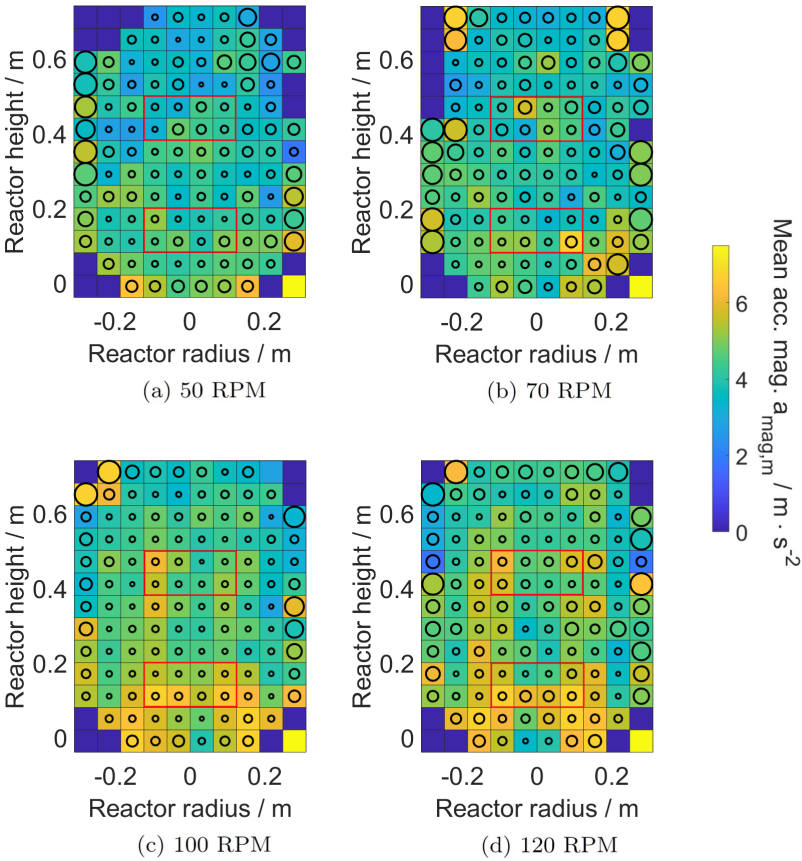

(a) 50 RPM (b) 70 RPM

(c) 100 RPM (d) 120 RPM

Figure 4.17.: Distributions of acceleration magnitudes $a_{mag,m}$ within the reactor utilizing the RTPB setup with no aeration. The color of each interrogation window represents the mean acceleration magnitude. The radius of the contained black circle corresponds to the uncertainty of the measured mean up to an uncertainty of 1 $\mathrm{m\,s^{-2}}$.

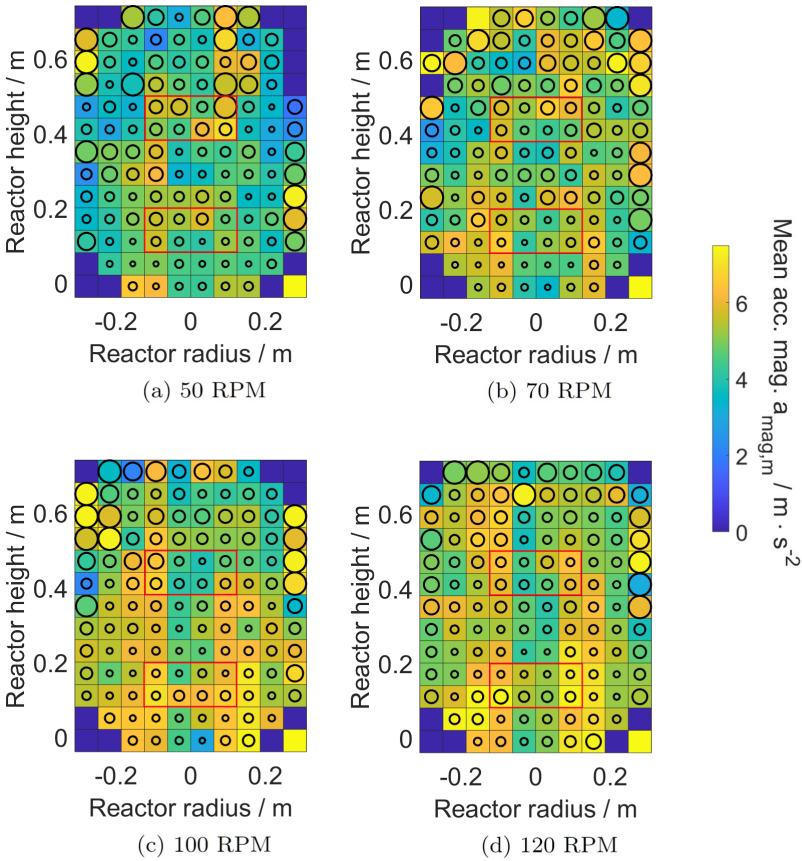

Figure 4.18.: Distributions of acceleration magnitudes $a_{mag,m}$ within the reactor utilizing the RTPB setup with an aeration rate of 20 $l \cdot min^{-1}$ using the micro sparger. The color of each interrogation window represents the mean acceleration magnitude. The radius of the contained black circle corresponds to the uncertainty of the measured mean up to an uncertainty of 1 $m\,s^{-2}$.

Both plots shows the previously observed trend of higher accelerations towards the bottom of the reactor and at a radial position of around -0.1 m and +0.1 m compared to the bulk of the reactor. The visualisation of the distribution of mean acceleration magnitudes across the reactor also affirms the notion of acceleration of the LED Motes caused by rising air bubbles. Especially for low stirrer speeds (Figure 4.18 (a)) relatively high accelerations occur in the upper regions of the reactor outside of the direct vicinity of the stirrer blades. Some of this acceleration could also be caused by LED Motes getting sucked into the stirrer vortex. However vortices are likely not solely responsible for the observed accelerations as their influence would not be expected to diminish in relative strength with rising stirrer speeds.

4.5.4. Probability density distribution over the 2D projection grid

The following figures show the distribution of the likelihood of LED mote occurrence throughout the reactor for the sets of experiments performed utilizing the RTPB stirrer setup without aeration (Figure 4.19) and an aeration rate of 20 $\mathrm{l} \cdot \mathrm{min}^{-1}$ using the micro sparger (Figure 4.20). The value of each interrogation window is calculated by dividing the number of observed LED Motes in that interrogation window through all frames of the recorded video by the total number of observations and the area of the interrogation window. Probabilities of occurrence of more than 6 % are not reflected in the color scale.

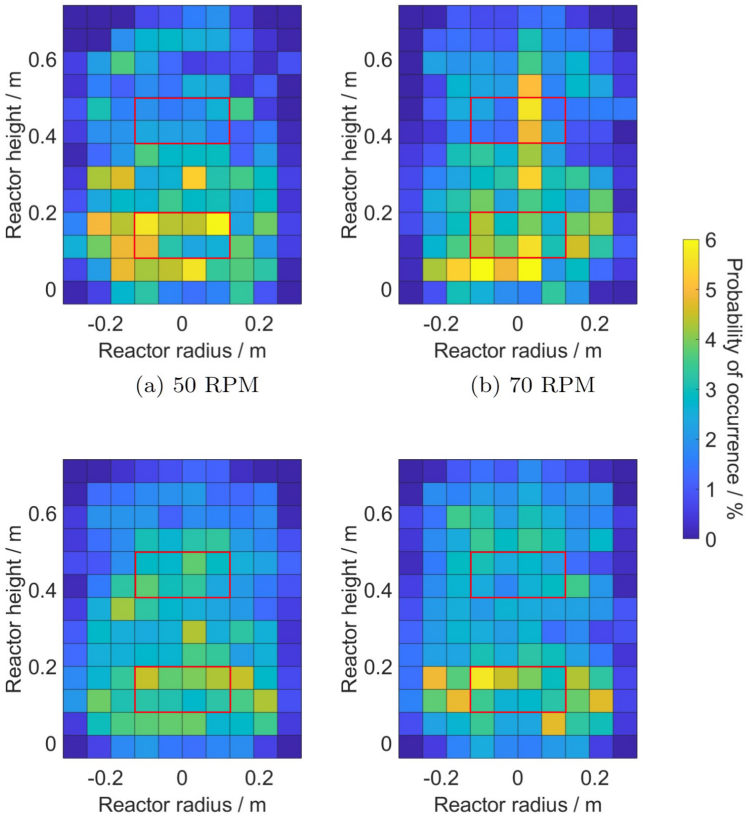

(a) 50 RPM (b) 70 RPM

(c) 100 RPM (d) 120 RPM

Figure 4.19.: Distribution of probability density for the RTPB setup with no aeration. The color of each region represents the likelihood (as a percentage) for an LED Mote to occur within the respective interrogation window.

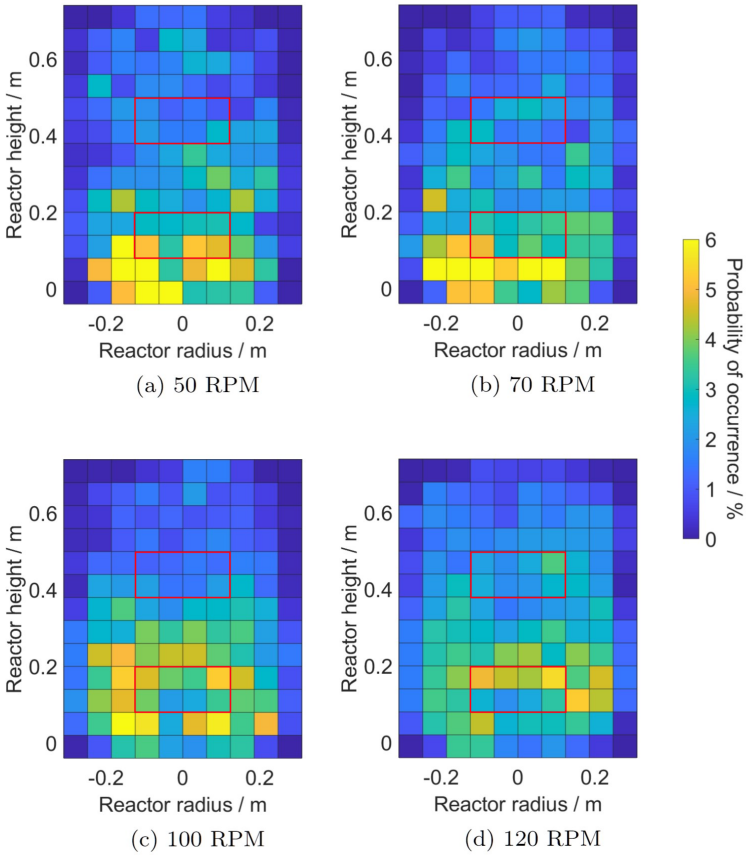

(a) 50 RPM (b) 70 RPM

(c) 100 RPM (d) 120 RPM

Figure 4.20.: Distribution of probability density for the RTPB setup with an aeration rate of 20 $l \cdot min^{-1}$ using the micro sparger. The color of each region represents the likelihood (as a percentage) for an LED Mote to occur within the respective interrogation window.

Plotting the probability density for the positions across the reactor shows a more uniform distribution of recorded LED Mote positions for the unaerated case when compared to the aerated case, especially at lower stirrer speeds. This can be attributed to collisions of the LED Motes with rising air bubbles for the aerated case. As the local mixing density sinks during a collision between an air bubble and an LED Mote, the LED Mote will generally move downwards when colliding with a rising air bubble. The distribution of LED Mote positions is more uniform for higher stirrer speeds for both aeration cases. However, the unaerated case reaches a qualitatively high uniformity at a stirrer speed of 100 RPM (c), at which the aerated case still shows a probability distribution that is strongly skewed towards the bottom. At a stirrer speed of 120 RPM (d) the uniformity of the probability density distributions of the aerated case becomes qualitatively closer to that of the unaerated case. This effect is expected to be observed for any particles sizes. It is unlikely however, that particles with smaller diameters would be affected in the same way, as their interactions with rising air bubbles will lead to different trajectories through the fluid that do not necessarily result in a downward movement. As such, these results should primarily be used when predicting the probability density distribution of similarly sized particles of the same density range.

4.6. Velocity vectors throughout the reactor

Unlike the previous sections that show magnitude values, in this section total values are considered and evaluated. This is why the following figures show the calculated resulting velocity vectors throughout the reactor when plotting mean radial and axial velocities. The length of each vector corresponds to the relative total value of the resulting mean velocity. The direction of the vectors corresponds to the resulting mean direction when combining all observed velocities in the respective interrogation window. As such, resulting relative velocities for the following figures differ from those shown in Section 4.5. Observed velocities pointing in opposite directions cancel each other out and only the resulting velocity is displayed. The vector sizes of the 6 longest vectors (95th percentile) are adjusted to be of an equal size corresponding to the lowest value among those vectors. This is done to increase readability. The length of the red line in the top right of each figure corresponds to a mean total velocity $v_{\mathrm{total,m}}$ of $0.2\ \mathrm{m\,s^{-1}}$. The contours of the stirrer setups are shown (dotted line). Shown are the sets of experiments performed utilizing the RTPB stirrer setup without aeration (Figure 4.21), the PBPB stirrer setup without aeration (Figure 4.22 and the RTPB stirrer setup with an aeration rate of $20\ \mathrm{l \cdot min^{-1}}$ using the micro sparger (Figure 4.23). The stirrer speed is 50 RPM for all figures.

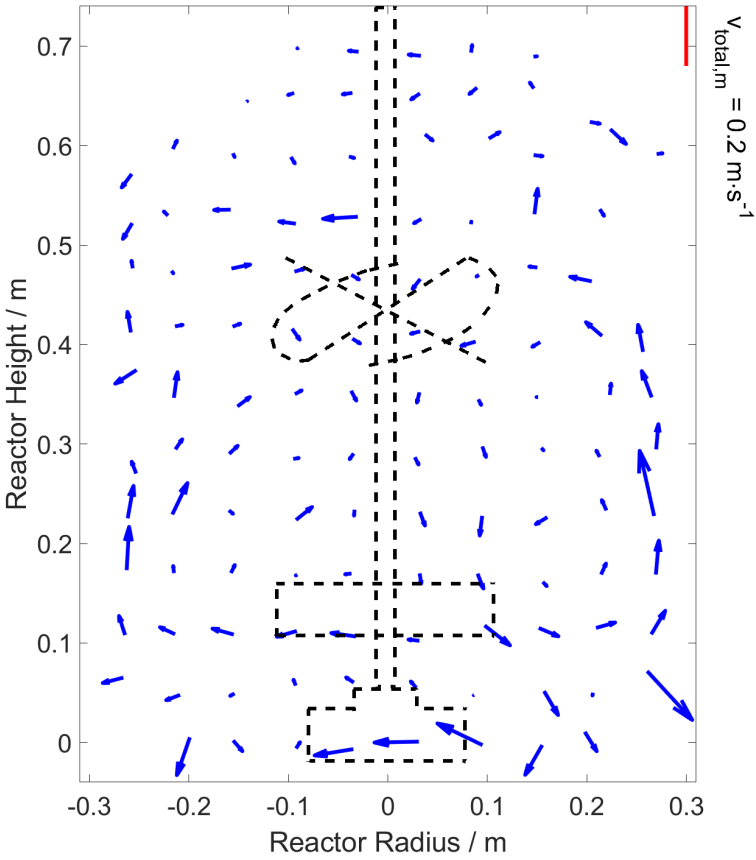

Figure 4.21.: Resulting velocity vectors throughout the reactor when combining mean radial and axial velocities within the respective interrogation window. The experiment is utilizing the RTPB stirrer setup with no aeration at 50 RPM. The length of each vector represents the resulting mean velocity.

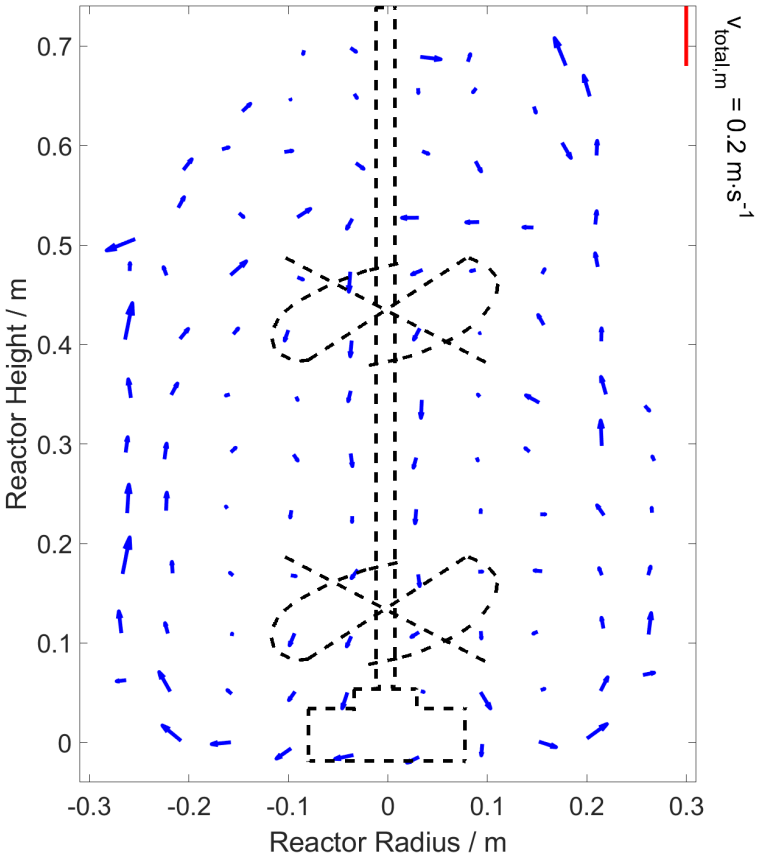

Figure 4.22.: Resulting velocity vectors throughout the reactor when combining mean radial and axial velocities within the respective interrogation window. The experiment is utilizing the PBPB stirrer setup with no aeration at 50 RPM. The length of each vector represents the resulting mean velocity.

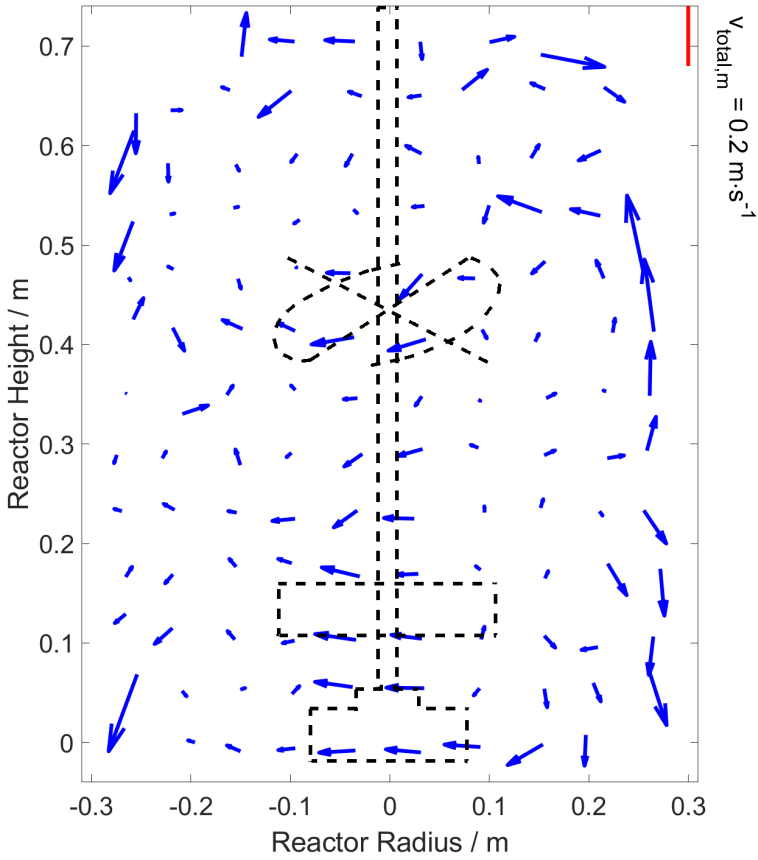

Figure 4.23.: Resulting velocity vectors throughout the reactor when combining mean radial and axial velocities within the respective interrogation window. The experiment is utilizing the RTPB stirrer setup with an aeration rate of 20 $l \cdot min^{-1}$ using the micro sparger at 50 RPM. The length of each vector represents the resulting mean velocity.

For the RTPB setup an expected flow pattern is a predominantly axial flow downwards from the pitched blade impeller into the the Rushton turbine impeller. From the Rushton turbine impeller a radial outwards flow direction is expected. The flow is then expected to be diverted by the reactor wall into an upwards direction. In the upper region of the reactor the flow is expected to to turn inwards and downwards, towards the pitched blade impeller.

In this visualization, for the RTPB stirrer setup and no aeration (Figure 4.21), the LED Motes show a slight preference to downwards movement in the center of the reactor and a strong preference to upwards movement near the reactor walls. Additionally a strong mean radial outwards trajectory at a height of approximately 0.1 m is observed. This corresponds to the location of the Rushton turbine impeller. Another, smaller, radial outwards trend at a height of 0.5 m to 0.6 m and a slight inwards trend at height of 0.3 m to 0.4 m is observed. This observation is likely caused by the formation of a double vortex structure inside of the reactor. A net velocity towards the left at the bottom of the reactor is also observed. A possible reason for this apparent leftwards skew in net velocity are perspective effects described in the error discussion. Another possible cause for this observation is obscuration of LED Motes through the sparger at bottom of the reactor which blocks a considerable area behind. As the stirrer is rotated clockwise, obscuration of LED Motes in the back of the reactor would cause a skewing of resulting mean velocities towards the left. This hypothesis is supported by very slight apparent leftwards net velocities in the center of the reactor (radial position 0 m) over its entire height, where the same effect would be caused by the stirrer shaft and blades.

The velocity vectors for the experiment performed without aeration utilizing the PBPB stirrer setup show a much stronger downwards flow in the center of the reactor and an inwards flow at high vertical positions, suggesting the formation of only a single vortex. This is owed to the form of the stirrers, as the pitched blade stirrer causes higher axial velocities but lower radial velocities when compared to the Rushton turbine impeller.

For the RTPB stirrer setup with an aeration rate of 20 $l \cdot min^{-1}$ using the micro sparger (Figure 4.23) a very strong apparent net velocity towards the left is shown in the center of the reactor. This is likely caused by obscuration of the LED Motes by rising air bubbles. This effect would be most pronounced in the center of the reactor due to the 2D projection of a cylinder. Additionally, due to the poor dispersion of gas bubbles at low stirrer speeds, most air bubbles are rising at low radial positions, leading to higher degrees of light extinction. While similar patterns as those observed in the unaerated cases are visible, the skewing of the resulting velocities is likely substantial and directional data for the the velocities from this evaluation method should be treated with caution.

4.7. Error discussion

In this section sources of error stemming from the experimental setup, the recording process, the image processing and the additional data processing steps are discussed. One source of error is the variance in the density of the LED Motes. As the densities are not uniform and fall into a range of 1000 $kg \cdot m^{-3}$ to 1003 $kg \cdot m^{-3}$, each employed LED Motes will have a different flow following and sinking behavior (as shown in Figures 4.1 and 4.2).However, as shown in Figure 4.1, the influence of variance in mote density on the Stokes Number is small relative to the total Stokes Number for the specified density range. Another source of error is introduced by the perspective of the camera. As the camera is a finite distance (2.2 m) away from the reactor, the projection of the 3D space inside of the reactor is distorted, such that a particle below the camera will appear to move downwards when moving towards the camera and upwards when moving away from the camera. This introduces errors in the positional, as well as velocity and acceleration data.

During data processing another source of error is the misidentification of LED Mote positions through the employed MATLAB script. As the LED Motes are not uniformly lit, but instead contain two

LEDs to provide illumination, it is possible that a change in rotation could lead to a change in registered position. Measures are taken to minimize the impact of this occurrence by clustering of recognized LED Mote positions. Though, it is unlikely that this effect is fully compensated for.

One more source of error is the false recognition of LED Mote reflections on the reactor walls as real LED Motes. Measures are taken to avoid false detection, such as setting a minimal brightness threshold for LED Mote recognition and setting a minimum length of tracks to be considered as valid data. Despite this false detection of reflections of LED Motes as real LED Motes are likely the cause of many of the apparent very high velocity and acceleration tracks at the edges of the surveyed area at radial positions of -0.3 m and +0.3 m. As LED Mote positions belonging to tracks of a length less than 5 are not considered for the calculation of velocity and acceleration values, uncertainties are expected to increase due to a smaller number of data points. This effect is stronger for the aerated case, where the length of tracks is generally reduced and more tracks fall below the length threshold (see Appendix D).

Inaccuracies in the calibration are also a source of error. Firstly, a possible misidentified calibration dot position might skew all calculated positions for motes in a 40 mm by 40 mm square around it (see Figure 3.9). However this type of error is minimized by manual confirmation of correct calibration dot detection. Likely a bigger cause of error is the extrapolation of LED Mote positions towards the left and right edges of the reactor, since the calibration target is slightly smaller than the inside of the reactor. The distortion increases towards the sides of the camera's field of view despite the outer reactor container. One more possible source of error in the calibration is the interpolation between calibration dots. As positions are only known directly at the dots, any registered LED Mote position that is not directly at a calibration dot is linearly interpolated between the four closest calibration dots. However, the error to the position introduced by this is small as the maximum distance a LED Mote can have to a calibration dot position while inside the area

covered by the target is only 10 mm.

A possible error introduced through the tracking script is the erroneous connection or cross-linking of two LED Mote trajectories into one, possibly leading to high apparent accelerations. Moreover, the splitting of a single LED Mote's trajectory into two or more tracks can lead to a loss of velocity and acceleration data. This might happen when the mote is accelerated fast enough, so that the new LED Mote position is outside the search radius of the previous track. This means there might be an under-estimation of high LED Mote accelerations. Another possible reason for a cut in a LED Mote track is obscuration induced by the stirrer blade, other reactor internals or air bubbles. This blocking of LED Motes from view likely caused a strong skewing in detected velocity direction for the velocity vectors in the aerated case and thus results from these cases should be treated with caution. Additionally, many of the mentioned sources of error are compounded by the low selected recording time, leading to larger errors, especially towards top and sides of the reactor where the frequency of detection was lower than in the reactor center.

5. Conclusion and Outlook

A custom made, robust MATLAB algorithm with calibration, image preprocessing, image recognition and LED Mote position detection was developed. Existing algorithms for calculating velocities and accelerations based on position data were adjusted. The goal of tracking the 2D positions of LED Motes throughout a 200 L acrylic glass STR has been achieved. Calculations of the Stokes and Archimedes Number show that the employed particles are not perfectly flow-following and thus do not capture vortices at micro-scale. Nonetheless, the major flow phenomena inside of the reactor were captured in a satisfying resolution with regards to the implementation of Lagrangian Sensor Particles. A preference of higher mean velocity and acceleration magnitudes when utilizing the Rushton turbine and pitched blade impeller setup compared to the double pitched blade impeller setup is observed. A trend in mean velocity and acceleration magnitudes was not observed between aeration rates and only to a small degree between the unaerated case and the aerated cases (Section 4.3).

Mean velocity magnitudes inside of the reactor were shown to be generally higher towards the center of the reactor and decreasing with higher vertical positions. Peaks in mean velocity and acceleration magnitudes at a radial position of -0.1 m and +0.1 m were observed (Section 4.4). This is likely caused by the blades of the stirrers whose tip is at a radial distance of 0.1 m from the reactor center. When employing the RTPB setup, a stronger correlation between stirrer speed and LED Mote velocity is observed, especially in the center of the reactor. As such, a greater difference in mean velocity magnitudes between the stirrer setups is observed, especially for higher stirrer speeds.

Examination of the velocity and Distribution of mean acceleration

magnitudess (Section 4.5.2 and 4.5.3) show that aeration leads to a relative increase in velocity and acceleration at lower stirrer speeds compared to higher stirrer speeds, likely due to interactions of LED Motes with rising air bubbles. This effect is especially pronounced in the center of the reactor between -0.1 m and +0.1 m of radial position, as the rising air bubbles are concentrated in that region for low stirrer speeds.

The probability distributions for LED Mote positions throughout the reactor (Section 4.5.4) show a generally more uniform distribution for the unaerated case, with LED Mote locations in the aerated case tending more towards the reactor bottom. This too is caused by interactions between the LED Motes and rising air bubbles in the reactor center. Therefore in order to receive a satisfactory distribution over the entire reactor region, three options are available. Firstly, a higher stirrer speed can be adjusted to counteract this effect. However, high stirrer speeds reduce the yields in many of the most common fermentation processes, for example those involving CHO cells. As such, this option is unlikely to be an adequate solution. Secondly, a more widespread sparger can be installed. This would require a higher gas pressure and would lead to higher pressure drops. Thirdly, baffles can be implemented. By doing so, the predominant tangential flow gives way to a more axial flow.

In general, longer recording times for the experiments would have likely yielded more uniform data and lower errors, especially towards the top and sides of the reactor where the data density of the LED Motes was relatively low compared to the center.

The flow vector diagrams (Section 4.5.2) show the formation of a double vortex flow for the RTPB stirrer setup and the formation of a single vortex flow for the double pitched blade impeller setup without aeration. For the aerated case, a strong apparent net velocity to the left was observed in the center of the reactor. This is caused by LED Motes being obscured by air bubbles.

To address these challenges and gain additional insights, future experiments using this work as a basis are planned. The implementation of 3D-tracking will remove uncertainties caused by perspective

effects and different LED configurations with higher visibility will allow for more reliable tracking of LED Mote trajectories in the 200 L acrylic glass STR as well as a 2000 L and 15000 L acrylic glass STR when utilizing aeration. Color coding of LED Motes will allow for uninterrupted tracks to be created, removing the possibility of wrongly connected or cut trajectory tracks. Additionally, to attain the ability to measure LSP trajectories in reactor setups without visual access, the scripts developed in this work will be used to validate and improve measurements taken with LSP containing an inertial measurement units and a pressure sensor.

Bibliography

[Rei16] S. Reinecke, U. Hampel, *Instrumented flow-following sensor particles with magnetic position detection and buoyancy control*, Journal of Sensors and Sensor Systems (2016). doi:10.5194/jsss-5-213-2016

[Bun20] L. Buntkiel, S. Reinecke, U. Hampel, *Towards 3D-Motion Tracking of Instrumented Flow - Followers in Large Vessels*, Sensor and Measurement Science (2020). doi:10.5162/SMSI2020/E6.1

[Lau19] T. Lauterbach, N. Ziebart, T. Bley, T. Walther, F. Lenk, *Mobile Sensoren für die Biotechnologie Ortsunabhängige, miniaturisierte Prozessmessung*, Chemie Ingenieur Technik 91 (2019). doi:10.1002/cite.201900114

[Wer97] F. C. Werner, *Ueber die Turbulenz in geruehrten newtonschen und nicht-newtonschen Fluiden*, Herbert Utz Verlag, Lehrstuhl B fur Verfahrenstechnik der Technischen Universitat Munchen, 1997

[Zlo01] M. Zlokarnik, *Stirring Theory and Practice*, Wiley-VCH Verlag GmbH, 2001, ISBN 3-527-29996-3

[Cro12] C. T. Crowe, J. D. Schwarzkopf, M. Sommerfeld, Y. Tsuji, *Multiphase Flows with Droplets and Particles 2nd Edition*, CRC Press (2012), isbn:978-1-4398-4051-1

[Rei12] S. Reinecke, A. Deutschmann, K.Jobst, H.Kryk, E.Friedrich, U.Hampel, *Flow following sensor particles—Validation and macro-mixing analysis in a stirred fermentation vessel with a highly viscous substrate*, Biochemical Engineering Journal 69 (2012). doi:10.1016/j.bej.2012.09.010

[Hai89] A. Haider, O. Levenspiel, *Drag Coefficient and Terminal Velocity of Spherical and Nonspherical Particles*, Powder Technology 58 (1989). doi:10.1016/0032-5910(89)80008-7

[Hai20] Haim Kalman, *Role of Reynolds and Archimedes Numbers in particle-fluid flows*, Reviews in Chemical Engineering (20020). doi:10.1515/revce-2020-0005

[Lau19] T. Lauterbach, T. Lüke, M Büker, H. Hedayat, T. Gernandt, R. Moll, M. Grösel, S. Lenk, F. Seidel, D. Brunner, T. Bley, T. Walther, F. Lenk, *Measurements on the fly– Introducing mobile micro-sensors for biotechnological applications*, Sensors and Actuators A 287 (2019). doi:10.1016/j.sna.2019.01.003

[Zim13a] R. Zimmermann, L. Fiabane, Y. Gasteuil, R. Volk, J-F. Pinton, *Measuring Lagrangian accelerations using an instrumented particle*, Physica Scripta T155 (2013). doi:10.1088/0031-8949/2013/T155/014063

[Zim13b] R. Zimmermann, L. Fiabane, Y. Gasteuil, R. Volk, J. Pinton, *Characterizing flows with an instrumented particle measuring Lagrangian accelerations*, New Journal of Physics 15 (2013). doi:10.1088/1367-2630/15/1/015018

[Bis20] J. Bisgaard, M. Muldbak, S. Cornelissen, T. Tajsoleiman, J. Huusom, T. Rasmussen, K. Gernaey, *Flow-following sensor devices: A tool for bridging data and model predictions in large-scale fermentations*, Computational and Structural Biotechnology Journal 18 (2020). doi:10.1016/j.csbj.2020.10.004

[Bis21a] J. Bisgaard, T. Tajsoleiman, M. Muldbak, T. Rydal, T. Rasmussen, J. Huusom, K. Gernaey, *Automated Compartment Model Development Based on Data from Flow-Following Sensor Devices*, Processes 9 (2021). doi:10.3390/pr9091651

[Bis21b] J. Bisgaard, M. Muldbak, T. Tajsoleiman, T. Rydal, T. Rasmussen, J. Huusom, K. Gernaey, *Characterization of mixing performance in bioreactors using flow-following sensor devices*, Chemical Engineering Research and Design 174 (2021). doi:10.1016/j.cherd.2021.08.008

[Sti20] J. Stine, L. Beardslee, R. Sathyam, W. Bentley, R. Ghodssi, *Electrochemical Dissolved Oxygen Sensor-Intergrated Platform for Wireless In Situ Bioprocess Monitoring*, Sensors & Actuators: B. Chemical 320 (2020). doi:10.1016/j.snb.2020.128381

[Sti19] J. Stine, *BPOD: A wireless integrated sensor platform for continuous localized bioprocess monitoring*, 2019

[Ste15] R. Stewart, I. Sutalo, C. Wong, *Three-dimensional tracking of sensor capsules mobilised by fluid flow*, Measurement Science and Technology 26 (2015)

[Wan16] S. Wang, R. Stewart, G. Metcalfe, *Visualization of the trapping of inertial particles in a laminar mixing tank*, Chemical Engineering Science 143 (2016). doi:/10.1016/j.ces.2015.12.023

[Gla10] J. Glazyrina, E. Materne, T. Dreher, D. Storm, S Junne, T. Adams, G. Greller, P. Neubauer,*Research High cell density cultivation and recombinant protein production with Escherichia coli in a rocking-motion-type bioreactor*, Glazyrina et al. Microbial Cell Factories 9 (2010)

[Oue08] N, Ouellette, P. Malley, J. Gollub, *Transport of Finite-Sized Particles in Chaotic Flow*, Physical Review Letters (2008) 101

[Oue06] N. Ouellette, H. Xu, E. Bodenschatz, *A quantitative study of three-dimensional Lagrangian particle tracking algorithms*, Experiments in Fluids (2006) 40: 301–313. doi:10.1007/s00348-005-0068-7

[Wil91] C. Willert, M. Gharib, *Digital particle image velocimetry*, Experiments in Fluids 10, 181-193 (1991)

[Wil14] D. Wilde, T. Dreher, C. Zahnow, U. Husemann, G. Greller, T. Adams, C. Fenge, *Superior Scalability of Single-Use Bioreactors*, BioProcess International September 2014

[Eib18] R. Eibl, V. JossEn, D. EiBl, *Therapeutische Antikörper Einweg-Bioreaktoren*, Chemie In Unserer Zeit 52 (2018). doi:10.1002/ciuz.201800803

[Löf13] C. Löffelholz, U. Husemann, G. Greller, W. Meusel, J. Kauling, P. Ay, M. Kraume, R. Eibl, D. Eibl,*Bioengineering Parameters for Single-Use Bioreactors: Overview and Evaluation of Suitable Methods*,Chemie Ingenieur Technik 85 (2013)

[Eib19] R. Eibl, D. Eibl, *Single-Use Technology in Biopharmaceutical Manufacture*, Wiley & Sons, Inc. (2019) ISBN 9781119477785

[Eib10] R. Eibl, S. Kaiser, R. Lombriser, D. Eibl,*Disposable bioreactors: the current state-of-the-art and recommended applications in biotechnology*, Appl Microbiol Biotechnol 86 (2010). doi:10.1007/s00253-009-2422-9

[Löf14] C. Löffelholz, S. Kaiser, M. Kraume, R. Eibl, D. Eibl, *Dynamic Single-Use Bioreactors Used in Modern Liter- and m3- Scale Biotechnological Processes: Engineering Characteristics and Scaling Up*, Adv Biochem Eng Biotechnol 138 (2014). doi:10.1007/10/2013/187

[Mer98] A. Mersmann, F. Werner, S. Maurer, K. Bartosch, *Theoretical prediction of the minimum stirrer speed in mechanically agitated suspensions*, Chemical Engineering and Processing: Process Intensification 37 (1998). doi:10.1016/S0255-2701(98)00057-9.

[Rub21] D. Rubenstein, W. Yin, M. Frame, *Biofluid Mechanics - An Introduction to Fluid Mechanics, Macrocirculation, and Microcirculation*, Academic Press (2021). ISBN 978-0-12-818034-1 doi:10.1016/C2018-0-02144-1

A. Parameter Sets At Varying Stirrer Speeds

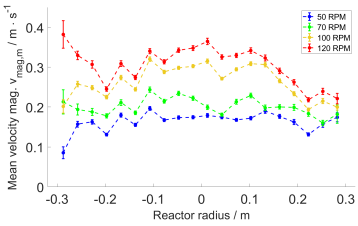

(a) Velocity over reactor width

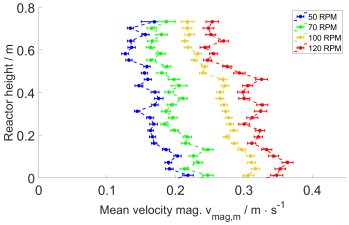

(b) Velocity over reactor height

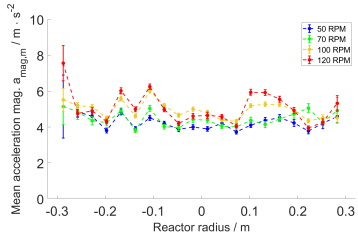

(c) Acceleration over reactor width

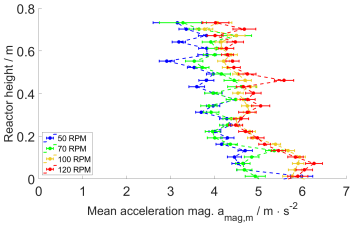

(d) Acceleration over reactor height

Figure A.1.: Line plot of calculated mean velocity and acceleration magnitudes over reactor width and height for the Rushton turbine and pitched blade impeller (RTPB) setup with no aeration.

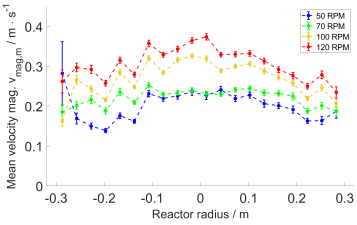

(a) Velocity over reactor width

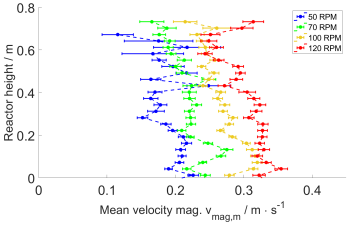

(b) Velocity over reactor height

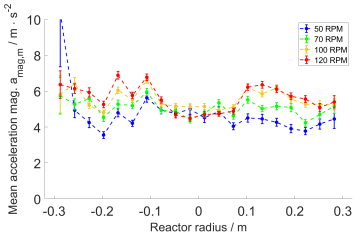

(c) Acceleration over reactor width

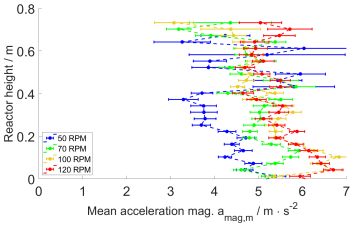

(d) Acceleration over reactor height

Figure A.2.: Line plot of calculated mean velocity and acceleration magnitudes over reactor width and height for the Rushton turbine and pitched blade impeller (RTPB) setup and an aeration rate of 15 l · min^{-1} utilizing the macro sparger.

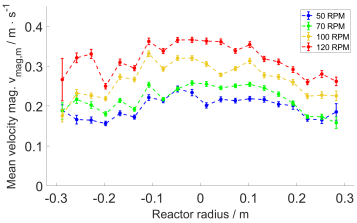

(a) Velocity over reactor width

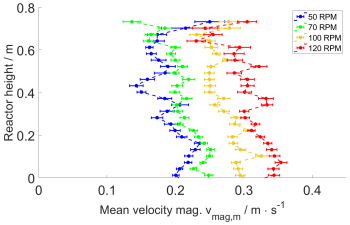

(b) Velocity over reactor height

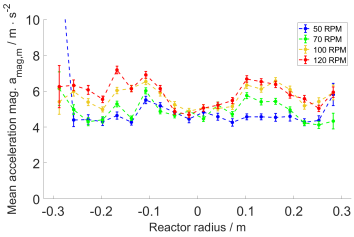

(c) Acceleration over reactor width

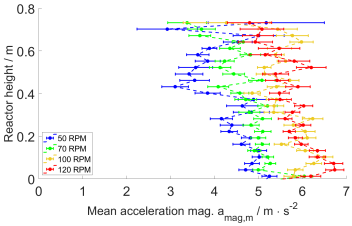

(d) Acceleration over reactor height

Figure A.3.: Line plot of calculated mean velocity and acceleration magnitudes over reactor width and height for the Rushton turbine and pitched blade impeller (RTPB) setup and an aeration rate of 20 l · min^{-1} utilizing the macro sparger.

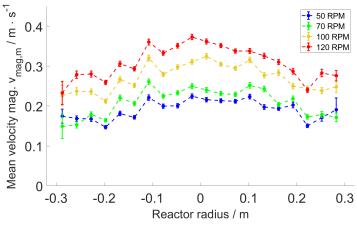

(a) Velocity over reactor width

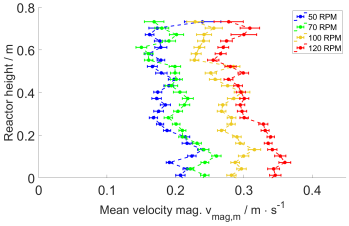

(b) Velocity over reactor height

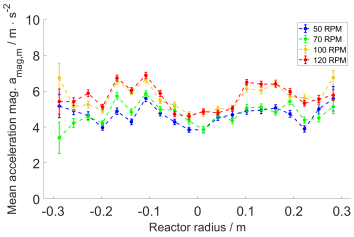

(c) Acceleration over reactor width

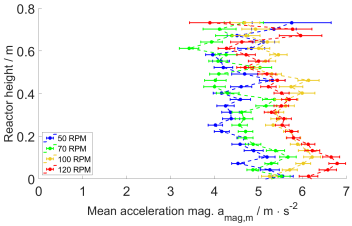

(d) Acceleration over reactor height

Figure A.4.: Line plot of calculated mean velocity and acceleration magnitudes over reactor width and height for the Rushton turbine and pitched blade impeller (RTPB) setup and an aeration rate of 15 l · min^{-1} utilizing the micro sparger.

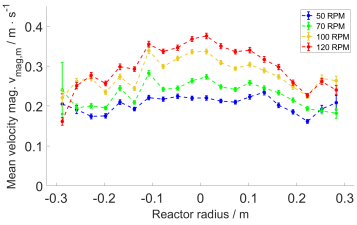

(a) Velocity over reactor width

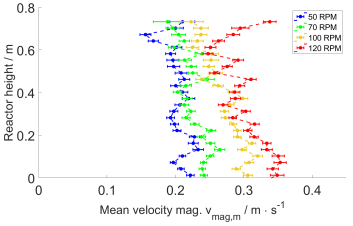

(b) Velocity over reactor height

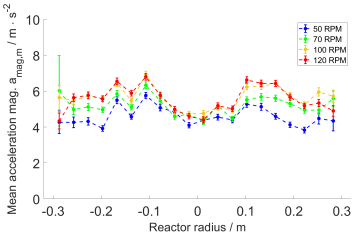

(c) Acceleration over reactor width

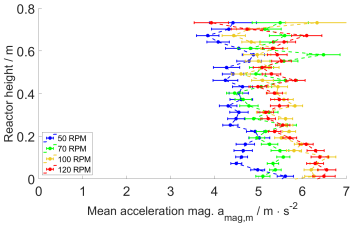

(d) Acceleration over reactor height

Figure A.5.: Line plot of calculated mean velocity and acceleration magnitudes over reactor width and height for the Rushton turbine and pitched blade impeller (RTPB) setup and an aeration rate of 20 l · min^{-1} utilizing the micro sparger.

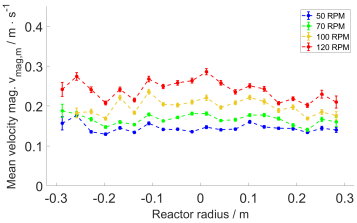

(a) Velocity over reactor width

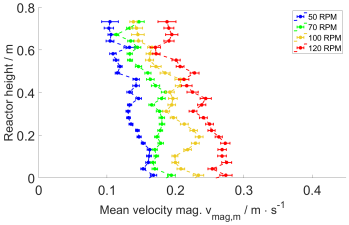

(b) Velocity over reactor height

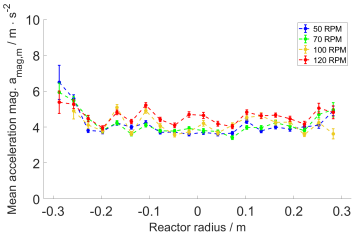

(c) Acceleration over reactor width

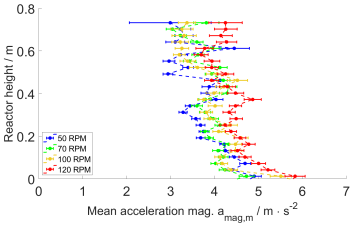

(d) Acceleration over reactor height

Figure A.6.: Line plot of calculated mean velocity and acceleration magnitudes over reactor width and height for the double pitched blade impeller (PBPB) setup with no aeration.

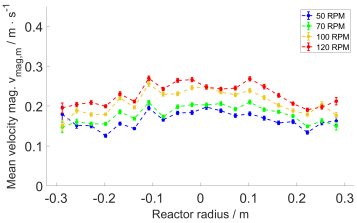

(a) Velocity over reactor width

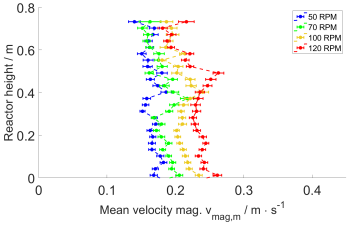

(b) Velocity over reactor height

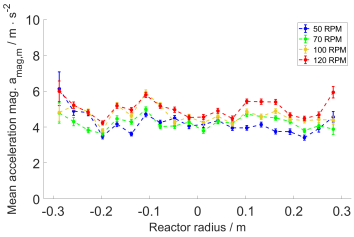

(c) Acceleration over reactor width

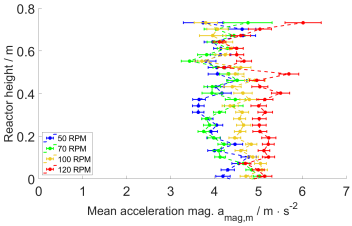

(d) Acceleration over reactor height

Figure A.7.: Line plot of calculated mean velocity and acceleration magnitudes over reactor width and height for the double pitched blade impeller (PBPB) setup and an aeration rate of 15 l · min^{-1} utilizing the macro sparger.

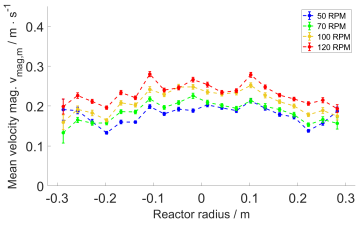

(a) Velocity over reactor width

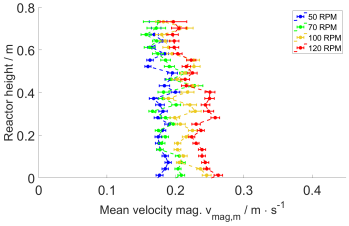

(b) Velocity over reactor height

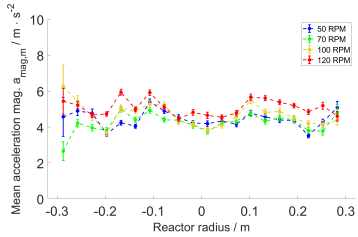

(c) Acceleration over reactor width

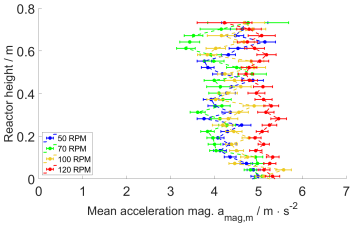

(d) Acceleration over reactor height

Figure A.8.: Line plot of calculated mean velocity and acceleration magnitudes over reactor width and height for the double pitched blade impeller (PBPB) setup and an aeration rate of 20 l · min^{-1} utilizing the macro sparger.

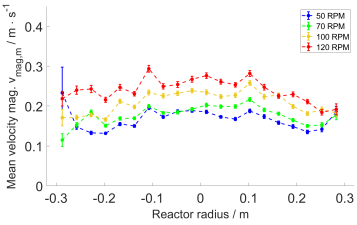

(a) Velocity over reactor width

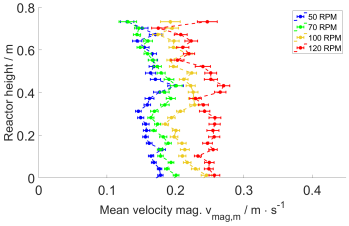

(b) Velocity over reactor height

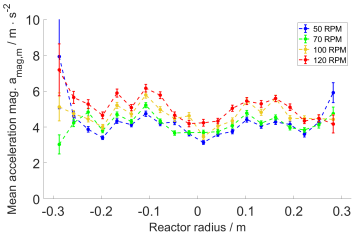

(c) Acceleration over reactor width

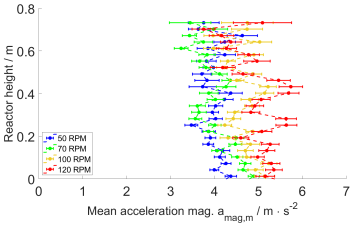

(d) Acceleration over reactor height

Figure A.9.: Line plot of calculated mean velocity and acceleration magnitudes over reactor width and height for the double pitched blade impeller (PBPB) setup and an aeration rate of 15 l · min^{-1} utilizing the micro sparger.

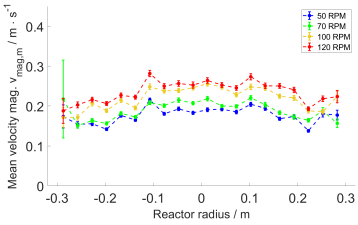

(a) Velocity over reactor width

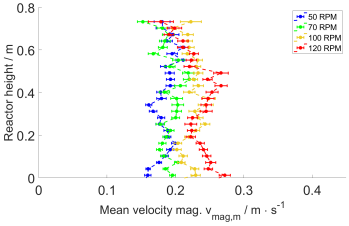

(b) Velocity over reactor height

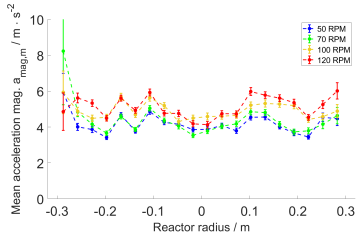

(c) Acceleration over reactor width

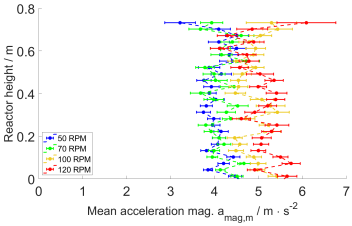

(d) Acceleration over reactor height

Figure A.10.: Line plot of calculated mean velocity and acceleration magnitudes over reactor width and height for the double pitched blade impeller (PBPB) setup and an aeration rate of 20 l · min^{-1} utilizing the micro sparger.

B. Evaluation Of Results In A 2D Projection Grid

B.1. Mean velocity magnitudes over the 2D grid

Distributions of mean velocity magnitudes within the reactor displayed in $\mathrm{mm\,s^{-1}}$ for 50, 70, 100 and 120 RPM. The color of each region represents the mean velocity magnitude inside of it. The use of $\mathrm{mm\,s^{-1}}$ instead of $\mathrm{m\,s^{-1}}$ is done for technical reasons. The radius of the black circle corresponds to the uncertainty. A black circle touching the border of the interrogation window corresponds to an uncertainty of 30 $\mathrm{mm\,s^{-1}}$ or higher.

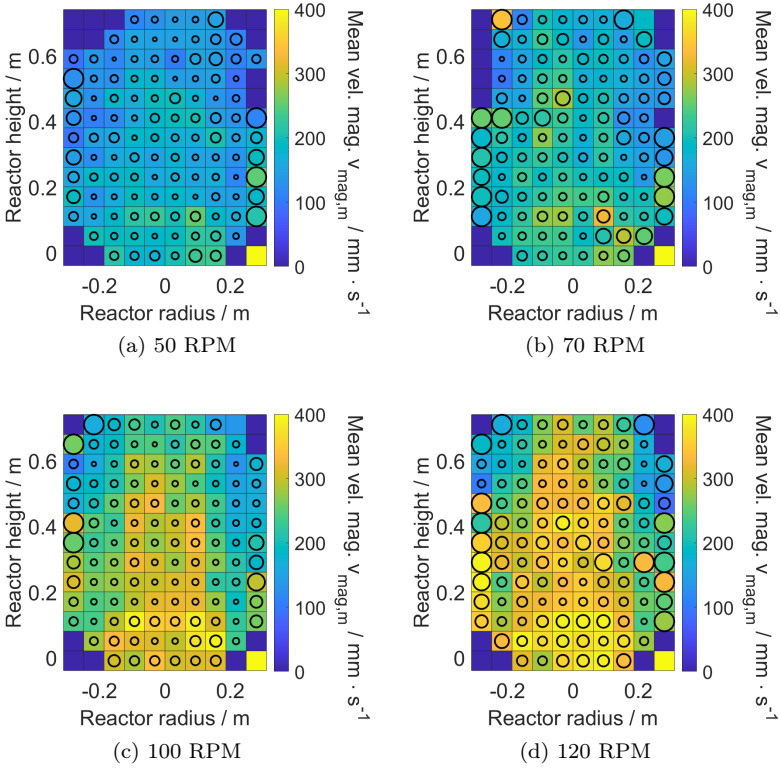

(a) 50 RPM (b) 70 RPM

(c) 100 RPM (d) 120 RPM

Figure B.1.: Distribution of mean velocity magnitudes for the experiment conducted using the Rushton turbine and pitched blade impeller (RTPB) setup with no aeration.

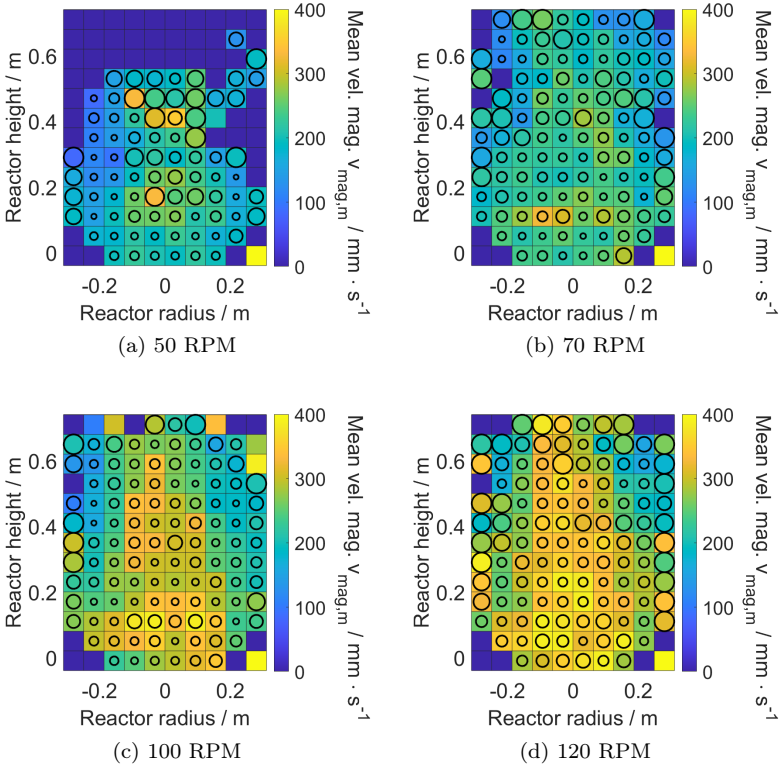

(a) 50 RPM (b) 70 RPM

(c) 100 RPM (d) 120 RPM

Figure B.2.: Distribution of mean velocity magnitudes for the experiment conducted using the Rushton turbine and pitched blade impeller (RTPB) setup and an aeration rate of 15 l · min^{-1} utilizing the macro sparger.

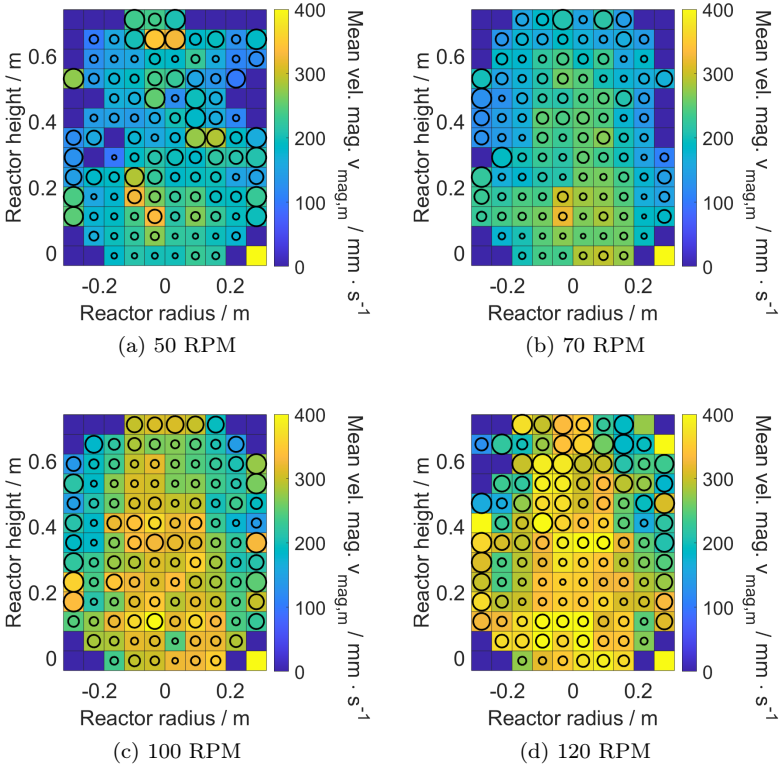

(a) 50 RPM (b) 70 RPM

(c) 100 RPM (d) 120 RPM

Figure B.3.: Distribution of mean velocity magnitudes for the experiment conducted using the Rushton turbine and pitched blade impeller (RTPB) setup and an aeration rate of 20 l · min^{-1} utilizing the macro sparger.

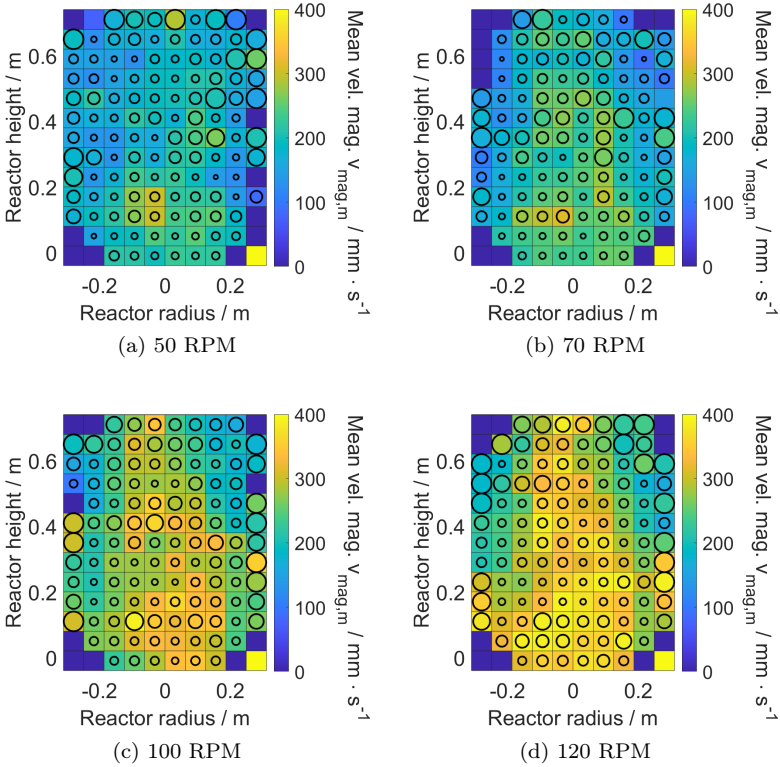

(a) 50 RPM (b) 70 RPM

(c) 100 RPM (d) 120 RPM

Figure B.4.: Distribution of mean velocity magnitudes for the experiment conducted using the Rushton turbine and pitched blade impeller (RTPB) setup and an aeration rate of 15 l · min^{-1} utilizing the micro sparger.

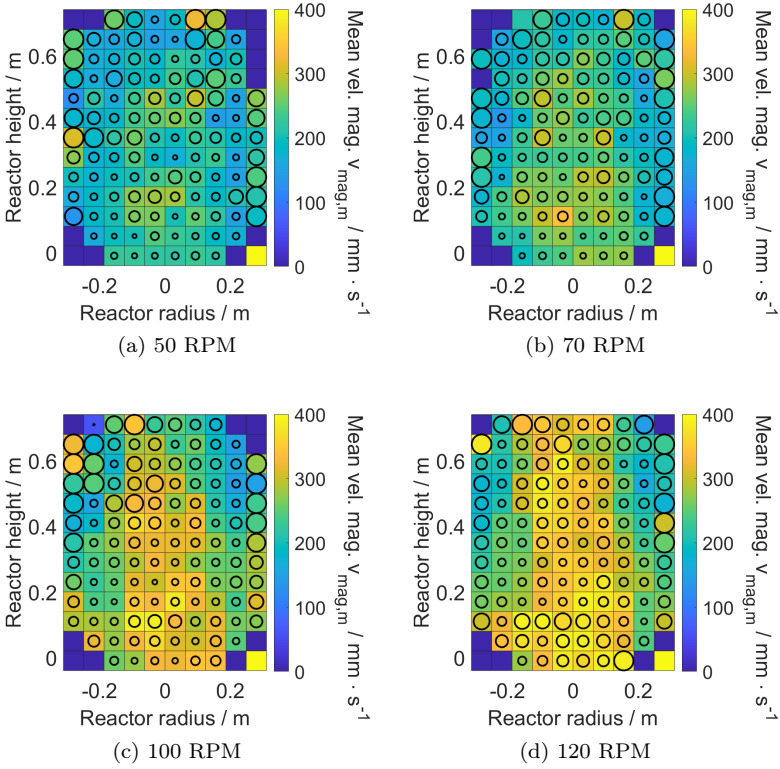

(a) 50 RPM (b) 70 RPM

(c) 100 RPM (d) 120 RPM

Figure B.5.: Distribution of mean velocity magnitudes for the experiment conducted using the Rushton turbine and pitched blade impeller (RTPB) setup and an aeration rate of 20 l · min^{-1} utilizing the micro sparger.

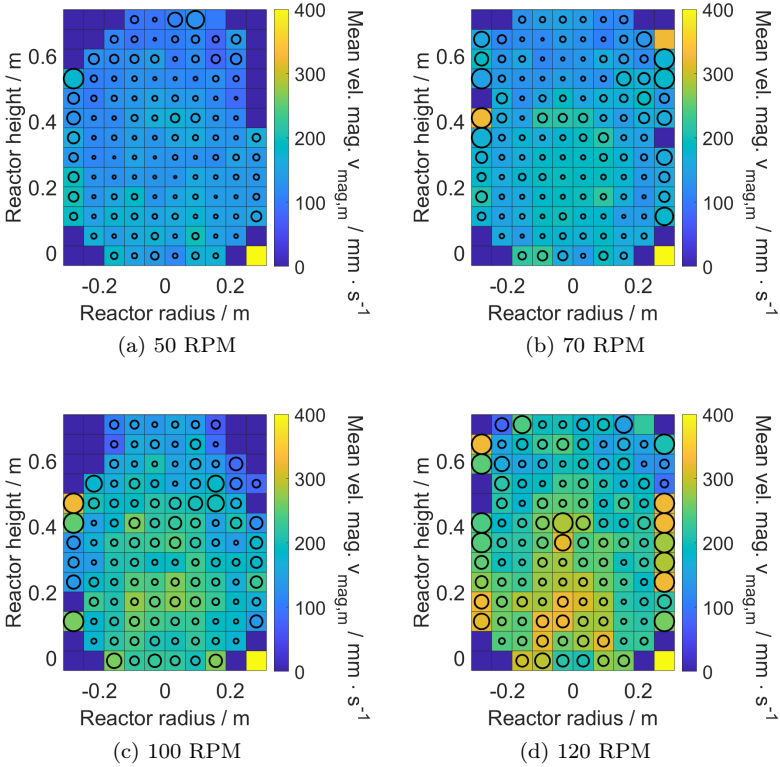

(a) 50 RPM (b) 70 RPM

(c) 100 RPM (d) 120 RPM

Figure B.6.: Distribution of mean velocity magnitudes for the experiment conducted using the double pitched blade impeller (PBPB) setup with no aeration.

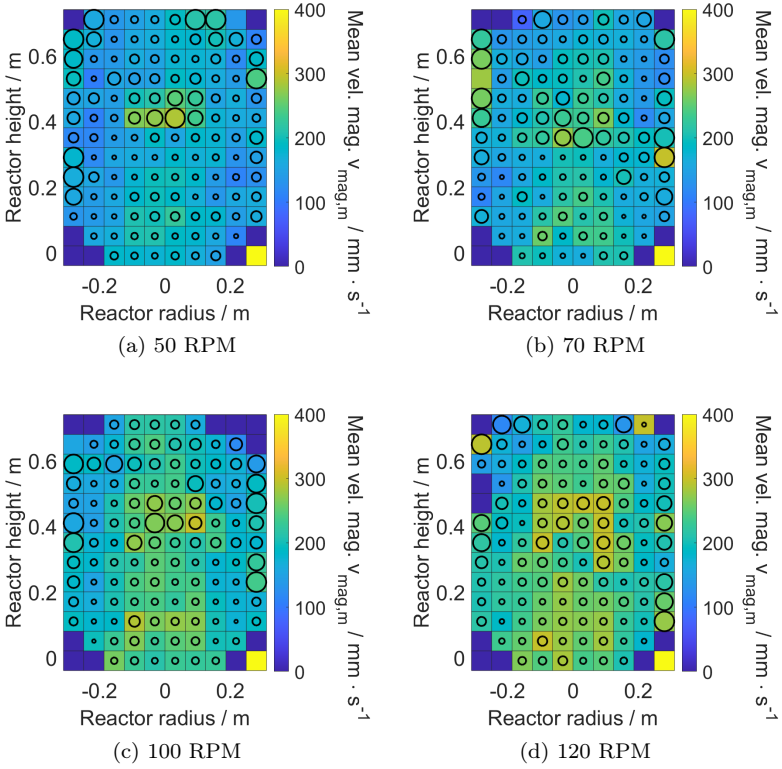

(a) 50 RPM (b) 70 RPM

(c) 100 RPM (d) 120 RPM

Figure B.7.: Distribution of mean velocity magnitudes for the experiment conducted using the double pitched blade impeller (PBPB) setup and an aeration rate of 15 l · min^{-1} utilizing the macro sparger.

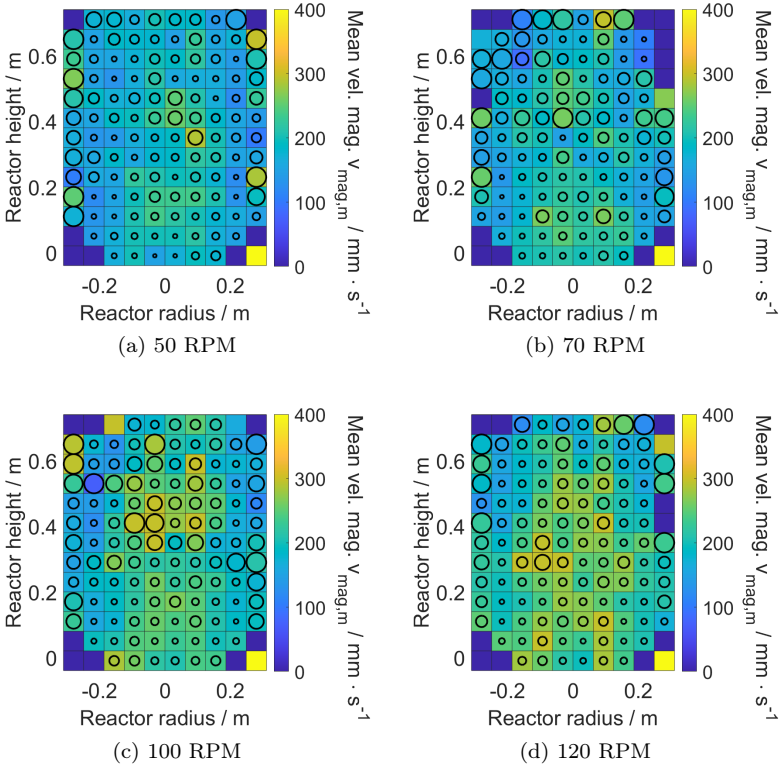

(a) 50 RPM (b) 70 RPM

(c) 100 RPM (d) 120 RPM

Figure B.8.: Distribution of mean velocity magnitudes for the experiment conducted using the double pitched blade impeller (PBPB) setup and an aeration rate of 20 l · min^{-1} utilizing the macro sparger.

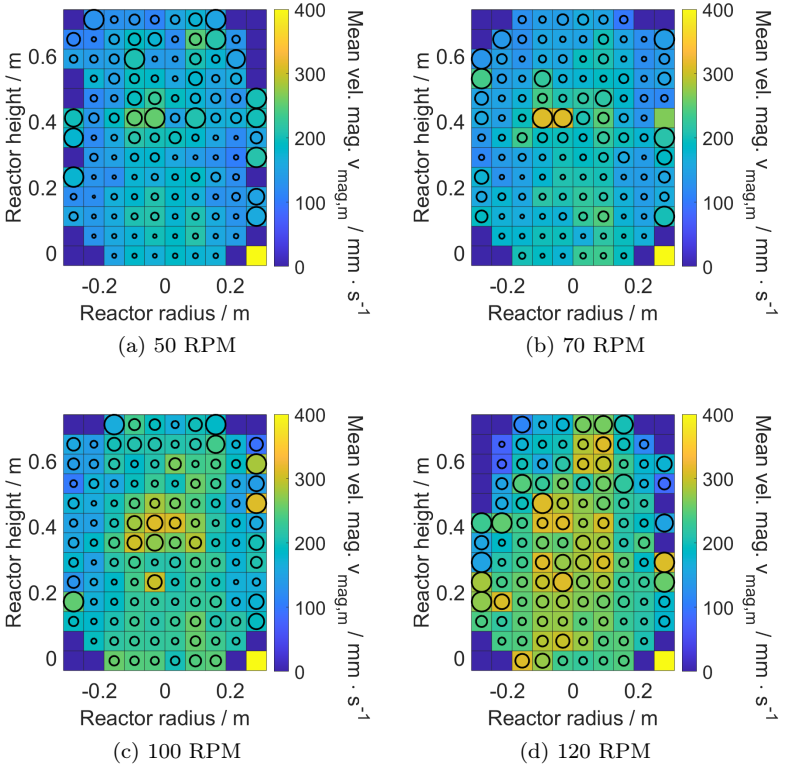

(a) 50 RPM (b) 70 RPM

(c) 100 RPM (d) 120 RPM

Figure B.9.: Distribution of mean velocity magnitudes for the experiment conducted using the double pitched blade impeller (PBPB) setup and an aeration rate of 15 l · min^{-1} utilizing the micro sparger.

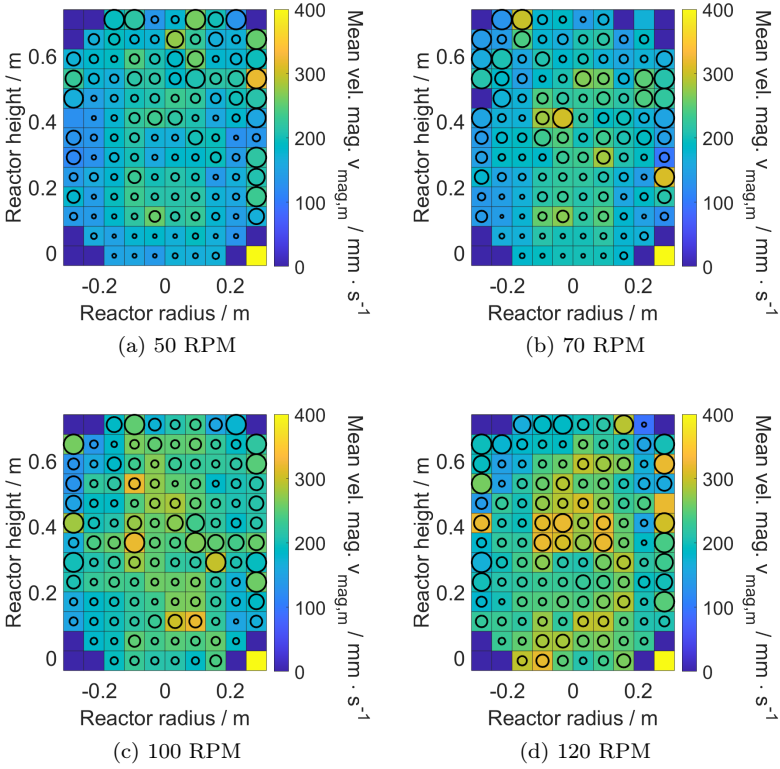

(a) 50 RPM (b) 70 RPM

(c) 100 RPM (d) 120 RPM

Figure B.10.: Distribution of mean velocity magnitudes for the experiment conducted using the double pitched blade impeller (PBPB) setup and an aeration rate of 20 l·min^{-1} utilizing the micro sparger.

B.2. Mean acceleration magnitudes over the 2D grid

Distributions of mean acceleration magnitudes within the reactor displayed in $\mathrm{mm\,s^{-2}}$ for 50, 70, 100 and 120 RPM. The color of each region represents the mean acceleration measured inside of it. The use of $\mathrm{mm\,s^{-2}}$ instead of $\mathrm{m\,s^{-2}}$ is done for technical reasons. The radius of the black circle corresponds to the uncertainty. A black circle touching the border of the interrogation window corresponds to an uncertainty of 1000 $\mathrm{mm\,s^{-2}}$ or higher.

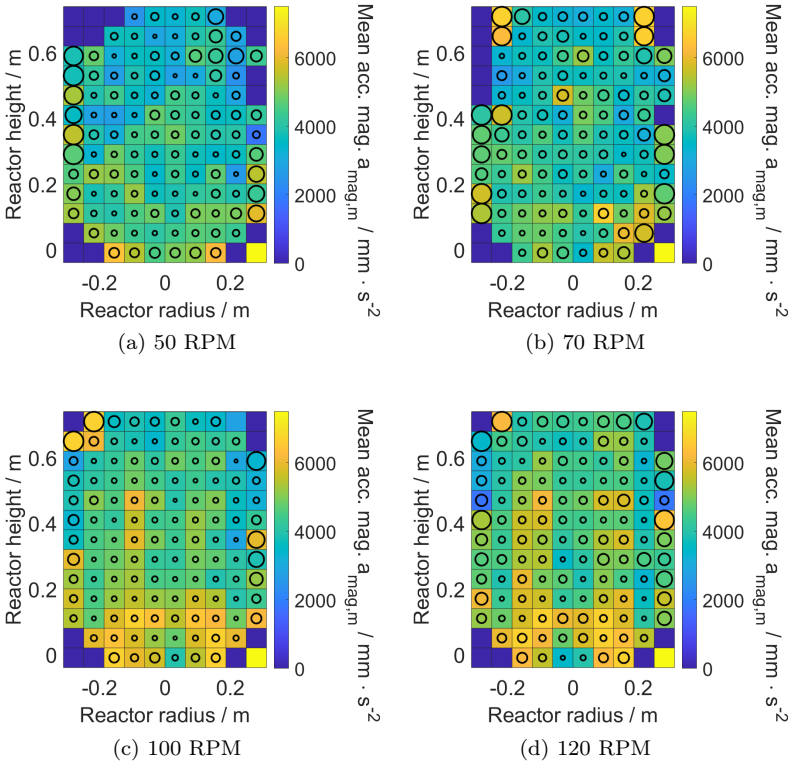

(a) 50 RPM (b) 70 RPM

(c) 100 RPM (d) 120 RPM

Figure B.11.: Distribution of mean acceleration magnitudes for the experiment conducted using the Rushton turbine and pitched blade impeller (RTPB) setup with no aeration.

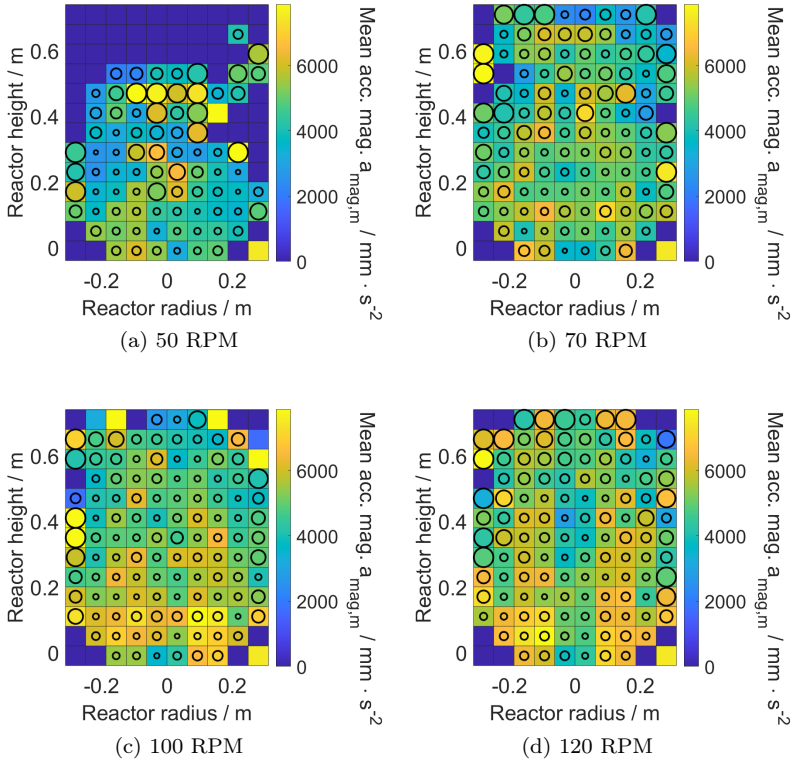

(a) 50 RPM (b) 70 RPM

(c) 100 RPM (d) 120 RPM

Figure B.12.: Distribution of mean acceleration magnitudes for the experiment conducted using the Rushton turbine and pitched blade impeller (RTPB) setup and an aeration rate of 15 $\mathrm{l} \cdot \mathrm{min}^{-1}$ utilizing the macro sparger.

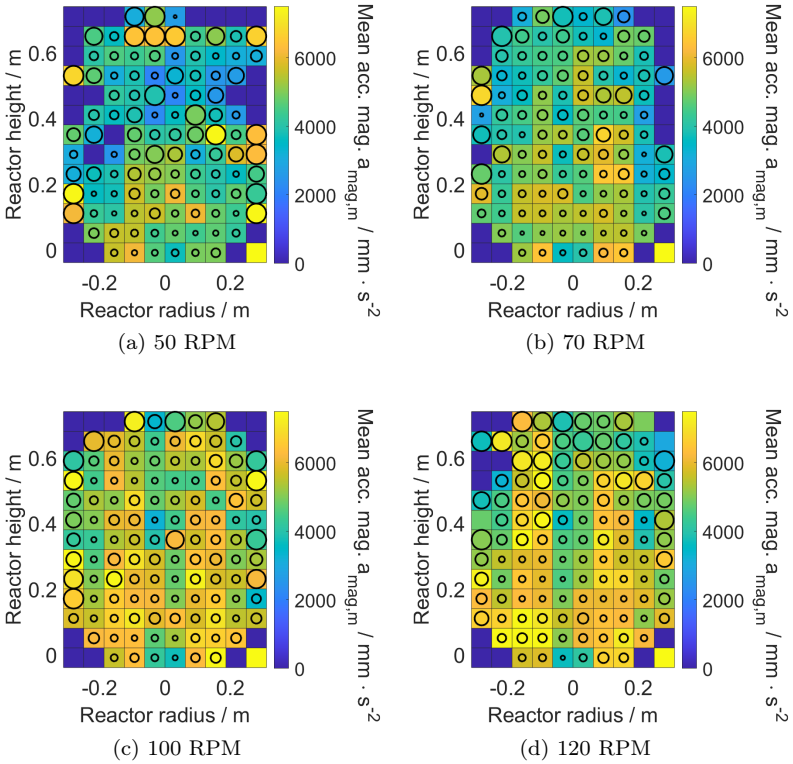

(a) 50 RPM (b) 70 RPM

(c) 100 RPM (d) 120 RPM

Figure B.13.: Distribution of mean acceleration magnitudes for the experiment conducted using the Rushton turbine and pitched blade impeller (RTPB) setup and an aeration rate of 20 $l \cdot min^{-1}$ utilizing the macro sparger.

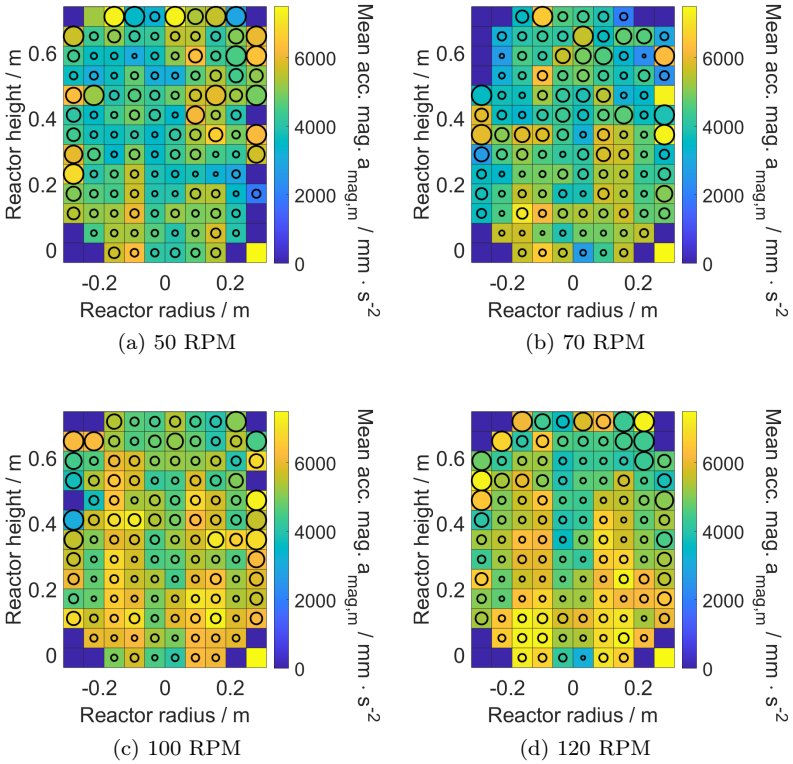

(a) 50 RPM (b) 70 RPM

(c) 100 RPM (d) 120 RPM

Figure B.14.: Distribution of mean acceleration magnitudes for the experiment conducted using the Rushton turbine and pitched blade impeller (RTPB) setup and an aeration rate of 15 $l \cdot min^{-1}$ utilizing the micro sparger.

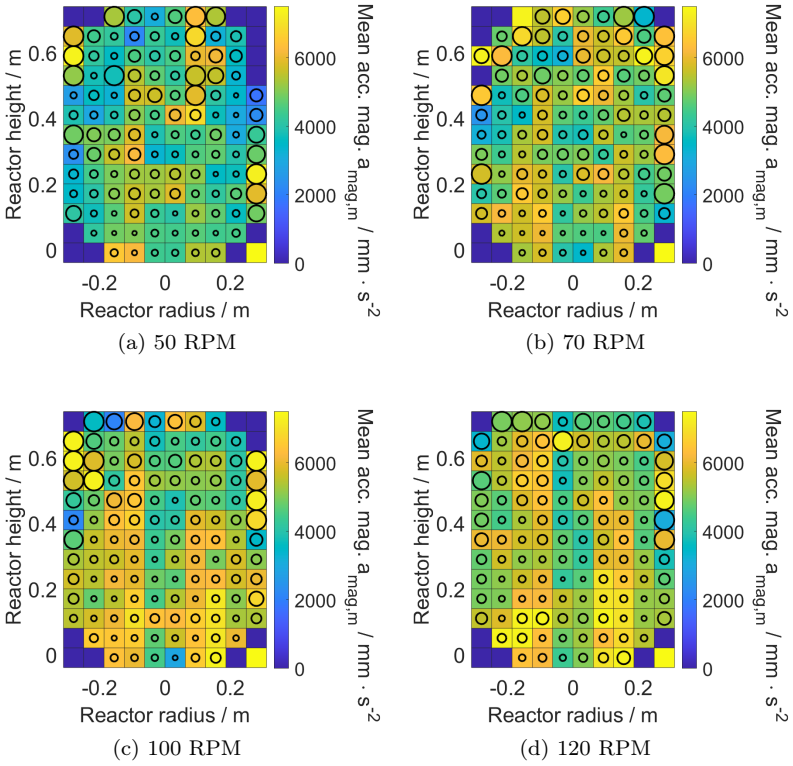

(a) 50 RPM (b) 70 RPM

(c) 100 RPM (d) 120 RPM

Figure B.15.: Distribution of mean acceleration magnitudes for the experiment conducted using the Rushton turbine and pitched blade impeller (RTPB) setup and an aeration rate of 20 $l \cdot min^{-1}$ utilizing the micro sparger.

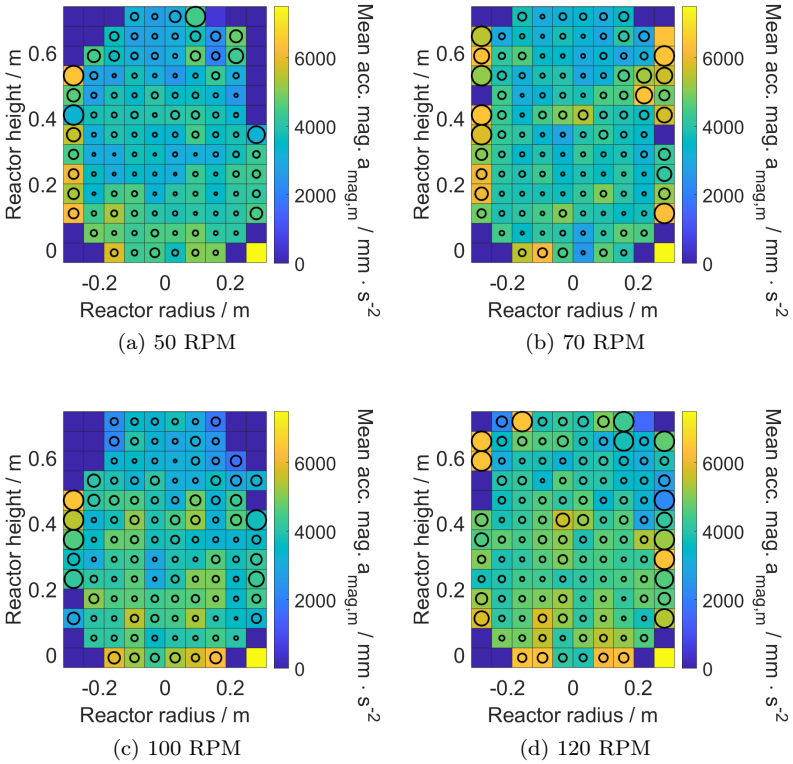

(a) 50 RPM (b) 70 RPM

(c) 100 RPM (d) 120 RPM

Figure B.16.: Distribution of mean acceleration magnitudes for the experiment conducted using the double pitched blade impeller (PBPB) setup with no aeration.

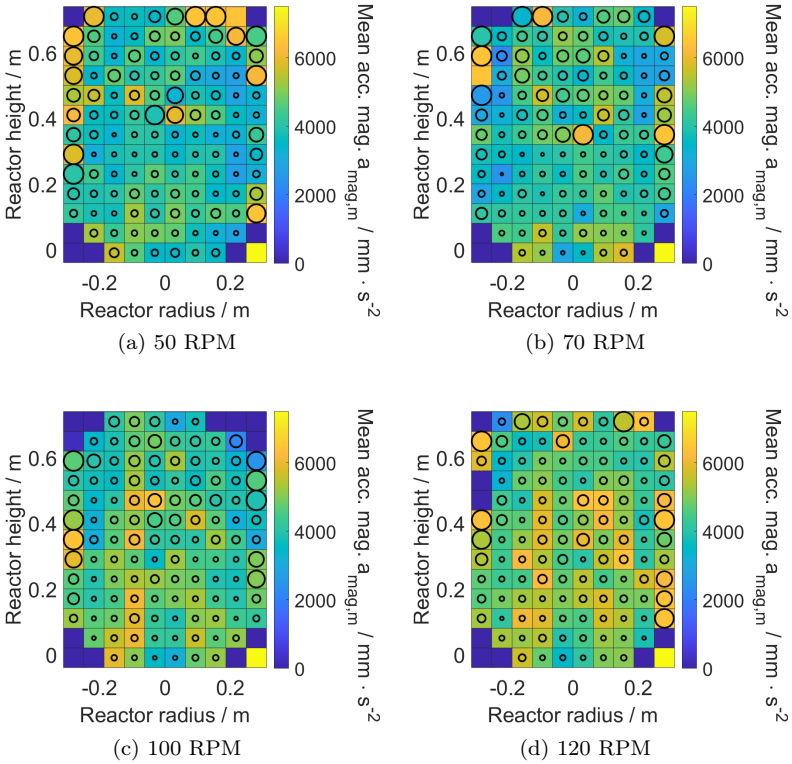

(a) 50 RPM (b) 70 RPM

(c) 100 RPM (d) 120 RPM

Figure B.17.: Distribution of mean acceleration magnitudes for the experiment conducted using the double pitched blade impeller (PBPB) setup and an aeration rate of 15 l · min^{-1} utilizing the macro sparger.

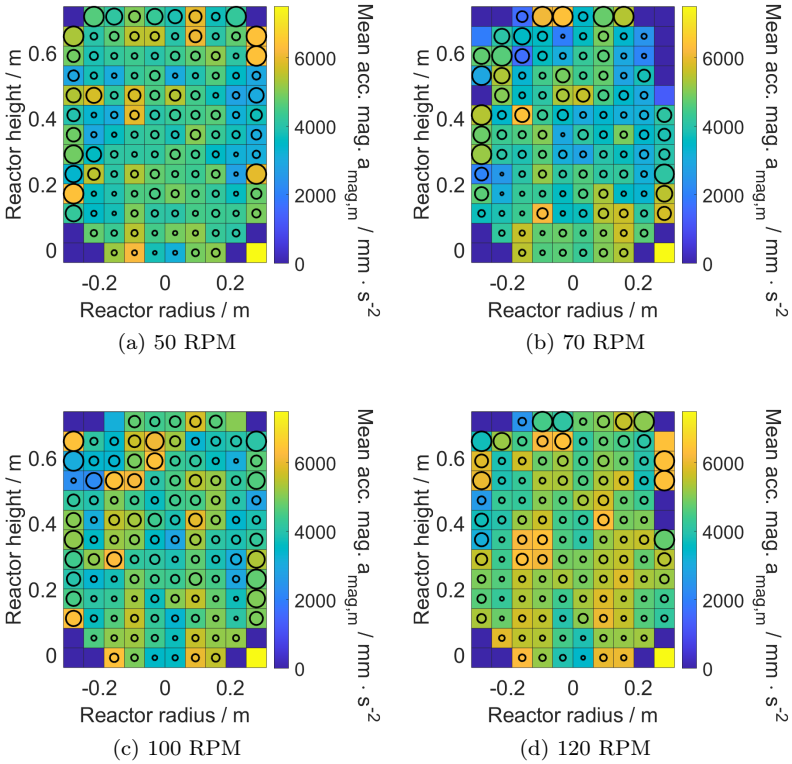

(a) 50 RPM (b) 70 RPM

(c) 100 RPM (d) 120 RPM

Figure B.18.: Distribution of mean acceleration magnitudes for the experiment conducted using the double pitched blade impeller (PBPB) setup and an aeration rate of 20 l · min^{-1} utilizing the macro sparger.

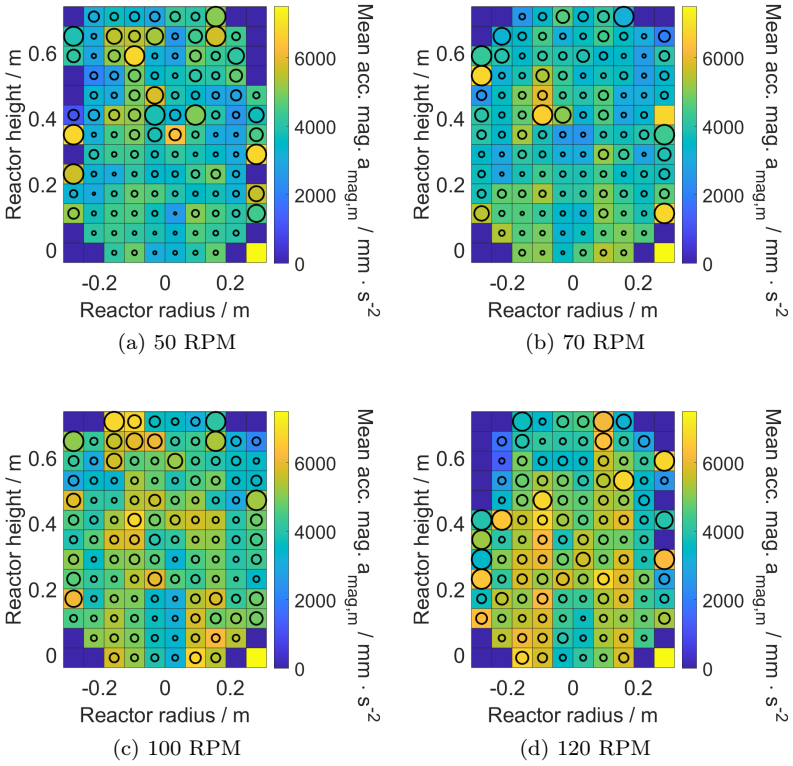

(a) 50 RPM (b) 70 RPM

(c) 100 RPM (d) 120 RPM

Figure B.19.: Distribution of mean acceleration magnitudes for the experiment conducted using the double pitched blade impeller (PBPB) setup and an aeration rate of 15 l · min^{-1} utilizing the micro sparger.

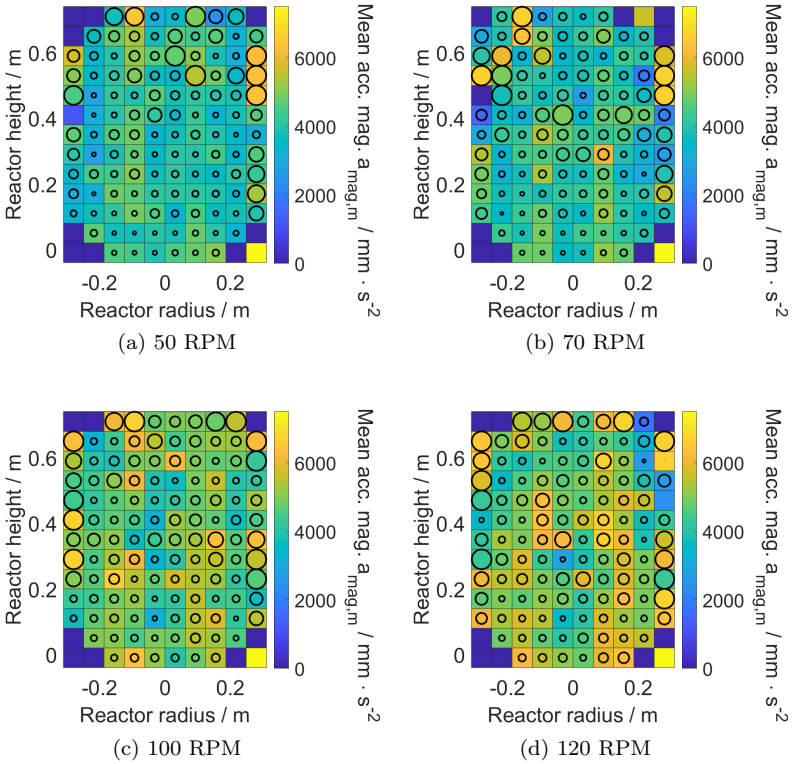

(a) 50 RPM (b) 70 RPM

(c) 100 RPM (d) 120 RPM

Figure B.20.: Distribution of mean acceleration magnitudes for the experiment conducted using the double pitched blade impeller (PBPB) setup and an aeration rate of 20 l · min^{-1} utilizing the micro sparger.

B.3. Probability density distribution over the 2D grid

Distribution of probability of LED Mote occurrence within the reactor for 50, 70, 100 and 120 RPM.

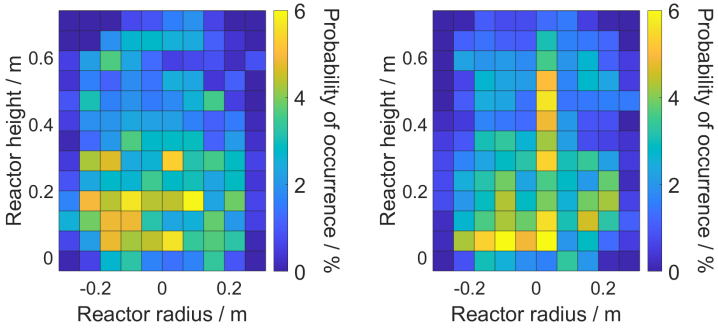

(a) 50 RPM

(b) 70 RPM

(c) 100 RPM

(d) 120 RPM

Figure B.21.: Probability density distribution for the experiment conducted using the Rushton turbine and pitched blade impeller (RTPB) setup with no aeration.

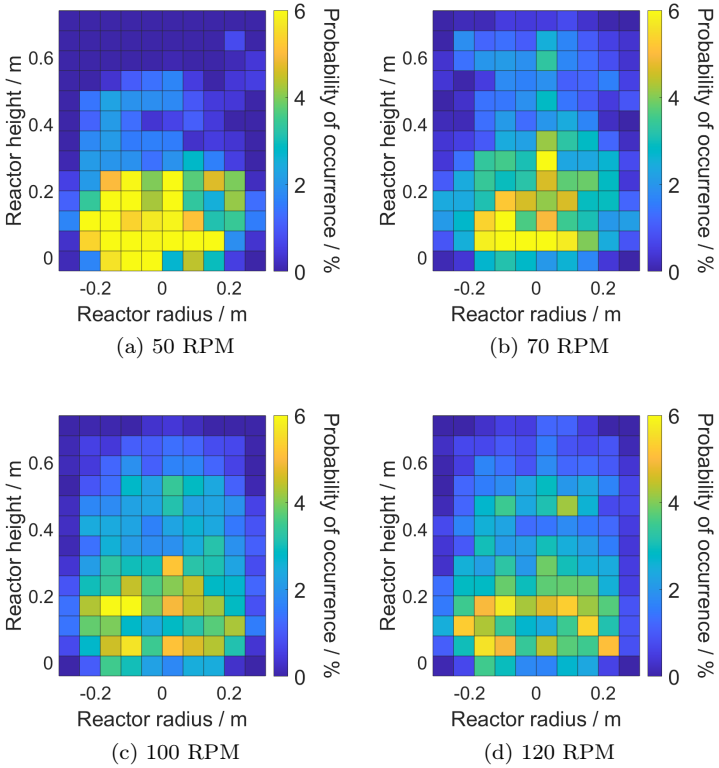

(a) 50 RPM (b) 70 RPM

(c) 100 RPM (d) 120 RPM

Figure B.22.: Probability density distribution for the experiment conducted using the Rushton turbine and pitched blade impeller (RTPB) setup and an aeration rate of 15 $l \cdot min^{-1}$ utilizing the macro sparger.

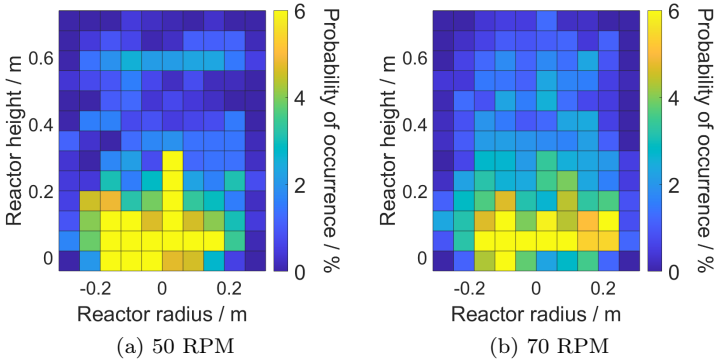

(a) 50 RPM (b) 70 RPM

(c) 100 RPM (d) 120 RPM

Figure B.23.: Probability density distribution for the experiment conducted using the Rushton turbine and pitched blade impeller (RTPB) setup and an aeration rate of 20 $l \cdot min^{-1}$ utilizing the macro sparger.

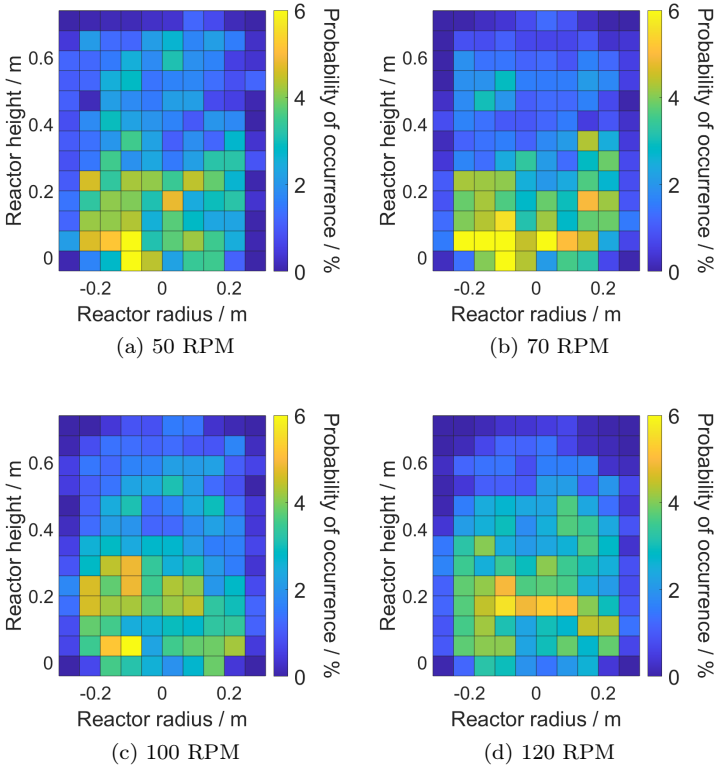

(a) 50 RPM (b) 70 RPM

(c) 100 RPM (d) 120 RPM

Figure B.24.: Probability density distribution for the experiment conducted using the Rushton turbine and pitched blade impeller (RTPB) setup and an aeration rate of 15 $l \cdot min^{-1}$ utilizing the micro sparger.

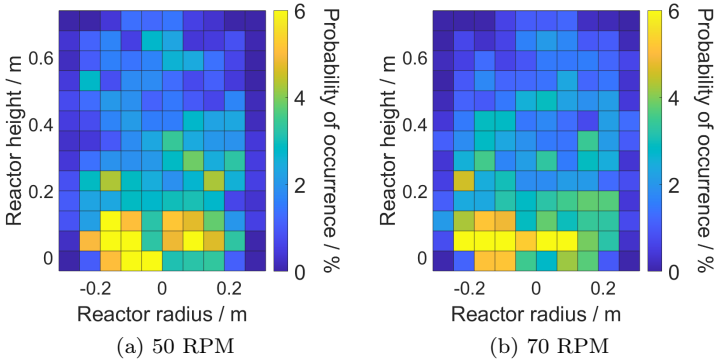

(a) 50 RPM (b) 70 RPM

(c) 100 RPM (d) 120 RPM

Figure B.25.: Probability density distribution for the experiment conducted using the Rushton turbine and pitched blade impeller (RTPB) setup and an aeration rate of 20 $l \cdot min^{-1}$ utilizing the micro sparger.

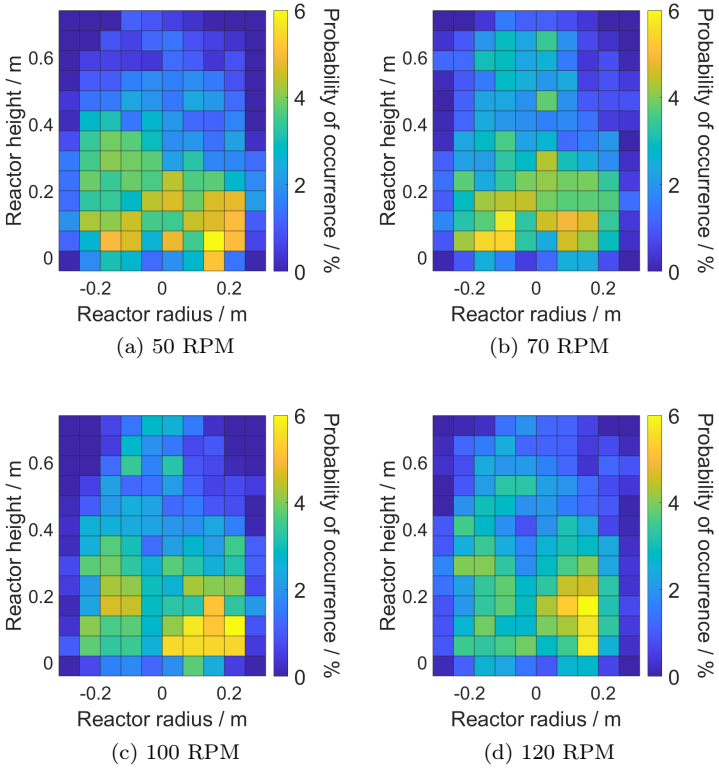

(a) 50 RPM (b) 70 RPM

(c) 100 RPM (d) 120 RPM

Figure B.26.: Probability density distribution for the experiment conducted using the double pitched blade impeller (PBPB) setup with no aeration.

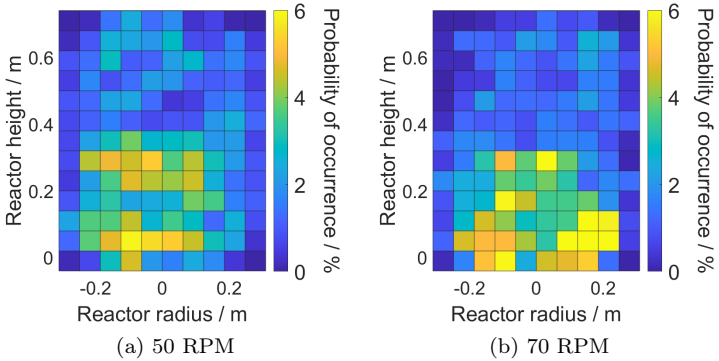

(a) 50 RPM (b) 70 RPM

(c) 100 RPM (d) 120 RPM

Figure B.27.: Probability density distribution for the experiment conducted using the double pitched blade impeller (PBPB) setup and an aeration rate of 15 $l \cdot min^{-1}$ utilizing the macro sparger.

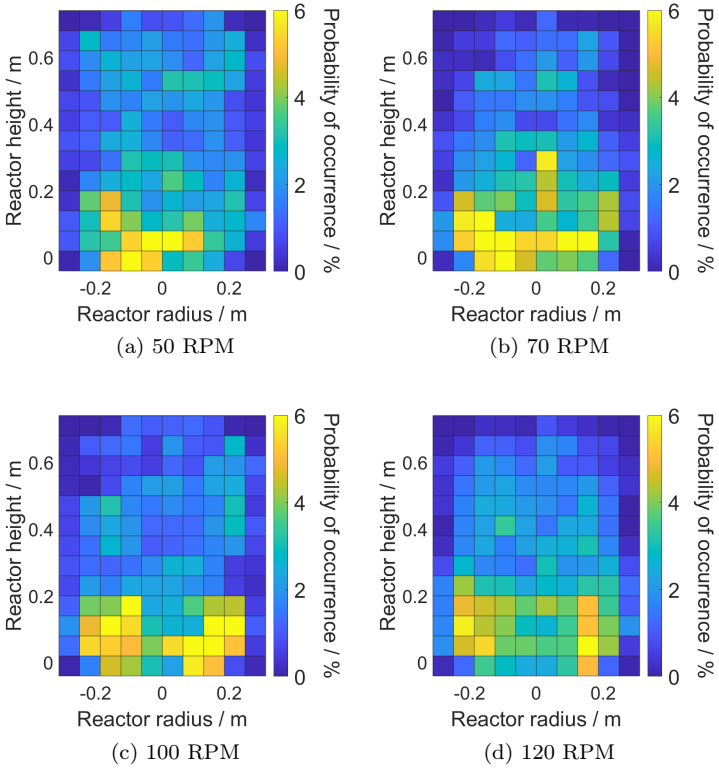

(a) 50 RPM (b) 70 RPM

(c) 100 RPM (d) 120 RPM

Figure B.28.: Probability density distribution for the experiment conducted using the double pitched blade impeller (PBPB) setup and an aeration rate of 20 $\mathrm{l} \cdot \mathrm{min}^{-1}$ utilizing the macro sparger.

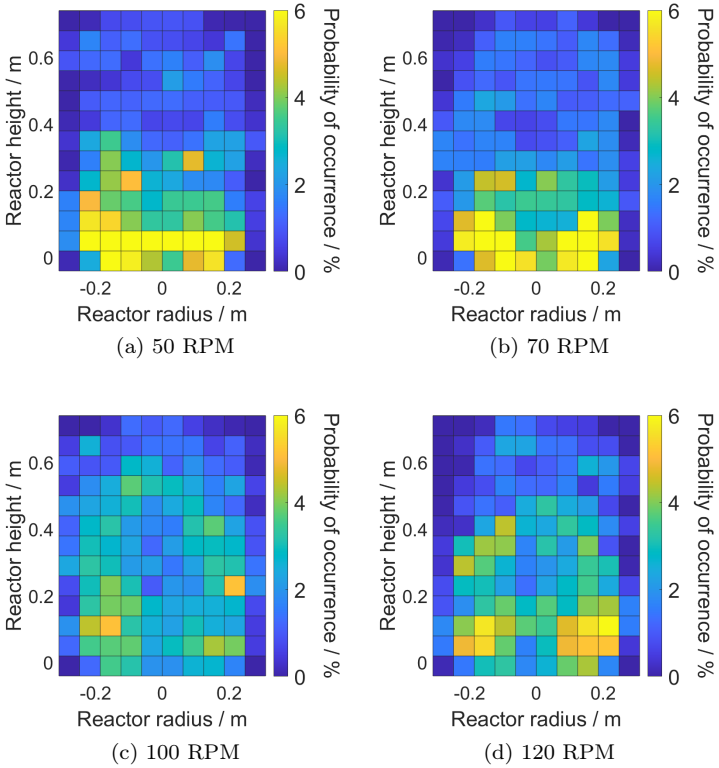

(a) 50 RPM (b) 70 RPM

(c) 100 RPM (d) 120 RPM

Figure B.29.: Probability density distribution for the experiment conducted using the double pitched blade impeller (PBPB) setup and an aeration rate of 15 $l \cdot min^{-1}$ utilizing the micro sparger.

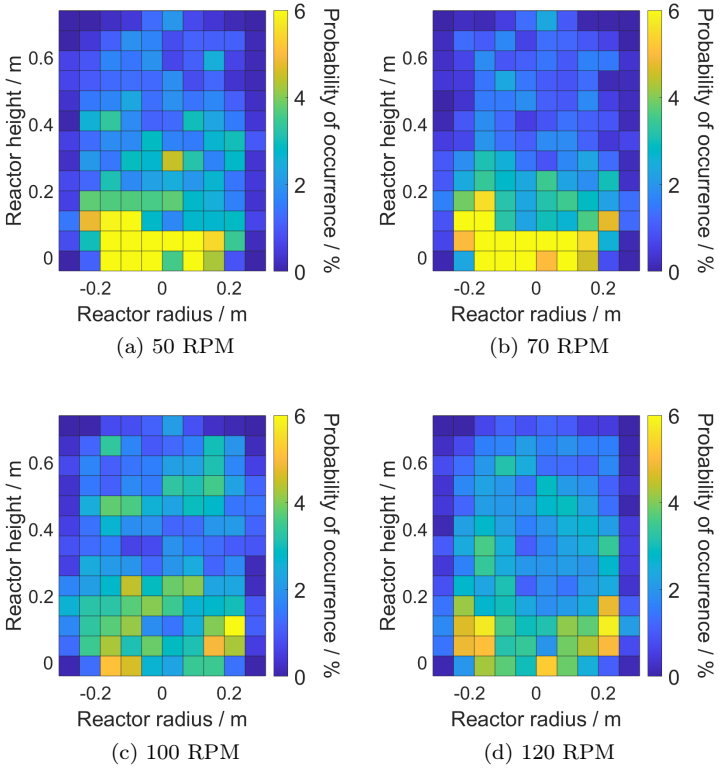

(a) 50 RPM (b) 70 RPM

(c) 100 RPM (d) 120 RPM

Figure B.30.: Probability density distribution for the experiment conducted using the double pitched blade impeller (PBPB) setup and an aeration rate of 20 $\mathrm{l} \cdot \mathrm{min}^{-1}$ utilizing the micro sparger.

C. Velocity Vectors Throughout The Reactor

Resulting total velocity vectors throughout the reactor when combining mean radial and axial velocities for 50, 70, 100 and 120 RPM. The length of each vector represents the total mean velocity.

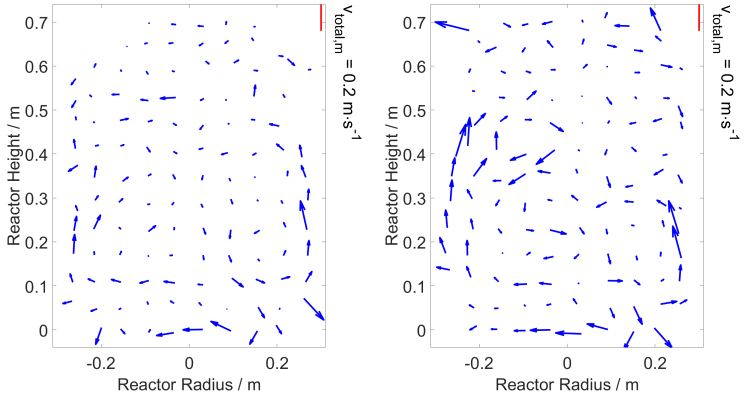

(a) 50 RPM (b) 70 RPM

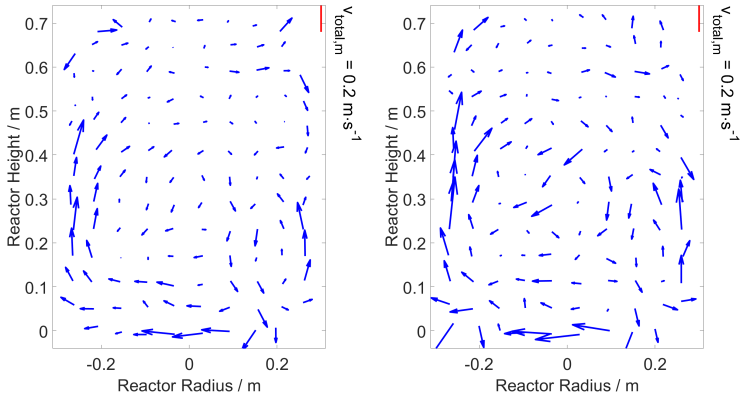

(c) 100 RPM (d) 120 RPM

Figure C.1.: Resulting velocity vectors throughout the reactor when combining mean radial and axial velocities for experiments conducted using the Rushton turbine and pitched blade impeller (RTPB) setup with no aeration.

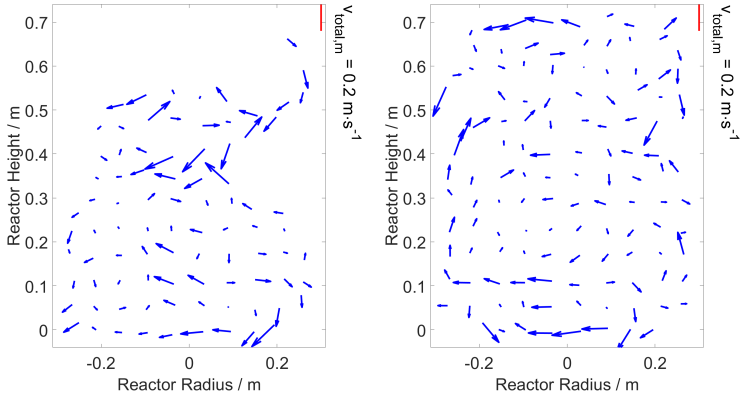

(a) 50 RPM (b) 70 RPM

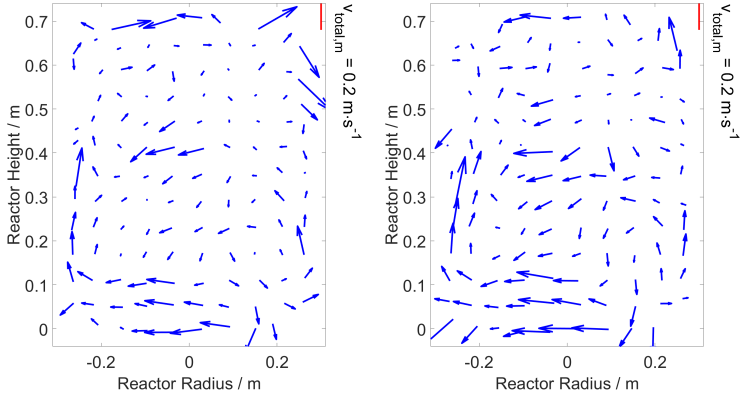

(c) 100 RPM (d) 120 RPM

Figure C.2.: Resulting velocity vectors throughout the reactor when combining mean radial and axial velocities for experiments conducted using the Rushton turbine and pitched blade impeller (RTPB) setup and an aeration rate of 15 $\mathrm{l} \cdot \mathrm{min}^{-1}$ utilizing the macro sparger.

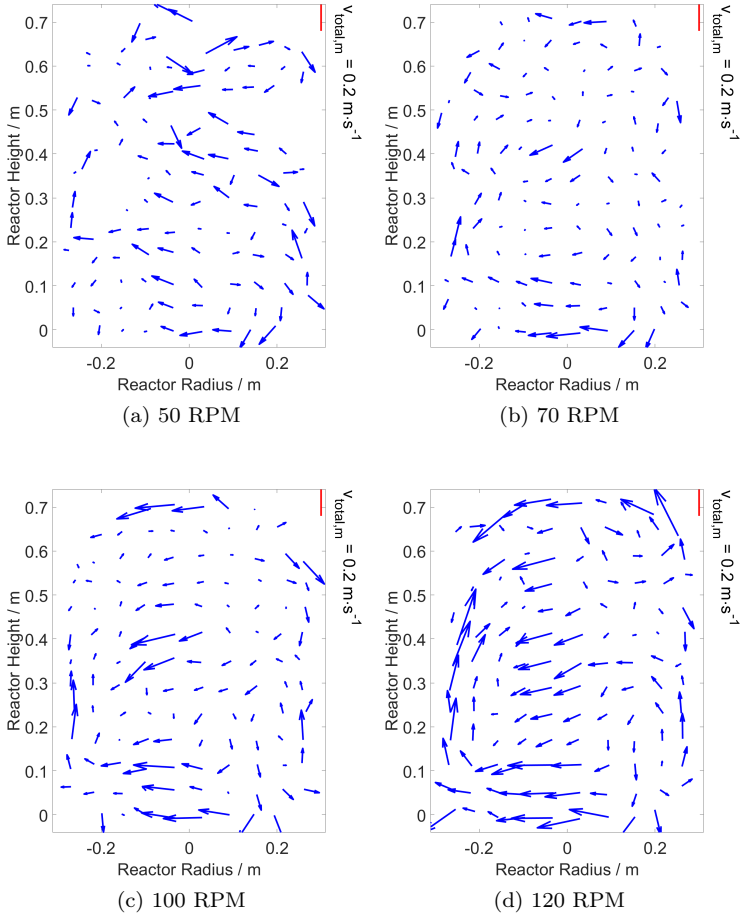

(a) 50 RPM (b) 70 RPM

(c) 100 RPM (d) 120 RPM

Figure C.3.: Resulting velocity vectors throughout the reactor when combining mean radial and axial velocities for experiments conducted using the Rushton turbine and pitched blade impeller (RTPB) setup and an aeration rate of $20\ \mathrm{l} \cdot \mathrm{min}^{-1}$ utilizing the macro sparger.

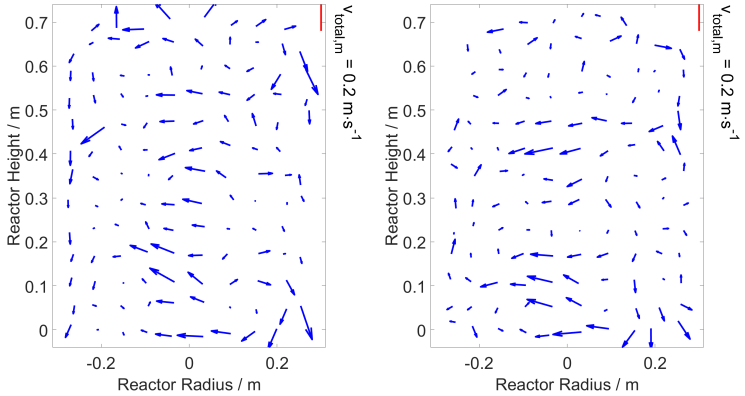

(a) 50 RPM (b) 70 RPM

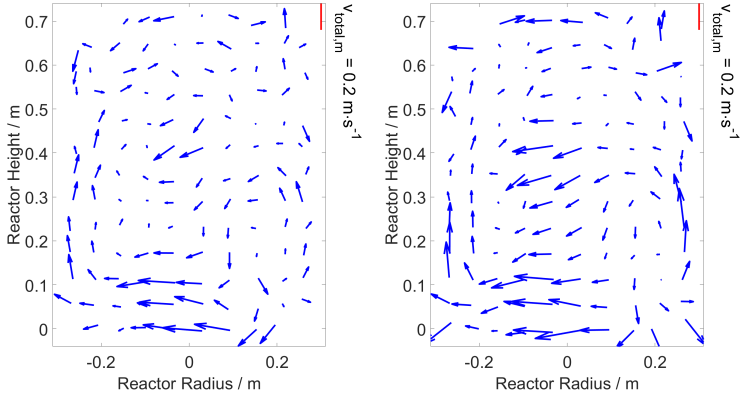

(c) 100 RPM (d) 120 RPM

Figure C.4.: Resulting velocity vectors throughout the reactor when combining mean radial and axial velocities for experiments conducted using the Rushton turbine and pitched blade impeller (RTPB) setup and an aeration rate of 15 $\mathrm{l} \cdot \mathrm{min}^{-1}$ utilizing the micro sparger.

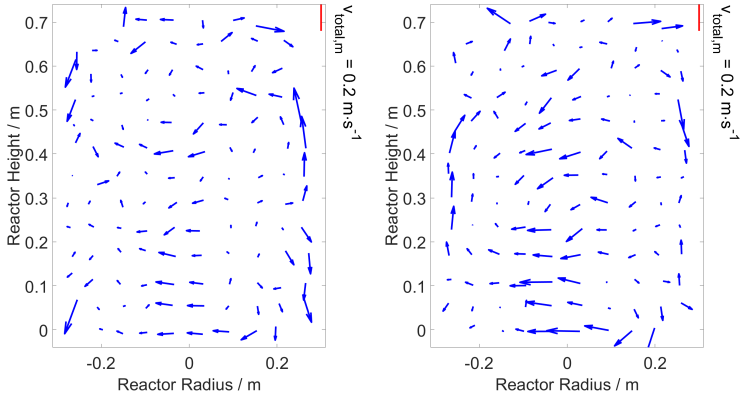

(a) 50 RPM (b) 70 RPM

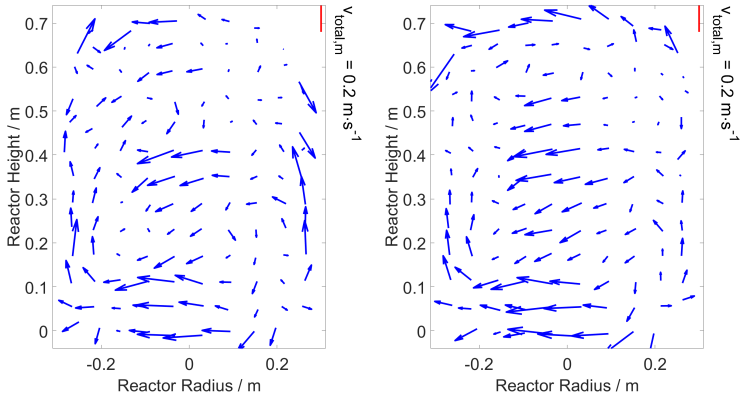

(c) 100 RPM (d) 120 RPM

Figure C.5.: Resulting velocity vectors throughout the reactor when combining mean radial and axial velocities for experiments conducted using the Rushton turbine and pitched blade impeller (RTPB) setup and an aeration rate of $20\ \mathrm{l} \cdot \mathrm{min}^{-1}$ utilizing the micro sparger.

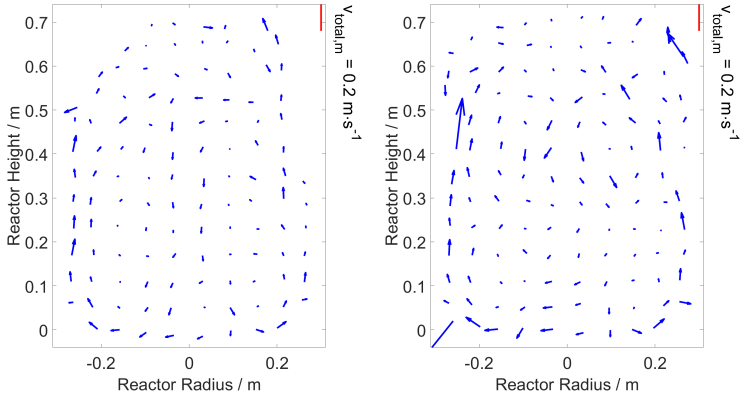

(a) 50 RPM (b) 70 RPM

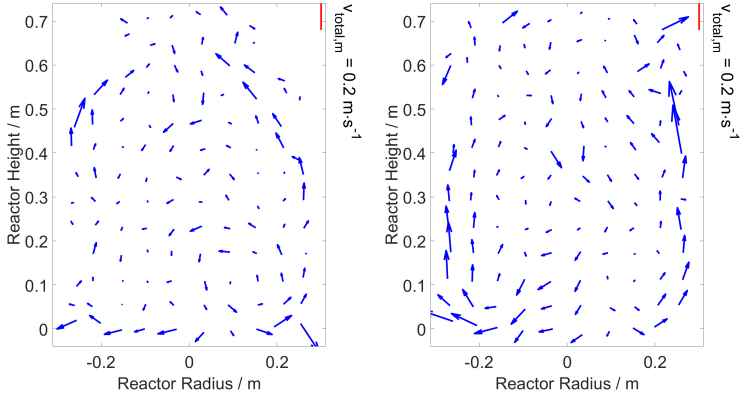

(c) 100 RPM (d) 120 RPM

Figure C.6.: Resulting velocity vectors throughout the reactor when combining mean radial and axial velocities for experiments conducted using the double pitched blade impeller (PBPB) setup with no aeration.

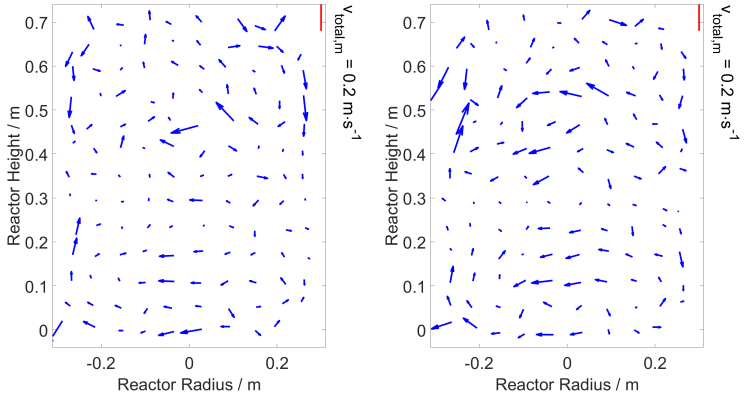

(a) 50 RPM (b) 70 RPM

(c) 100 RPM (d) 120 RPM

Figure C.7.: Resulting velocity vectors throughout the reactor when combining mean radial and axial velocities for experiments conducted using the double pitched blade impeller (PBPB) setup and an aeration rate of 15 $l \cdot min^{-1}$ utilizing the macro sparger.

L

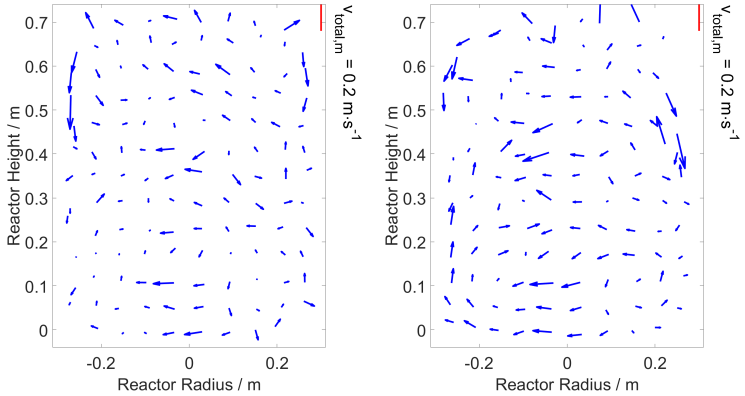

(a) 50 RPM (b) 70 RPM

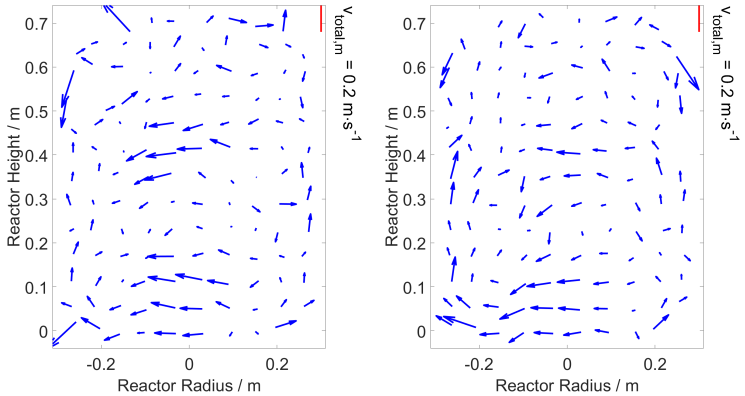

(c) 100 RPM (d) 120 RPM

Figure C.8.: Resulting velocity vectors throughout the reactor when combining mean radial and axial velocities for experiments conducted using the double pitched blade impeller (PBPB) setup and an aeration rate of 20 $l \cdot min^{-1}$ utilizing the macro sparger.

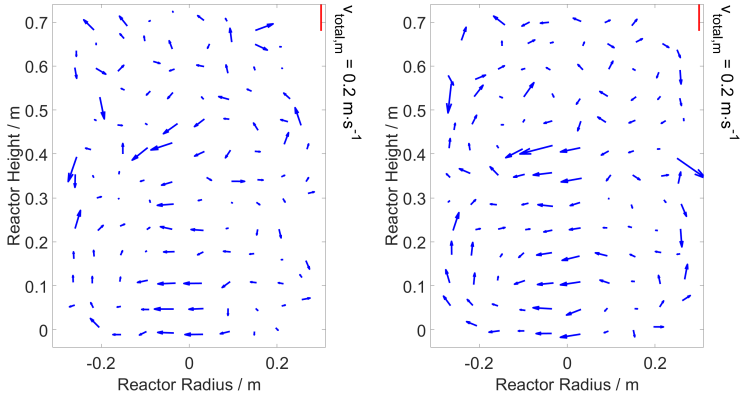

(a) 50 RPM (b) 70 RPM

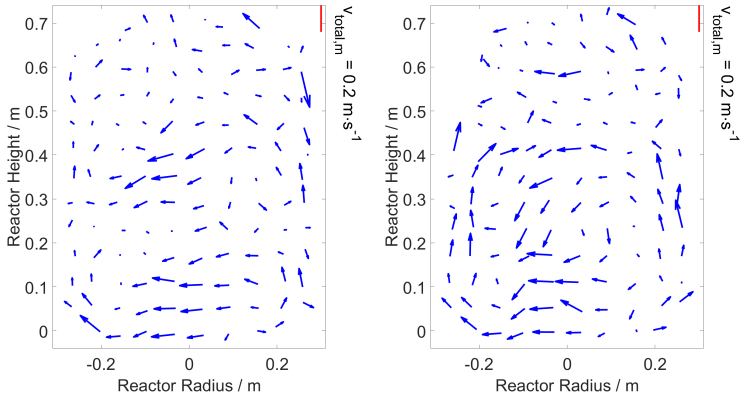

(c) 100 RPM (d) 120 RPM

Figure C.9.: Resulting velocity vectors throughout the reactor when combining mean radial and axial velocities for experiments conducted using the double pitched blade impeller (PBPB) setup and an aeration rate of 15 $l \cdot min^{-1}$ utilizing the micro sparger.

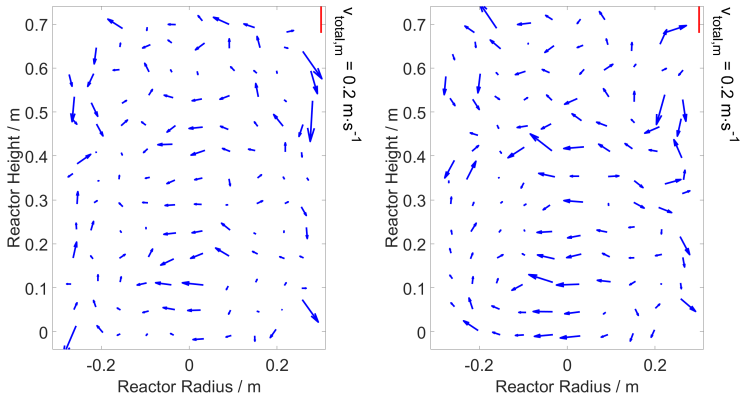

(a) 50 RPM (b) 70 RPM

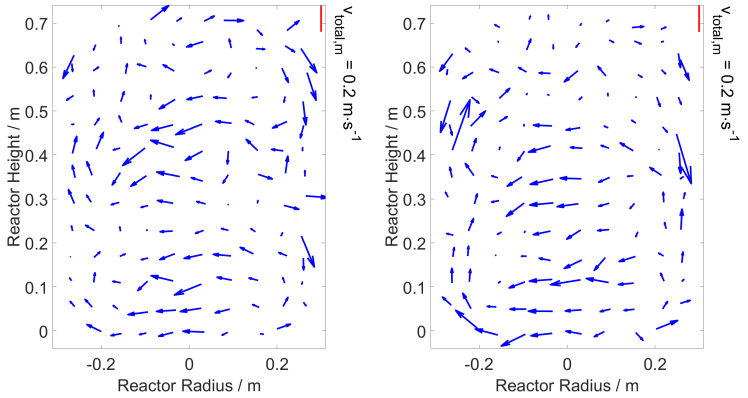

(c) 100 RPM (d) 120 RPM

Figure C.10.: Resulting velocity vectors throughout the reactor when combining mean radial and axial velocities for experiments conducted using the double pitched blade impeller (PBPB) setup and an aeration rate of 20 $l \cdot min^{-1}$ utilizing the micro sparger.

D. Track Length Statistics

The following figures show the track length statistics for the individual experiments. The bin size is 5. The maximum observed track length is 240 individual positions, meaning the track was kept for a minimum of 10 seconds. Track counts of up to 100 are shown. The minimum track length considered by the script is 5. Located positions belonging to a track with a length of less than 5 positions are not considered for the calculation of velocities and acceleration. The value k in the figures represents the total number of tracks for the respective experiment. The value p represents the total number of positions belonging to tracks with a length of 5 or more positions. The value j represents the total number of positions detected by the script. The value r represents the ratio of p and j, meaning the ratio of positions evaluated for velocity and acceleration calculations and the total number of detected positions for that experiment. The maximum theoretical number of correctly recognized position is 14400 for an experiment with a duration of 120 s and 25200 for an experiment with a duration of 210 s. These numbers are calculated based on perfect detection of LED Motes with no obscuration and no stuck and discarded motes.

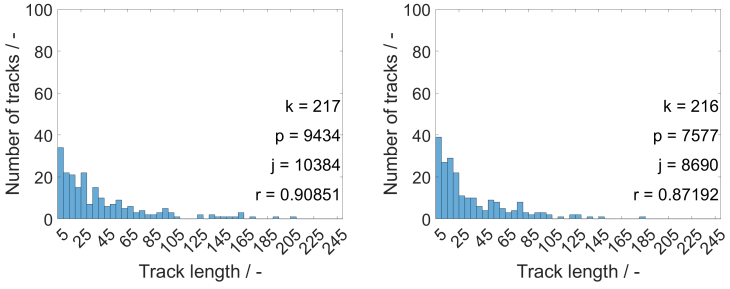

(a) 50 RPM

(b) 70 RPM

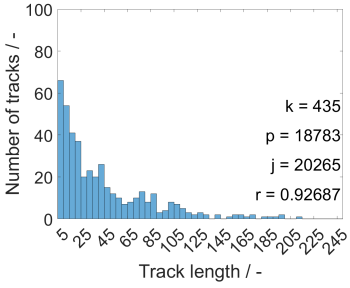

(c) 100 RPM

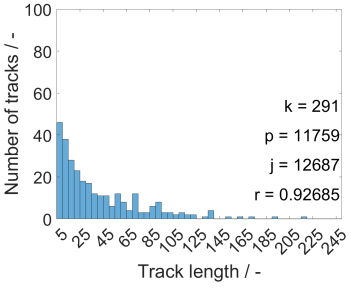

(d) 120 RPM

Figure D.1.: Probability density function plot of the track length for the experiment conducted using the Rushton turbine and pitched blade impeller (RTPB) setup with no aeration.

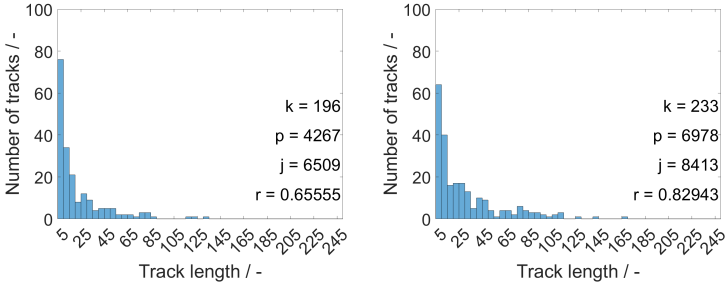

(a) 50 RPM

(b) 70 RPM

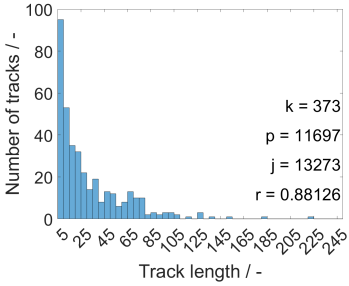

(c) 100 RPM

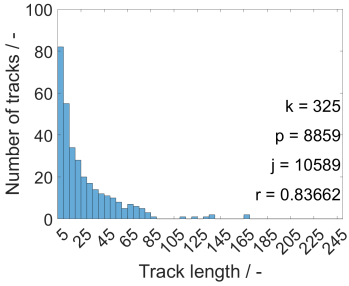

(d) 120 RPM

Figure D.2.: Probability density function plot of the track length for the experiment conducted using the Rushton turbine and pitched blade impeller (RTPB) setup and an aeration rate of 15 $l \cdot min^{-1}$ utilizing the macro sparger.

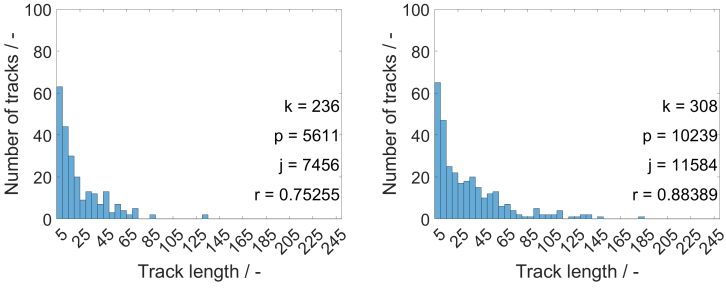

(a) 50 RPM

(b) 70 RPM

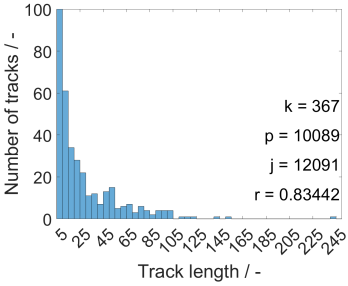

(c) 100 RPM

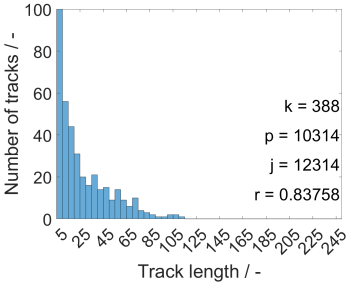

(d) 120 RPM

Figure D.3.: Probability density function plot of the track length for the experiment conducted using the Rushton turbine and pitched blade impeller (RTPB) setup and an aeration rate of 20 $\mathrm{l} \cdot \mathrm{min}^{-1}$ utilizing the macro sparger.

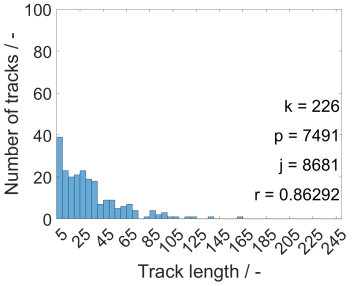

(a) 50 RPM

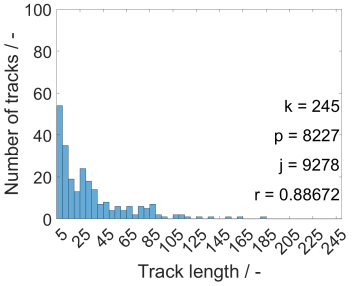

(b) 70 RPM

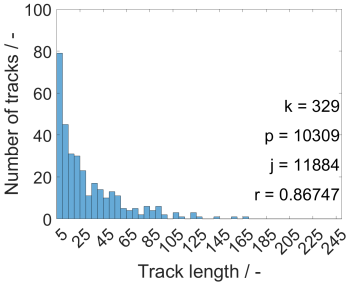

(c) 100 RPM

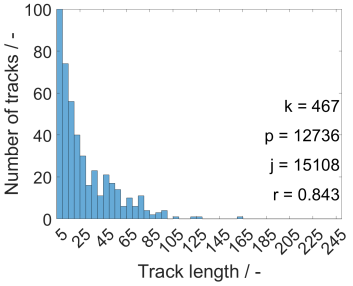

(d) 120 RPM

Figure D.4.: Probability density function plot of the track length for the experiment conducted using the Rushton turbine and pitched blade impeller (RTPB) setup and an aeration rate of 15 $\mathrm{l} \cdot \mathrm{min}^{-1}$ utilizing the micro sparger.

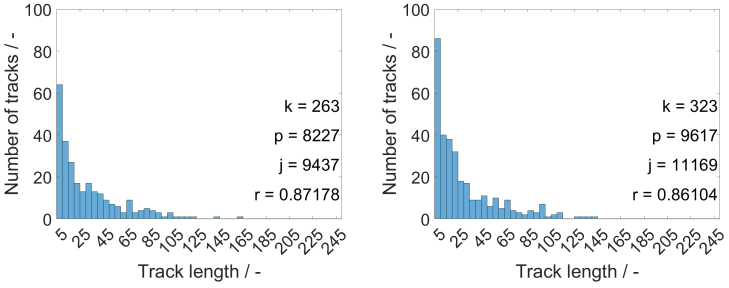

(a) 50 RPM

(b) 70 RPM

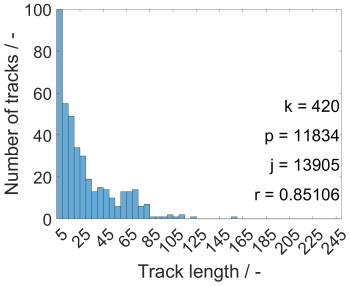

(c) 100 RPM

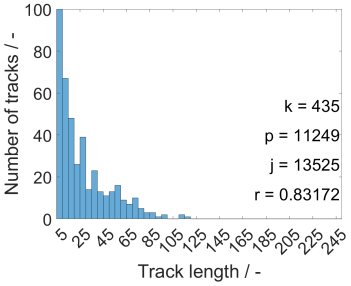

(d) 120 RPM

Figure D.5.: Probability density function plot of the track length for the experiment conducted using the Rushton turbine and pitched blade impeller (RTPB) setup and an aeration rate of 20 $l \cdot min^{-1}$ utilizing the micro sparger.

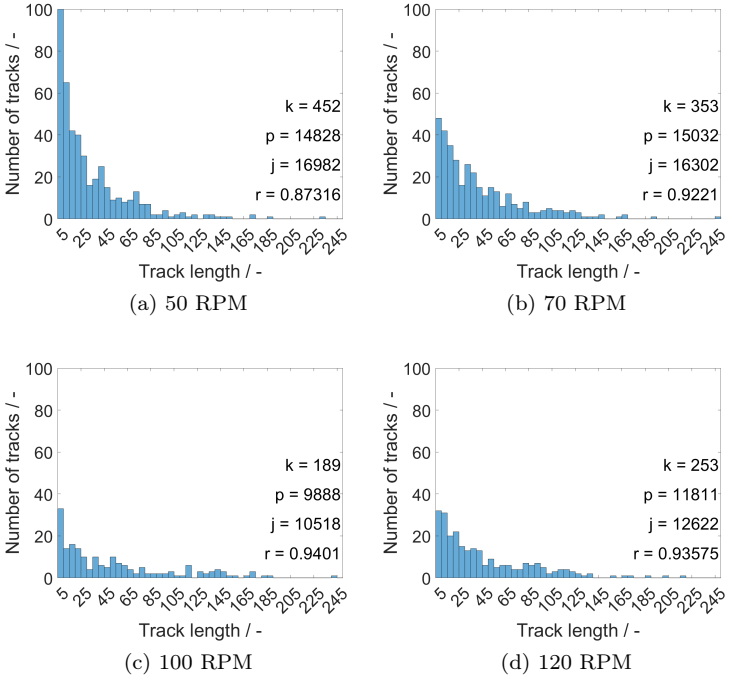

(a) 50 RPM (b) 70 RPM

(c) 100 RPM (d) 120 RPM

Figure D.6.: Probability density function plot of the track length for the experiment conducted using the double pitched blade impeller (PBPB) setup with no aeration.

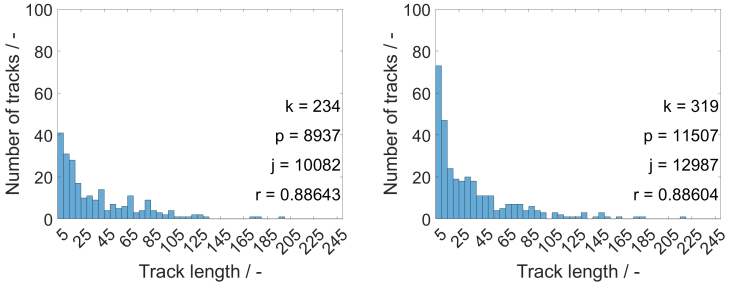

(a) 50 RPM

(b) 70 RPM

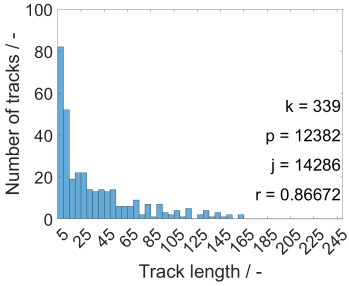

(c) 100 RPM

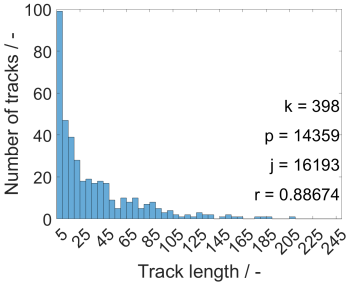

(d) 120 RPM

Figure D.7.: Probability density function plot of the track length for the experiment conducted using the double pitched blade impeller (PBPB) setup and an aeration rate of 15 $\mathrm{l} \cdot \mathrm{min}^{-1}$ utilizing the macro sparger.

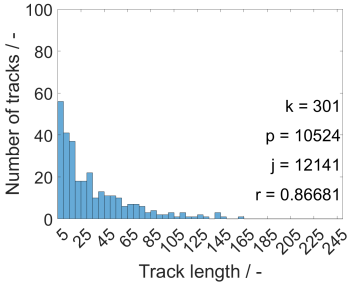

(a) 50 RPM

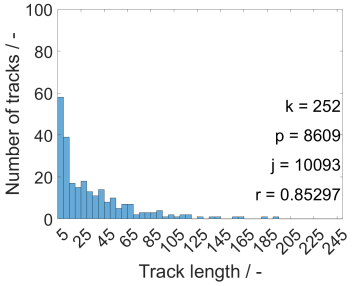

(b) 70 RPM

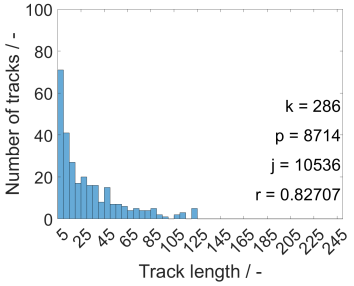

(c) 100 RPM

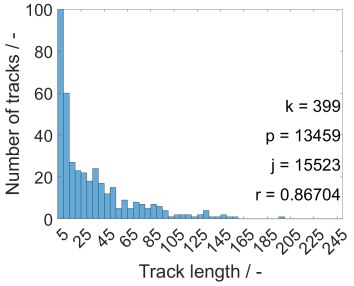

(d) 120 RPM

Figure D.8.: Probability density function plot of the track length for the experiment conducted using the double pitched blade impeller (PBPB) setup and an aeration rate of 20 $\mathrm{l} \cdot \mathrm{min}^{-1}$ utilizing the macro sparger.

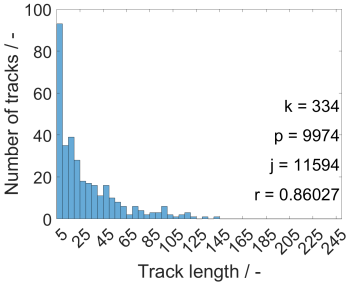

(a) 50 RPM

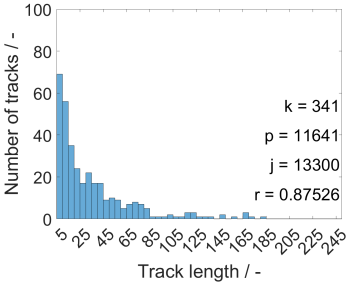

(b) 70 RPM

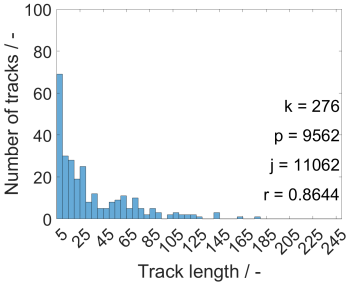

(c) 100 RPM

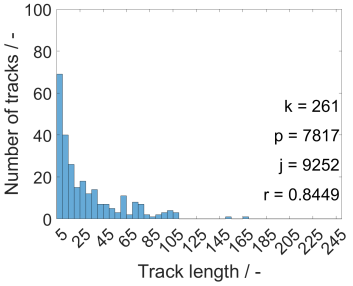

(d) 120 RPM

Figure D.9.: Probability density function plot of the track length for the experiment conducted using the double pitched blade impeller (PBPB) setup and an aeration rate of 15 $\mathrm{l} \cdot \mathrm{min}^{-1}$ utilizing the micro sparger.

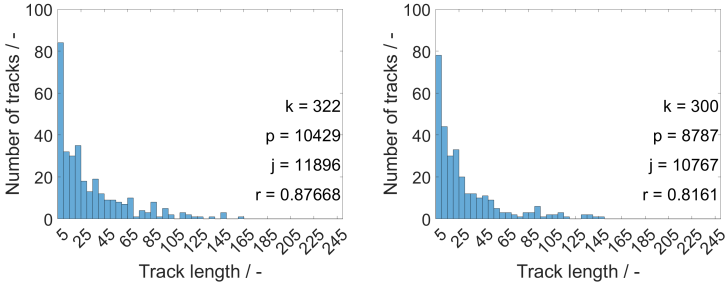

(a) 50 RPM

(b) 70 RPM

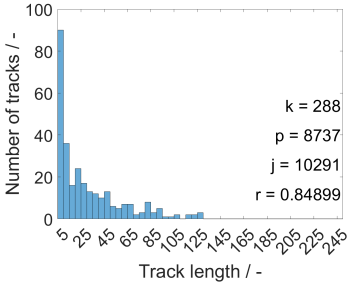

(c) 100 RPM

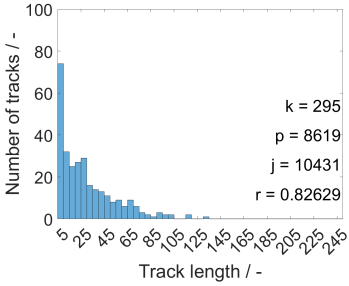

(d) 120 RPM

Figure D.10.: Probability density function plot of the track length for the experiment conducted using the double pitched blade impeller (PBPB) setup and an aeration rate of 20 $\mathrm{l} \cdot \mathrm{min}^{-1}$ utilizing the micro sparger.

E. Developed Script

The developed script is available online at:
https://doi.org/10.18419/darus-2811
and
https://collaborating.tuhh.de/SebastianHofmannIMS/2d-lagrangian-led-particle-tracking

F. Miscellaneous Equations

Equation F.1 for the calculation of mass concentrations of sodium chloride in water corresponding to a certain density from two known points of mass correspondence - density correlation. Here $c_{\text{mass,NaCl}}$ is the mass concentration of the respective solution and ρ_{solution} is the density of the solution.

$$c_{\text{mass,NaCl}} = c_{\text{mass,NaCl,1}} + (\rho_{\text{solution}} - \rho_{\text{solution,1}}) \cdot \frac{c_{\text{mass,NaCl,2}} - c_{\text{mass,NaCl,1}}}{\rho_{\text{solution,2}} - \rho_{\text{solution,1}}} \tag{F.1}$$

Equation F.2 shows the calculation of mean velocity and acceleration magnitudes. Here x_{mean} is the mean velocity or acceleration magnitude, x_i is a single velocity or acceleration and u is the total number of velocities or accelerations inside of the bin.

$$x_{\text{mean}} = \frac{\sum_u |x_i|}{u} \tag{F.2}$$